The University Of Sheffield.

Water gated thin film-transistors: Ion sensing and modes of operation

By:
Abbad Fahad Al Baroot

A thesis submitted in partial fulfilment of the requirements for the degree of Doctor of Philosophy in Physics.

Faculty of Science
Department of Physics and Astronomy
The University of Sheffield

July 2019

I dedicate this thesis to my beloved family,

My parents, my wife, my sons, my brothers and my sisters.

Acknowledgements

First of all, I would like to thank and praise **Allah** who is giving me the potential, activity and guide me to complete my study. Then I would like to thank all my **love family** especially my parents, wife, sons for their support and patient during this long journey.

I would like to express special thanks, respect and appreciation to my supervisor **Dr. Martin Grell** for his support, his idea, his patient, his massive knowledge and his contribution during my PhD study.

I would like to extend special thanks to my co-supervisor **Dr. Jenny Clark** for her support, and her encouragement during my study.

I would like to thank all my lab's team; **Dr.Saud, Dr Talal, Dr. Abraham, Dr. Krisina,** Alhuluw, Nawal and Zahrah for their help, support, ideas and their contribution during our work.

I would like to thank Imam Abdulrahman Bin Faisal University for giving me the chance and funded me during my PhD study.

Published papers and attended conferences

1- T. Althagafi, **A. Al Baroot**, S. Algarni, and M. Grell. "A membrane- free cation selective water- gated transistor". **Analyst**, 2016,141, 5571-5576.

2- T. Althagafi, **A. Al Baroot** and M. Grell "A new precursor route to semiconducting Zinc Oxide". **IEEE Electron Device Letters**, 2016, 0741-3106

3- A. Al Baroot and M. Grell. "Comparing electron-and hole transporting semiconductors in ion sensitive water-gated transistors." **Materials Science in Semiconductor Processing** 89 (2019): 216-222.

4- A. Al Baroot, A. Alshammari, and M. Grell. (2019). Electrochemical gating of a hydrophobic organic semiconductor with aqueous media**. Thin Solid Films,** 669, 665-669.

5- A. Al Baroot, T. Althagafi, S. Algarni, and M. Grell. "A membrane- free cation selective water- gated transistor". **Poster presentation** in the Octagon-University of Sheffield, Faculty of Science Graduate School Poster Day, United Kingdom (26th April 2017).

6- A. Al Baroot, M. Grell "Crown ethers in ion- sensitive water- gated transistors with organic and inorganic semiconductors". **Poster presentation** in ERPOS 2017 Conference on Electrical and Related Properties of Organic Solids held in University of St Andrews, Scotland (9-13 July 2017).

Abstract

This thesis investigates the ion sensing properties, and modes of operation, of water gated thin film transistors (WGTFTs).For ion sensing, suitable sensitisers ('ionophores') are integrated into the (WGTFT) architecture that lead to a membrane or interface potential in response to changing concentrations of the ionophore's 'primary' ion, leading to a shift in transistor threshold voltage when a WGTFT is gated using a medium containing such ions. Quantitatively potential and threshold shift follow a modification of the Nernst equation. Hence measurement of TFT characteristics transduces ion concentration in the aqueous gate medium into a concentration-dependent WGTFT threshold shift $\Delta V_T(c)$, similar as in the traditional ISFET (ion-selective field effect transistor). Here I report investigations on two aspects of ion-selective WGTFTs:

(i) Previous studies on WGTFT ion sensors followed the design of ISFETs and conventional potentiometric ion sensors in so far that they introduced the ionophore within a permeable membrane that is distinct from the transducer. We have demonstrated a simplified ion-selective WGTFT architecture that requires no separate ion- selective membrane. Instead, we added a calcium-selective calix[4]arene ionophore directly to spin casting solutions of the organic semiconductor rrP3HT. We find that resulting WGTFTs cast from ionophore-doped rrP3HT solutions selectively respond to calcium cations dissolved in the gating water with similar characteristics as previous ion- selective WGTFTs. The ionophore-doped rrP3HT simultaneously acts as a semiconductor, and ion- sensitive layer, without the need for a separate ion- selective membrane.

(ii) We have systematically compared the use of hole- vs electron transporting semiconductors in ion-selective WGTFTs. When using the same ion- selective membrane and otherwise identical device architecture to gate either a p-type (solution processed rrP3HT) or an n-type (spray pyrolysed ZnO) semiconductor, we find a systematic difference in WGTFT response characteristics: The hole transporter leads to super- Nernstian response, while the electron transporter shows sub- Nernstian response. We explain this by a capacitive amplification (or attenuation) mechanism based on the ratio of cationic to anionic electric double layer capacitances.

A further study reported in this thesis is on the mode-of-operation in WGTFTs. When the common organic semiconductor 'PBTTT' is used in water- gated thin film transistors, it has so far been found to operate only in field effect (interfacial gating) mode. Electrochemical transistor (volumetric gating) mode, which is actuated by the penetration of waterborne ions into the bulk of the semiconducting film, enables significantly higher transistor currents. However, this has until now been prevented by the hydrophobicity of PBTTT, and could only be observed for derivatives of PBTTT with hydrophilic side chains. We report here for the first time the operation of PBTTT water-gated transistors in electrochemical mode, despite PBTTT's hydrophobicity. This is enabled by a specific choice of the waterborne ion, which apart from its ionic character somewhat resemble typical PBTTT solvents and therefore can penetrate PBTTT bulk.

Table of Contents

List of Figures

List of tables

Chapter 1: Introduction

1.1 An overview of sensor technology

Sensor technology is one of the most exciting areas of study which has been applied in a diverse range of applications [1]. Sensors are analytical devices that are commonly used for such functions as electricity generation [2], environmental monitoring [2-4] and medical diagnosis [5]. To be more specific, sensors can be used to detect air and water pollution, a vital application is given the significant level of pollution in our environment, both in the air and in the water; primary components of life on this planet. To highlight the significance of this, 70% of all freshwater that is used is applied to the field of agriculture [6]. In addition, the main source of the food for much of the world's population is fished from the oceans [6]. However, the pollution of air and water is one of the major problems that is currently threating our life and environment, especially in terms of the health of animals, humans and plants[7]. Major sources of this pollution include heavy industry and transport.

Given these facts, perhaps the most promising application of sensors is in the detection of air pollution. Koolen et al. [7] have presented examples of air pollution that lead to terrible consequences. For example, in 1952, a large cloud of sulphate aerosols suffocated London in fog for two days, killing more than 10,000 people [8]. In addition, in 1985, five days of dense smog covered North-Rhine Westphalia in West Germany. This led to more than 3,500 people being admitted to hospital as a consequence of respiratory and cardiovascular failure. To allow some perspective on this issue, Figure 1.1 presents data illustrating how many megatons of pollutants are estimated to have been emitted in Europe in 2014 as a result of the burning of fuel. As can be seen, the largest contributor is carbon oxide with an output in the range of 23 megatons [7]. However, the environmental impact of CO is less significant to that of NO_x, nitrogen oxides which are known to contribute heavily to air pollution. These include nitric oxide (NO) and nitrogen dioxide (NO_2) [9, 10]. The reaction between nitrogen and oxygen leads to the production of these gases through combustion of fuels – hydrocarbons – in air. At high temperatures, the reaction mostly occurs in car engines [9, 10]. In addition, emission of NO is observed as a main source of air pollution in most countries that have dense motor vehicle traffic, especially in large cities. As shown in Figure 1.2, between 1990 and 2016 in Europe, the most significant contributor to pollution in terms of NO_x was road

transport. It should also be noted that many companies are continuing to produce vehicles that emit levels of pollution higher than recommended and allowed for by law [11].

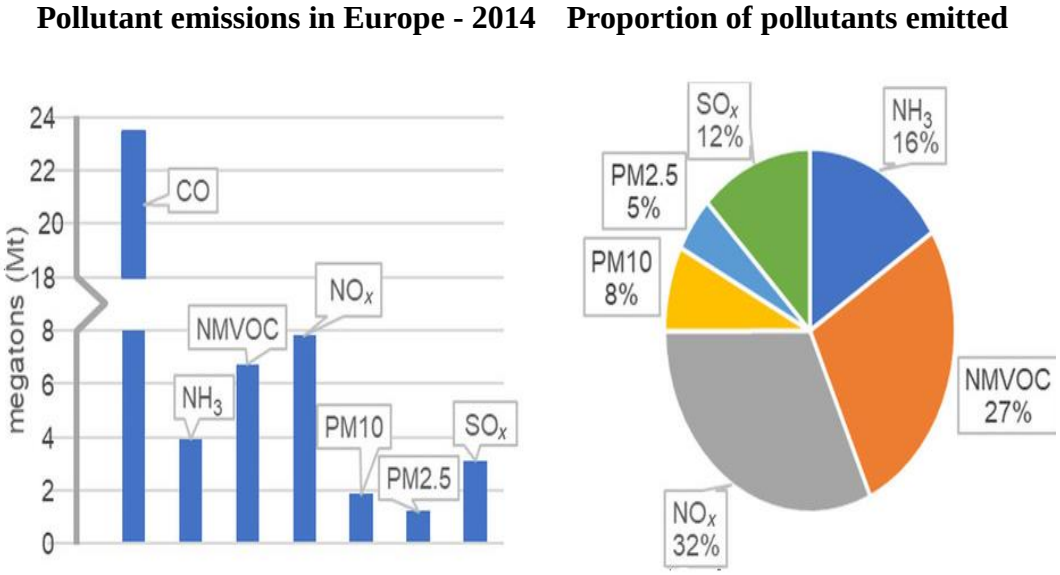

Figure 1.1 *Data indicating the megatons of pollutants estimated to have been emitted from consumption of fuel in Europe in 2014 (left). Pie chart presenting the volume % contribution of each pollutant when carbon oxide is omitted (right) [7].*

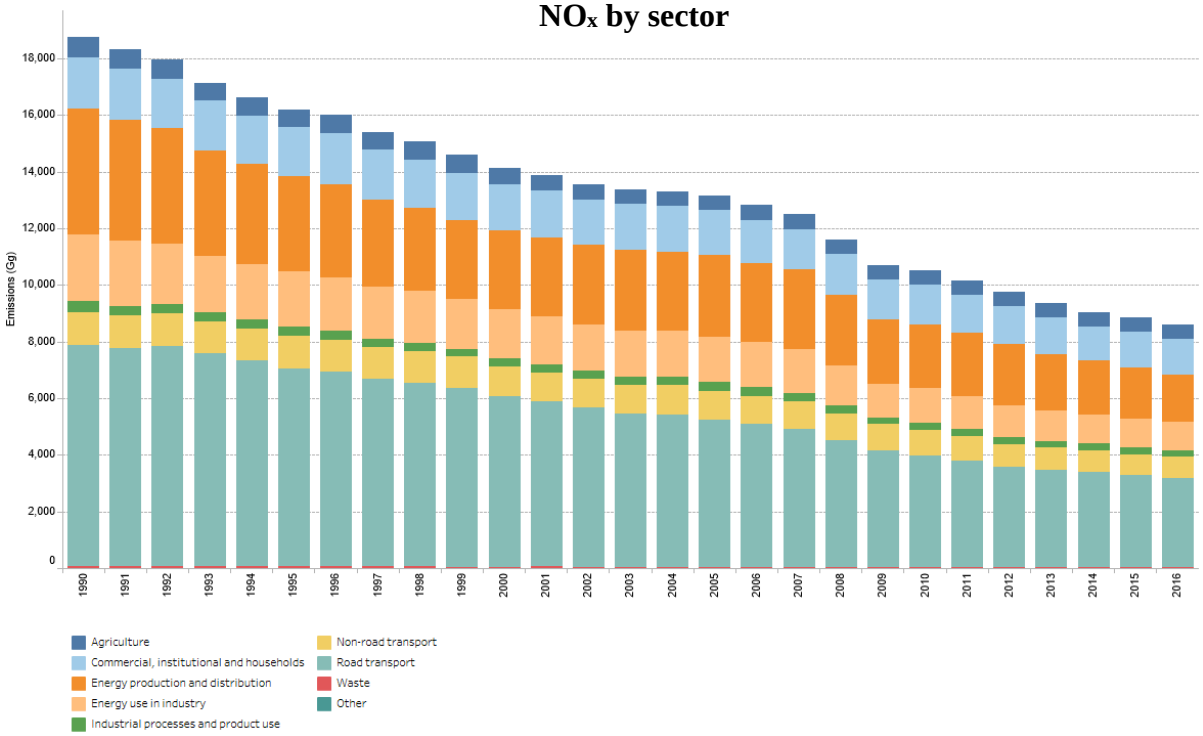

Figure 1.2 *Data indicating the air pollutant emission of NO_x between 1990 and 2016 in Europe [12].*

Another exciting application of sensor technology is in the treatment of diabetes through detection and monitoring of blood sugar levels. This is particularly important given the global increase in the number of patients with diabetes reported in World Health Organisation statistics (WHO). Newman et al. [13] have convincingly argued that the number of people with diabetes will increase to 300 million by 2025: 17.1% of the population of developed countries compared to 154 million in 2000. Diabetes is a medical condition that is caused by insufficient insulin production [14] or abnormal levels of glucose in the body: when blood glucose concentration is lower or higher than the normal range of 80-120 mg/dl (4.4-6.6 mM) [14]. The symptoms of diabetes are numerous and include higher risk of kidney failure and heart disease [14]. As diabetes can cause numerous critical health complications in sufferers, the patient's glucose level must be continuously and accurately monitored so that it can be tightly controlled. The chemical analysis of blood samples is thus used to detect or diagnose whether patients have high levels of glucose in the blood. Millions of tests are used to measure the blood glucose levels daily and so glucose is an extremely commonly tested analyte. In fact, approximately 85% of the entire biosensor market is comprised of glucose biosensors. Due to their importance, researchers are working hard to develop new methods of medical biosensing. For instance, Newman et al. [13] have reported the development of numerous commercial glucose biosensors.

The detection of ions in water is a further area of promise in the field of sensor technology [15-19]. The reason for this is that the World Health Organisation (WHO) have presented guidelines for drinking water quality and thus it is important to monitor the composition of minerals and pollutants contained within it [20]. These guidelines show most of the common minerals that are contained in drinking water, the recommended daily intake of these, and the symptoms of over dosage [20]. One of the most important factors when measuring concentrations of samples is the limit of detection (LoD), the lowest concentration of an analyte that can be detected at a specified level of confidence (more details on this in section 3.4). Some common cations such as sodium, potassium and calcium are essential for the functioning of living organisms [21]. For example, calcium is a very important cation which is a major contributor to bones health and metabolic functions. The typical concentration of serum calcium should be in the range of 8 to 10 mg/dl [22]. When calcium is consumed in concentrations are over this value, it can lead to hypercalcemia. In this case, the patient will suffer from symptoms such as muscular pain and cardiovascular issues [22]. In terms of potassium, the recommended daily intake is 3500 mg, and over dosage may cause stomach

upset [20, 21]. Due to their importance for health, these cations have been studied for biomedical diagnostics, food-monitoring and water control [15, 17].

Heavy metals ions have also formed the focus of studies due to the risk they pose ecologically, nutritionally and environmentally [23]. Of these, (Hg^{2+}, Cd^{2+}, Pb^{2+}..) are the heavy metals found in polluted water and are thus very toxic and extremely poisonous, even at low concentration [23, 24]. The recommended concentration of Pb^{2+} in natural water is less than 0.048 µM. Higher concentrations can lead to health issues [20]. Unfortunately, on some rare occasions, water is polluted with such ions – often through human activities such as mining operations or the use of lead water pipes [25]. Moreover, radioisotope metals such as (Cs^{+}, Sr^{2+} ..) have been released in nuclear accidents such as that at the Fukushima Daiichi Nuclear Power Plant and also in nuclear weapons testing in the 1950s and 60s. The former of these caused significant contamination of seawater [26-28]. Whilst caesium is rarely found in nature; the β^{-} active radioisotope ^{137}Cs is released into the environment when nuclear accidents occur. Thus, detection of Cs^{+} in drinking water (and removal from it) is a requirement to ensure the protection of humans and animals from drinking contaminated water.

It is clear then that the sensing of ions in water is a key application of sensor technology and there are many techniques used by the scientific community to investigate waterborne cations at low concentrations. These include atomic absorption spectroscopy [29], atomic emission spectroscopy [30] and mass spectrometry [31]. It should be noted though that the disadvantage of using these techniques is the need for expensive instrumentation and infrastructure that is, in general, not easily portable to the point of need [32]. A lower cost and more portable alternative has been reported by Kergoat *et al.* [33] in the form of thin film transistors (see section 2.1) which can be gated across water as electrolytic gate medium (water-gated thin film transistors, WGTFTs) (see section 2.3). This technique has paved the way for a new potentiometric transducer concept for detection of waterborne analytes. To be specific, when a WGTFT is sensitised with a suitable receptor (see section 2.4), an analyte borne in the gating water may bind to the sensitiser. This binding is transduced into a change of the WGTFT characteristics, usually a shift in threshold voltage, V_{th} (more details can be found in sections 2.3 and 2.4).

1.2 Structure of the thesis

The overall structure of the thesis is organised into four sections subdivided into nine individual chapters:

Section 1: Introduction and Literature Review

Chapter 1- An overview of sensor technology in general and structure of my thesis.

Chapter 2 - the basic principles of thin film transistors (including their structure and operation), various electrolytes (including water) as a gate medium and the electric double layer. In addition, the basic principles of potentiometric ion sensors.

Chapter 3 - A review of the literature related to a quantitative description of TFT, various practical solutions for processing TFT semiconductors, and properties and mechanisms of organic semiconductors. Following this, we discuss the quantitative and theoretical concept of potentiometric ion sensors.

Section 2: Experimental section

Chapter 4 - A presentation of the method of fabrication of water gated thin film transistors and manufacturing of the transistor substrate which is a pair of opposing contacts, source and drain on supporting substrate connected by a semiconducting film.

Chapter 5 - A presentation of the instruments used to investigate the morphology and properties of TFT semiconductors and electrical characterisation.

Section 3: Results and discussion

Chapter 6 – Results showing that an ionophore-doped semiconductor leads to ion-sensitive WGTFTs without the need for a separate ion-selective membrane.

Chapter 7 - A systematic study comparing cation-sensitive WGTFTs using either a hole transporting semiconducting polymer (rrP3HT) or an electron-transporting precursor-route metal oxide (ZnO) as the semiconductor. Both organic hole transporters and inorganic electron transporters have their relative merits and drawbacks in ion-sensitive WGTFTs.

Chapter 8 - A presentation of results showing that picric acid PA's combination of properties – solubility in water, and similarity to semiconducting polymer PBTTT solvents – leads to organic electrochemical transistor OECT behaviour in PBTTT. Previous studies have shown that organic field effect transistor OFET behaviour only when gated with aqueous media.

Section 4: Conclusion

Chapter 9 - Overall conclusions, and future work.

Chapter 2: Basic principles of thin film transistors and potentiometric ion sensors

In chapter 1, a general overview of sensor technology was introduced. In this current chapter, the basic principles, structure and operation of TFT are described as well as TFT semiconductors. Following this, electrolytes as gate media in TFTs are demonstrated with a particular focus on the most important feature of electrolyte-gated TFTs: an electric double layer (EDL). The chapter ends with the basic concepts of sensors and a discussion of various electrochemical sensors for the detection of ions in solutions - potentiometric sensors.

2.1 Structure and operation of thin film transistors (TFTs)

2.1.1 TFT Structure

Before starting to discuss a thin film transistor (TFT), it is necessary to first explain the function of transistors. These are semiconductor devices that are utilised to amplify electrical signals. In other words, electronic devices that are used to control or switch the current or voltage. They also have the ability to work as a transducer when a sensitiser (explained later in section 2.4) interacts with an analyte which converts this interaction to an electric signal. TFTs were initially proposed and developed by Weimer in 1962 [34]. These are a type of field effect transistor which have three electric terminals: source (S), drain (D) and gate (G), and also include a semiconductor, a gate medium (dielectric or electrolytic as described in section 2.3), and metallic contacts which are compacted together on a non-conducting substrate – often glass.

As shown in Figure 2.1, source and drain are electrical wires that are used as metallic contacts deposited on a non-conducting substrate and separated by channel area: length (L) and width (W). The thin film of the semiconductor layer (described later in section 2.2) is placed or deposited on the source and drain contacts. The gate insulator isolates the gate metal (third terminal) from the semiconductor layer. Usually, silicon dioxide (SiO_2) is used as the common gate insulator material i.e. easily fabricated by thermal oxidation of silicon [35]. However, in our work, we use an electrolyte instead of the gate insulator in the channel between semiconductor and gate metal of TFT for bio-chemical sensor applications [36, 37].

As mentioned earlier, a TFT is utilised to control or switch the current or voltage. It is also a three-terminal device that allows the application of two different voltages (gate V_G- and drain

voltage V_D). In addition, the source acts as though grounded and is used as a reference for the bias applied to the electrodes of the gate and the drain. A current flows between source and drain is known as source-drain current I_{SD} and as well as can be controlled by the gate voltage V_G. When applying the gate voltage, the current is always driven over the semiconductor channel from the source to the drain contact.

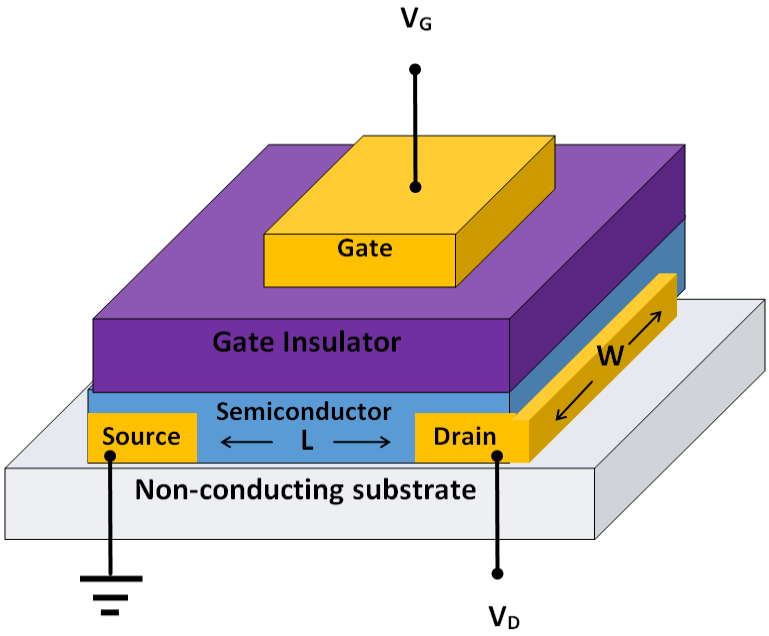

Figure 2.1 *The basic structure of a thin film transistor (TFT).*

The structure of TFT, in principle, is similar to MOSFET (metal oxide semiconductor field effect transistor), but the latter uses a silicon wafer to act as a substrate and semiconductor. It should be noted though that the substrate utilised in MOSFET technology consists of a single Si wafer, and some devices are often required to operate in extremely high temperatures and for costly procedures (e.g. lithography and etching) [38]. TFTs are fabricated using substances that are insulators (glass and plastic). However, vacuum deposition techniques can occur at a lower temperature (<650C) [38]. This means that the active layers of TFTs are normally made up of amorphous or polycrystalline materials. These materials are considered to hold a lower charge carrier mobility than organic and inorganic semiconductors, an undesirable quality [38].

There are several TFT architectures, and this depends on the position of the gate electrode in relation to the active layer, as shown in Figure 2.2 (a, b, c and d). This configuration depends on the position of the source and drain contact (i.e. bottom gate/top contact (Figure 2.2(a)) or bottom gate/bottom contact Figure 2.2(b)) and on the side of the semiconductor or the gate insulator such as top gate/ bottom contact Figure 2.2(c)) or top gate/top contact Figure 2.2(d)) [38-40]. Each of these configurations has some advantages and drawbacks. Due to their improved performance and easy handling, bottom gate structures – especially those which are staggered (see Figure 2.2(a)) – are mostly used for silicon TFTs. However, an additional layer is required in most samples to protect the back channel from being exposed to air and thus preventing undesirable instability effects [38, 39]. Top gate structures, however, especially coplanar (see Figure 2.2(d)), are mainly used when utilising low-temperature polycrystalline silicon (LTPS) technology. This configuration enables deposition and crystallisation of semiconductors at higher temperatures without necessarily damaging other interfaces accomplished in sequential steps [38]. Moreover, with top gate TFTs, the advantage of using the gate insulator is that it can be used as a passivation layer. This leads to a reduction in the number of step patterns [38].

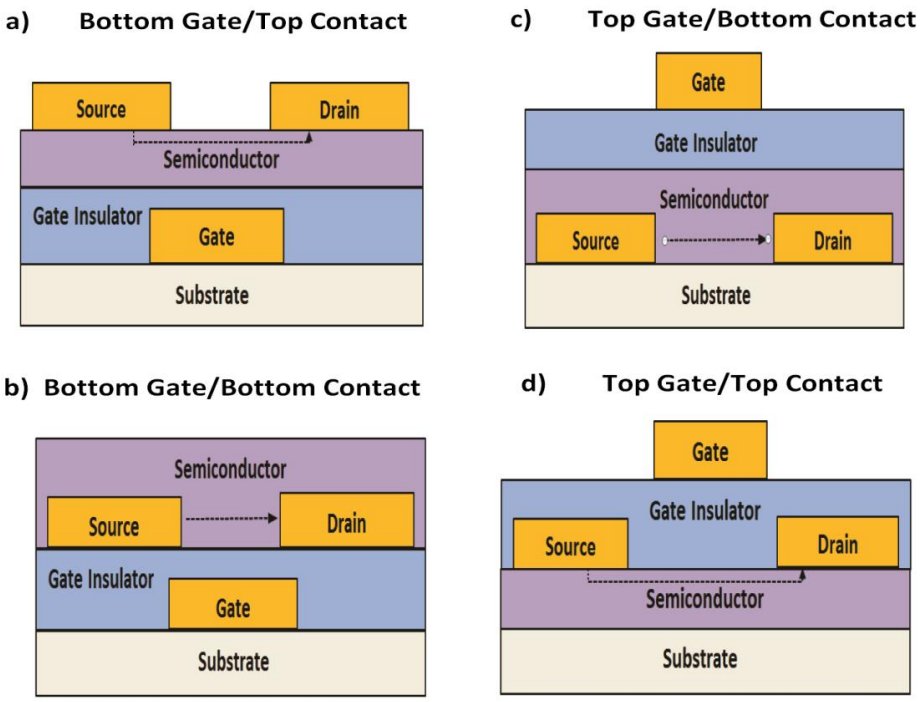

Figure 2.2 *Four common configurations of TFTs based on the gate insulator and contact geometry distribution. Flow of charges in the channel area is illustrated by a dashed black line as well as displaying the injection of carriers charge from source metallic contact.*

2.1.2 TFT operation

The TFT acts and operates on accumulation mode due to most of the materials used in TFTs being intrinsic semiconductors [35, 38]. Thus, as the charge carriers accumulate at the interface between the semiconductor and gate insulator, during the process of application of gate voltage, the transistor undergoes three phases: accumulation mode, depletion mode, and inversion mode [41]. Due to its significance in this current research, accumulation mode of TFTs is discussed here in detail.

In an accumulation mode transistor, an accumulation layer of electrons or holes (for positive or negative gate voltage) builds up in the transistor channel near the semiconductor/gate medium interface when a sufficiently high voltage of appropriate polarity is applied to the gate. This 'sufficiently high' gate voltage V_G is known as the transistor's threshold voltage (V_{th} or V_T), and this makes the transistor channel conductive – we say it 'switches on' (more details on threshold voltage present in section 3.1).

Tanase *et al.* [42] reported certain properties of the accumulation layer; in organic field effect transistors (OFETs), the thickness of accumulation layer is very thin , and this leads to the confinement of one or two molecular layers at the insulator interface and semiconductor. In fact, the accumulation layer is very thin compared to semiconductor films , and the carrier density is comparatively very high – in the range of $10^{19} \sim 10^{20}$ [43].

2.2 TFT Semiconductors

TFTs are used in an extremely wide variety of applications and are thus an area of intense study. These include flat-panel screens, smartphones, computers, and systems for playing video games [44]. Additionally, TFTs have been applied in the field of chemical, physical, and biochemical sensing [44]. A large variety of semiconductor materials, such as silicon, can be used to make TFTs. A feature of the silicon-based TFT is that the crystalline nature of the semiconductor layer can be either amorphous silicon or can be galvanised into polysilicon. Several kinds of organic and inorganic substances have been applied to TFT in scientific studies [33, 38, 45, 46]. Various distinctive substances for organic semiconductors (OSCs) are polythiophenes polymers, an example being poly (3-hexylthiophene) (P3HT), which possesses a highly stable semiconducting nature [15, 47]. There are also oligomers, such as pentacene, which have derivatives that are soluble, and other organic substances that are able to provide high mobility exceeding 1 $cm^2\ V\ s^{-1}$ to organic thin film transistor (OTFT) devices [48]. More details regarding chemical structures are reported later in section 3.2, and the

descriptions of the processing methods (evaporation vs solution) are provided in sections 4.2 and 4.3, respectively.

Other studies have been conducted to determine the optical and electrical properties of metal oxide TFTs (MOTFTs) whose mobility (described later in section 3.2.2.4) is higher than amorphous silicon-based TFTs [38-40]. They also have a transparent visible light region and can be manufactured using low-temperature processes [49, 50]. There have also been intensive efforts to fabricate metal oxide thin film transistors (MOTFTs) using processing methods which reduce the cost of producing metal oxide semiconductor films. Examples of the films include as ZnO [51], IGZO [52], InZnO [53], and In_2O_3 [53]. These offer possible replacements to the conventional technologies based on vacuums such as prompt inorganic condensation [54] and sputtering [55]. In addition, other studies [51, 56, 57] have focused on solution-processed metal acetate, nitrate, or chloride from solution, but not oxide. The oxide forms during processing by spin coating or pyrolysis from the precursor acetate, nitrate and chloride.

In this thesis, two organic semiconductor materials; namely, regioregular poly(3-hexyl)thiophene (rrP3HT) and poly (2,5-bis(3-tetradecylthiophen-2-yl) thieno[3,2-b]thiophene) (PBTTT); and one inorganic semiconducting material, zinc oxide, are used as a basis for experimentation. Extensive details on these are provided in section 3.2.

2.3 Electrolytes as gate media in TFTs

As demonstrated earlier in section 2.1, the gate insulator isolates the gate metal from the semiconductor layer. The crucial aspects of the gate insulator in TFTs are as follows: it improves the performance of a transistor, it is observed with high specific capacitance (discussed later in section 3.1), is based on the applied voltage, and contributes to high charge carrier and lower threshold voltage [58]. There are two parameters which can affect the specific capacitance since the capacitance for a film is proportional to the dielectric constant (k) as well as inversely proportional to the thickness of the film (d).

Silicon dioxide (SiO_2) is the most common gate insulator material utilised in TFTs and integrated circuits. It has a low dielectric constant (k= 3.9) [59],in addition, another disadvantage of using SiO_2 in OTFT's is the existence of a hydroxyl group (-OH) on its surface that act as a trap (described later in section 3.2.2.4). To reduce the –OH group on the surface of SiO_2, the surface can be treated with hexamethyldisilazane (HMDS) (discussed in

section 4.4) or polyethylene [60]. Orit *et al.* [59] have reported many examples of different gate insulators with organic field effect transistors under low voltage. Most of these show a capacitance in the range 1 ~ 100 nF/cm^2. For example, the capacitance(C_i) of rrP3HT with an SiO_2 insulating layer with a 200nm thickness was 15 nF/cm^2 [61].

However, using an electrolyte as a gate medium instead of a gate insulator such as SiO_2 in TFTs has recently become desirable since this leads to their use in many bio-sensing applications. An electrolyte is defined as a material that dissolves in polar solvent or has free mobile ions. Water or salt dissolved in water (e.g. potassium chloride) are common examples of electrolytes. When the salt dissolves in the polar solvent, this leads to the formation of separately charged ions: cations (positive charge) and anions (negative charge). The name of this process known as dissociation. One important factor to note here is the degree of dissociation which leads to the categorization of electrolytes as either weak (i.e. water as discussed later in section 2.3.2) and strong.

There are a range of electrolyte materials that have been used in electrolyte-gated (EG) TFTs. These include poly (sodium 4-styrenesulfonate) PSS [61], Li Perchlorate doped polymer [62], ionic liquid (IL) [63, 64], gelled IL [65], salt solutions [15, 17] and pure water [33]. One purpose of using an electrolyte as a gate medium is to block the flow of current to the gate contact that is insulated rather than conducting. As electrolytes are DC insulators (at least up to a particular voltage) and conduct AC only. The most important advantage of using electrolytes in TFT is leading to high capacitance. In fact, Kergoat *et al.* [33] reported that organic semiconductor films can be gated across a droplet of water using the interfacial electric double layers (EDLs) in electrolytes as high capacitance (1–10 µF/cm^2) and as an alternative to conventional dielectric gate media.

2.3.1 Electric Double Layers (EDLs)

When a pair of electrodes is subjected to electrolyte solution, and a voltage is applied to them, this causes the migration of ions (cations are positively charged, and anions are negatively charged) at the gate electrolyte and semiconductor-electrolyte interface [33, 35]. This in turn leads to the build-up and creation of the electric double-layer (EDL) as shown in Figure 2.3. Note that the positive charge of the electrode is known as the anode and the negative charge of the electrode is known as a cathode. The name of the layer can be distinguished according to the position of ions from the electrolyte; a cationic layer at the cathode and anionic at the anode.

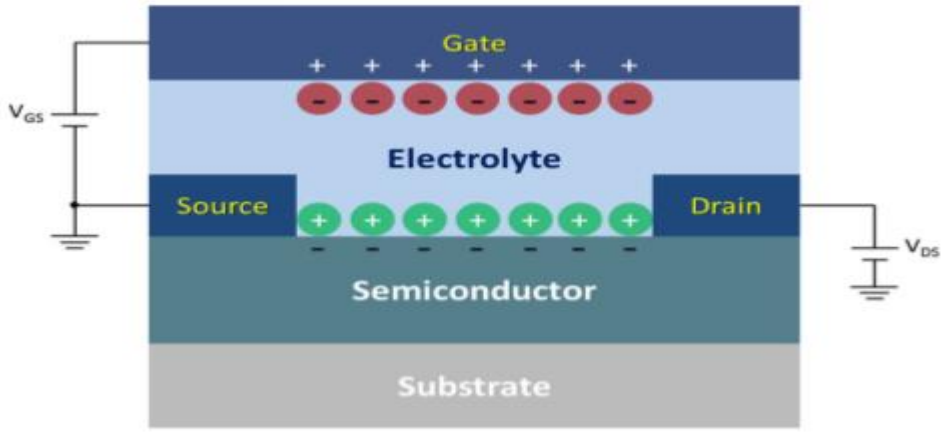

Figure 2.3 *Schematic illustration of the structure of an electric double layer[66].*

The most important property of the EDL is high capacitance since the double layer is very thin approximately 1nm or less [67]. However, the carrier density is very high which illustrates the reason for such a high capacitance [67]. When using electrolytic gate media, the specific capacitance C_i values quoted in the literature; therefore, do vary, albeit they are typically in the range (1-10) $\mu F/cm^2$ [15]. In addition, as we know the capacitor needs two plates, the EDL consists of pairs (cationic and anionic) based on the total EDL capacitance. The law of addition of serial capacitance applies here since the two EDLs are considered a serial combination. As a property for the electrolyte, 'electrochemical window' is a limit to the voltage that can be applied without destroying the electrolyte. When the applied voltage is higher than the electrochemical window, the electrolyte is destroyed electrochemically. For example, the electrochemical window of water is 1.23 V.

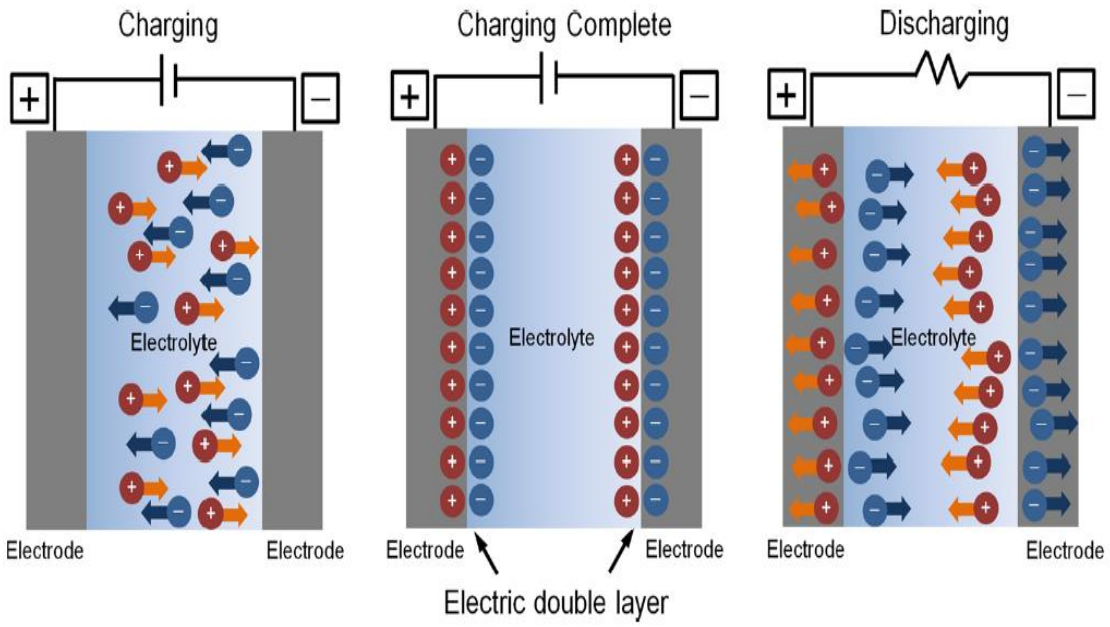

Figure 2.4 *Operation of the electric double layer illustrated by charging and discharging [35].*

The figure above represents the operation mechanism of the electric double-layer capacitor (EDLC). As can be seen, an electrolyte such as a liquid whose cations and anions are mobile is distributed between two electrodes. An electric voltage is applied between the electrodes to form two EDLs between the electrolyte and the electrode. Upon application of an external voltage, the cations and the anions move to the electrode's surface, thus initiating the charging process [35]. The result, when fully charged, is the creation of the EDL. The electrode side of the double layer has a space charge: at the electrolyte, the side is an ion space. Both sides have a space charge layer, but both are very thin. Furthermore, the capacitance is always proportional to the electrode's area. Thus, for every capacitor, we quote specific capacitance (described earlier), and its operation is based on the rate at which the electrical layer absorbs and desorbs ions [35]. On the other hand, the discharge process occurs when removing the external voltage and simultaneously using a load resistance that in this case leads to the ions moving away, as shown in Figure 2.4.

In 2015, Du *et al.* [35] presented a review of models; namely the distribution of ions and field in the electrolyte of an EDL based on EDL theory. The earliest model was investigated by Von Helmholtz in the 19th century and was thus named the Helmholtz model. In this model, a thin layer of counter ions is created near the electrode's surface and is surrounded by solvent molecules such as water. However, the solvent molecules lead to the ions being prevented from conducting the electrode's surface since the distance (d) is very small and isolates ions

from the electrode's surface. This process is known as the Helmholtz plane. When balancing occurs on electrodes by counter ions, the electric potential falls through the layer, but the rest potential in the bulk electrolyte is zero. Therefore, in the EDL, the electric field is concentrated. However, this model fails to indicate whether measured capacitance is dependent on the electrical potential of the electrodes and the electrolyte concentration.

The Gouy-Chapman model followed on from Helmholtz's model with modifications. Taking into consideration the effect of thermal motion on the attracted ions' distribution, the Gouy-Chapman (GC) model proposes that there is an exponential fall in the electrical potential away from the electrode. This leads to the formation of two distinctive layers; the Helmholtz layer and the diffusing layer which contain negative and positive charges. Despite the GC model predicting that the capacitance is dependent on the potential and concentration, it failed to match the results of experiments: the suggested model gives higher than measured capacitance. Stern then integrated the Helmholtz model and the Gouy-Chapman model, as seen in Figure 2.5 (c). This consists of a Helmholtz plane (HP) and a diffuse layer [35]. In this model, there is a distance separating the inner and outer Helmholtz planes consisting of specifically absorbed anions and non-specifically absorbed ions. This distance increases with respect to the rate of increase in the concentration of the ions. Due to the formation of the HP layer, the potential ψ at the interface between the electrolyte and the electrode begins to drop. These EDLCs display high capacitance (~430 μF cm^{-2}) [68] and large carrier density (~10^{14} cm^{-2}). They also have a very rapid response to the external electric field [35].

In cases in which the external voltage is low enough such that it cannot induce an electrochemical reaction, the EDLTs anions are aligned close to the surface, and the holes or the electrons are gathered on the surface of the electrode forming a two-dimensional electron for the attainment of phenomena such as superconductivity [67].

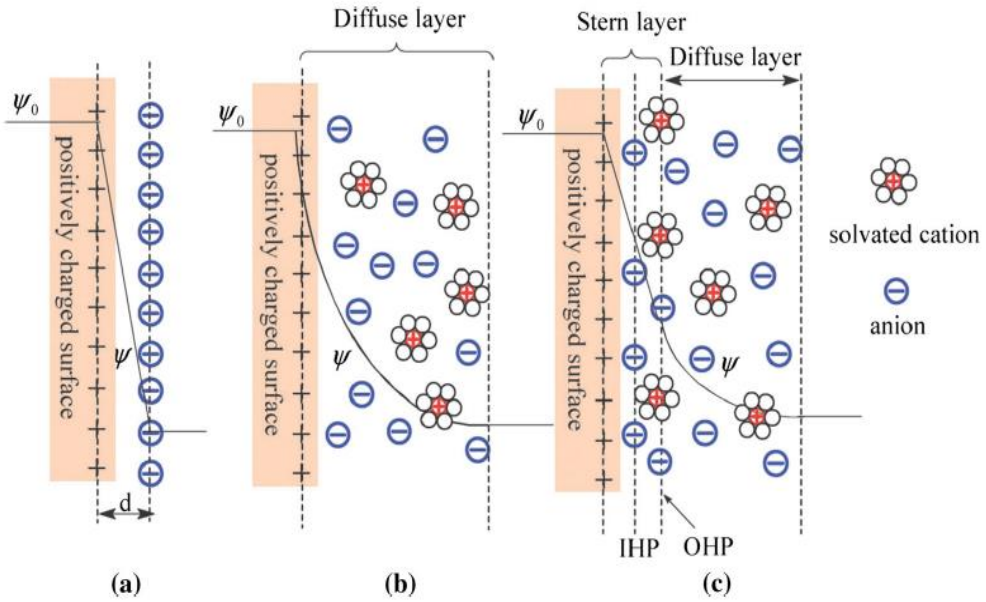

Figure 2.5 *The development of the electrical double layer as presented in three models: (a) Helmholtz model, (b) Gouy–Chapman model, and (c) Stern model [35].*

2.3.2 Electrolytes

2.3.2.1 Aqueous media

- DI water

Deionised water (DI) refers to very pure water which has had any dissolved salts removed. Nevertheless, autoprotolysis separates a very small fraction of water molecules into hydronium ions (H_3O^+) and hydroxide ions (OH^-), as in the following equation [69]:

$$2\ H_2O \leftrightharpoons\ H_3O^+ + OH^-$$

Chemical equilibrium for any compound or material that has autoprotolysis as a property is heavily weighted towards the non-dissociated side [69]. At a temperature of 25 ^oC, the concentration of H_3O^+ is only 10^{-7} mole/L. Pure water has an electrical conductivity of 5.5×10^{-6} S/m (18 MΩ.cm electrical resistivity) owing to the H^+ and the OH^- ions produced when water attains a dissociation equilibrium [69]. Moreover, the electrochemical window of water is approximately 1.23 V [70]. The typical WGTFT thresholds are lower than the electrochemical window. If they were not, WGTFT operation would not be possible at all.

- Phosphate buffer saline (PBS)

PBS is a buffer solution (water-based salt solution) consisting of a compound such as disodium hydrogen phosphate and sodium chloride, as well as, other ions, i.e. potassium chloride and potassium dihydrogen phosphate. A buffer solution is frequently used in many biological applications, especially ion concentrations of the human body and when washing cells. The pH of the buffer solution is 7.4, and its importance is that it helps to maintain a constant pH whilst being nontoxic to most cells. Using a buffer solution as an electrolyte in WGTFT leads to high current and high capacitance since it is very concentrated compared to DI water [66].

2.3.2.2 Ionic liquid

Ionic liquids are organic salts that have melting points below room temperature [71, 72]. These have several advantages for use as electrolytes: their near-zero volatility, the fact that they are thermally, chemically and electrochemically stable [72], and their high EDL capacitance. The estimated value of conductivity of ionic liquids is 0.1 (S cm^{-1}) [73]; the reason being ionic liquids have a higher concentration than DI water whose concentration is low due to the limited dissociation of the water molecules. An example of an ionic liquid reported for use with an organic field effect transistor (OFET) [74] is displayed in Figure 2.6 below.

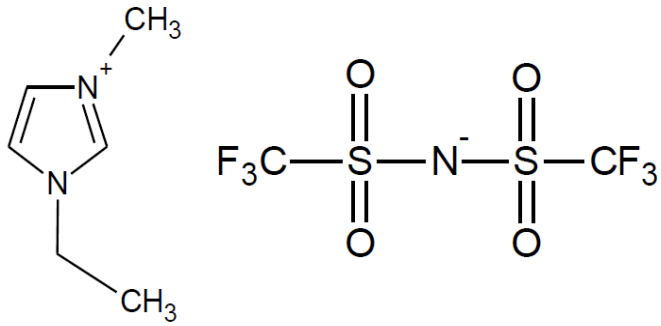

Figure 2.6 *The chemical structure of the ionic liquid 1-ethyl-3-methylimidazolium-bis(trifluoromethyl-sulfonyl)imide ('EMITSFI') [74].*

The electrochemical window of this ionic liquid is 4.3 V, higher than all aqueous media's electrochemical windows [75]. Moreover, it shows high capacitance with P3HT OFET: approximately ~30 μF cm^{-2} at 10 Hz [75]. As a matter of fact, the capacitance of EDL remains higher than aqueous electrolytes with frequencies reaching into the KHz. With these two features combined, it is clear that compared to water, ionic liquid has a maximum

possible gate electric displacement ($D = C_i \times V_{window}$) approximately ten times higher. Its application in FETs enables the achievement of low voltage, with FETs being observed not to interfere with the mobility of the organic semiconductor.

2.4 Potentiometric ion sensors

2.4.1 Basic concept of sensors

In the following section, the most common potentiometric transducer concepts are first introduced followed by a discussion of ionophore and ion-selective membrane (ISM) formulations. Moreover, the most common class of electrochemical ion sensors – potentiometric sensors – are presented.

First of all, a sensor is an analytical device that is used to detect and distinguish the concentration of analytes in the ambient environment. Sensors are classified in general into 'physical' and 'chemical' sensors according to their applications. Sensors can operate in different media, most commonly air or aqueous media. However, chemical sensors typically contain two key elements: the sensitiser or receptor, and the transducer (described later). Sensitisers are characterised by their ability to interact and bind selectively with a particular analyte such as chelators [76], macrocycles [77] or enzymes [78]. This leads to a change in a physical quantity or characteristics between the bare sensitiser and the sensitiser/analyte complex. In addition, the transducers convert the change of molecular property that results from sensitiser/analyte binding into a measurement. This is the sensor's response. Transducers have to be adapted to the sensitiser according to what particular physical property is affected by analyte/sensitiser binding. Common examples of transducers are colorimetric [79], fluorometric [80], amperometric [81, 82] and potentiometric[83, 84]. In this thesis, one type of potentiometric is used: a water-gated thin film transistor.

2.4.2 Ionophores and ion-selective membranes (ISMs)

All potentiometric ion sensors in common use a so-called 'ionophore' as an ion-selective sensitiser. This is a chemical substance which binds to particular ions, constitutes the ion carrier or ionophore [85], and is capable of transferring ions from hydrophilic media, including water itself, into hydrophobic media, such as a biological membrane in which ions would typically be insoluble [85, 86]. In most cases, the ionophore is embedded in an ion-selective membrane (ISM) that commonly consists of plasticised poly(vinyl chloride) (PVC) [15, 17] filled with the ionophore and sometimes an ion exchange medium. ISMs build up a

membrane potential depending on the identity and concentrations of ions in the adjacent aqueous media, which can then be transduced into a voltage reading with different transducer concepts. It is interesting to note their use as ion-selective sensitisers within ion-selective membranes (ISMs). In this study, ionophores were used as they have been found to have significantly selective metal cation complexes within their central cavities. Some practical examples of ionophores, such as calixarenes [87, 88] and crown ethers [89], are discussed below.

2.4.3 Practical examples of ionophores

2.4.3.1 Calixarenes

Calixarenes are macrocyclic molecules that Gutsche introduced in 1978 by condensing cyclic oligomers from formaldehyde and p-substituted phenols [90]. The term calixarene is formed from the word chalice (or calix) as the molecule bears semblance to a vase, and the word arene, a term for aromatic hydrocarbons. It contains hydrophobic cavities which can hold small ions or molecules and belongs to the cavitands class, which means container-shaped molecule [91]. The chemistry of calixarenes is characterised by versatility [90]. The recurring calixarene unit can be pyrogallol or phenol, and they have easily distinguished functionalisation both at the lower and upper rim which provides an extensive array of compounds [92]. Figure 2.7 shows some examples of calixarenes. Note that the [4] and [6] in calix[x]arene denote the number of units in the ring. Moreover, calixarenes are usually insoluble which qualifies them for use in WGTFTs as the ionophore can be immobilised in a membrane that is in contact with water without leaching [93].

As an example of this, calix[4]arenes tetraesters have been shown to exhibit selectivity to sodium cation [94]. It was found that the existence of t-butyl clusters within the upper rim compelled the calixarene into a fixed cone that enabled the esters to create the required coordination cavity. The hexamer esters (calix[6]arenes) exhibited less affinity to sodium cations but showed affinities for caesium, rubidium, and potassium cations. Therefore, creation of bigger cavities creates room for more effective binding of bigger metallic cations.

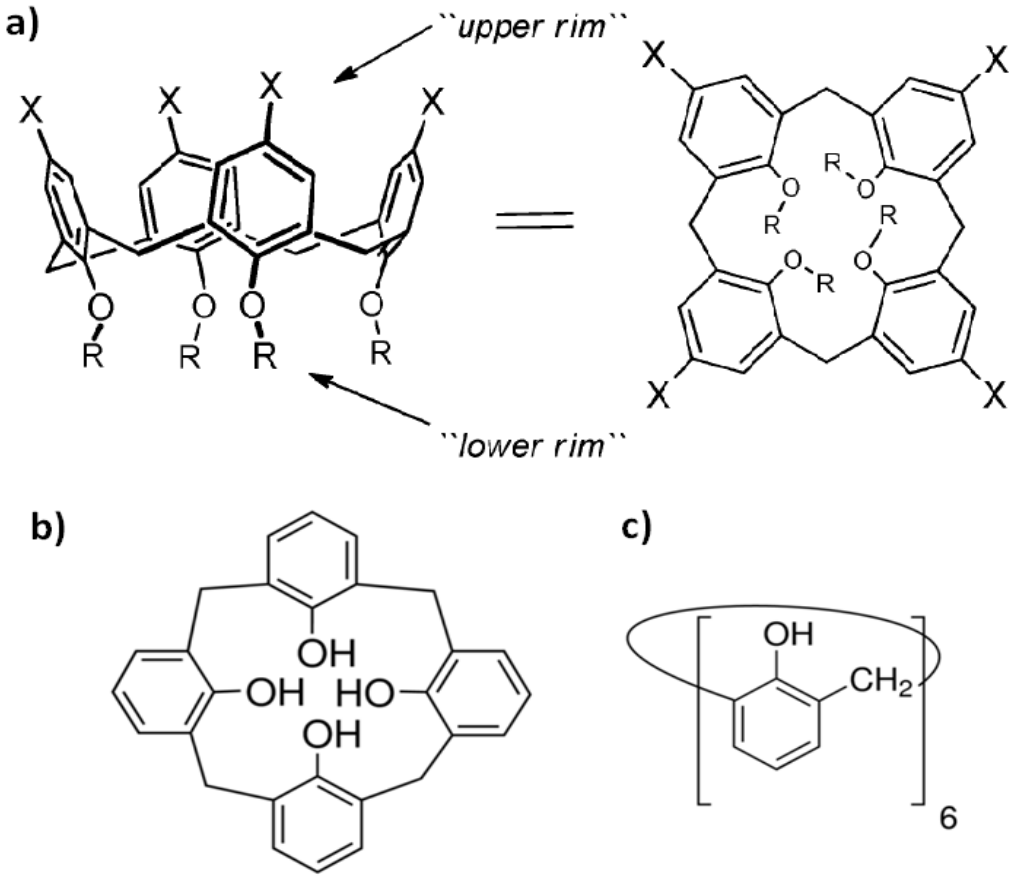

Figure 2.7 ***(a)*** *Chemical structure of two forms of a calix[4]arene, presented differently to show the lower and upper rim with different functional groups R and X [95]* ***(top)*** *and the chemical structure of a generic* ***(b)*** *calix[4]arene and* ***(c)*** *calix[6]arene* ***(bottom)***

McKittrick *et al.* [96] investigated one example of calixarene (*p-tert*-butylcalix[4]arene phosphine oxide) that was utilised alongside a PVC membrane electrochemical transducer (reported earlier in section 2.4) to identify water-borne calcium ions.

2.4.3.2 Crown Ethers

Crown ethers can be defined as cyclic chemical compounds that have a multiple ether-group ring, the most popular of which are ethylene oxide-cyclic oligomers, with ethyleneoxy[-CH_2CH_2-O-][97] emerging as the recurring unit. Hydrophobic ethylenic groups surround the chemical structure of the crown ether that features a hydrophilic ether oxygen atom-cavity. The crown ether wrap-around on metallic ions enhances solubilisation of metals to organic solvents [98]. The O atoms within the crown ether cavity have a significant affinity to alkaline and alkali earth metallic cations, resulting in the creation of complex compounds. The main aim of designing new crown ethers is to distinguish 'ion selectivity'. In addition, the complex formation of a chemical compound is very important and in crown ether is largely dependent on cation size and cavity size. For instance, 18-crown-6 has good

coordination with potassium (18 refers to the number of atoms in the cycle and 6 represents the number of those atoms that are oxygen) whereas sodium ions fit well within a 15-crown-5 cavity [97], as shown in Figure 2.8.

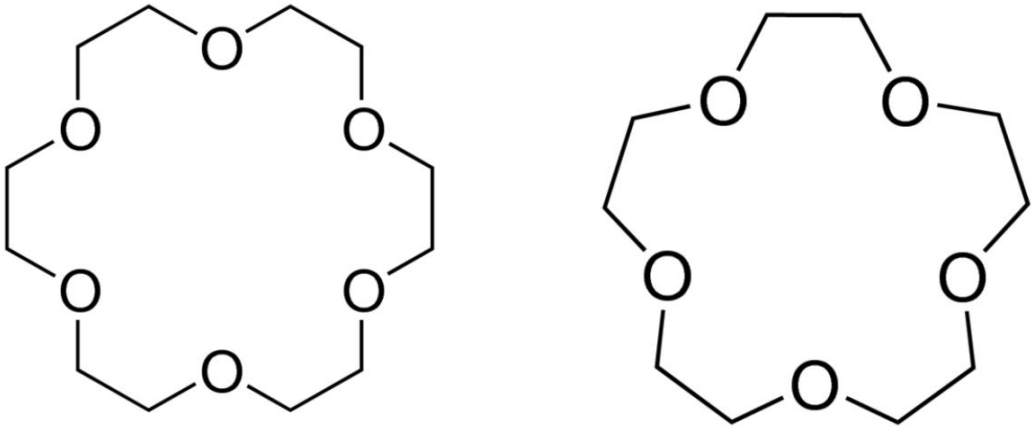

Figure 2.8 *Chemical structure of 18-crown-6 (left) and 15-crown-5 (right).*

Calixarenes have the same ability of selectively accommodating ions within their cavities. Molecules of crown ether have gained considerable attention within several fields. Their extensive application spectrum includes medicinal applications and ion sensors [97]. One example of crown ether, which is investigated in this present work, is *Dibenzo-30-Crown-10* that selectively complexes potassium ions (K^+) in its central cavity, as reported by Pedersen *et al.* [89]. More details related to crown ethers in ion-sensitive water-gated transistors with organic and inorganic semiconductors are presented in chapter 7.

2.4.4 Examples of potentiometric sensors

2.4.4.1 Classic potentiometry

In terms of the history of electrochemical sensors for the detection of ions in solutions, the first potentiometric sensors which used a potentiostat in conjunction with an ion-selective electrode (ISE), such membranes were originally developed between the early and mid-1960s [99]. This is what can be termed ‘classic’ or ‘conventional’ potentiometry, as shown in Figure 2.9 (a). The system consists of two compartments separated by an ISM. One compartment contains a reference solution of known ion concentration; the other contains the sample solution with unknown analyte ion concentration. The ISM builds up a membrane potential that is related to the difference in analyte ion concentrations between the two compartments.

Two identical electrochemical reference electrodes are immersed into the compartments, one in each. Despite being identical, their potential will now differ due to the membrane potential. This potential difference is read by a high impedance voltmeter, usually a potentiostat taken from cyclic voltammetry [100], but here simply used as a voltmeter. This provides a near zero-current sensing system based on the potential difference across the ISM. The quantitative relationship between the (initially unknown) ion concentration in a sample solution and the resulting membrane potential [101] is reported in section 3.4.

2.4.4.2 Ion-selective field-effect transistor (ISFET)

In 1970, Bergveld proposed a much simplified potentiometric ion sensor: the ion-selective field-effect transistor (ISFET) [102, 103] where originally, the gate insulator of a field effect transistor was in contact with a sample solution. This is a type of potentiometric device which operates in a similar way to the MOSFET (TFT reported earlier in section 2.1). In its original form, Bergveld's device was a pH sensor, with H_3O^+ a special case of ion that leads to surface potential by protonation/deprotonation of the amphoteric inorganic oxide surface such as the FET's gate insulator, SiO_2. However, in this form, it cannot sense any metal ions, only pH. The interface potential consequently changes the current through the transistor, or more precisely, it changes the FET's threshold voltage (explained later in section 3.4). In later work, Moss et al. [104, 105] introduced ion-selective membranes instead of the gate metal to sense metal ions rather than just pH as shown in Figure 2.9(b), i.e. potassium ISFET, and calcium ISFET. Unlike conventional potentiometry, ISFET directly transduces membrane potential into a high current signal, albeit the sensing mechanism itself is entirely potentiometric, requiring no current at all. Moreover, no reference solutions are needed. This provides the ISFET with many benefits including a high response rate, reduced size in comparison to conventional potentiometry and voltammetry, and low output impedance [19].

2.4.4.3 Water-gated field-effect transistor (WGFET)

The discovery of Kergoat *et al.[33]* that water can act as an electrolytic gate medium for thin film transistors (TFTs) has paved the way for novel 'electrophysical' rather than electrochemical transducers for waterborne analytes. In principle, analytes may be electrically neutral solutes (e.g. [106],[45]), or ions (e.g.[15, 17]). Our work focuses on ionic solutes. Since transistor threshold voltage is sensitive to interfacial potentials, water- gated TFTs (WGTFTs) that incorporate suitable sensitisers ('ionophores') display a shift of transistor threshold voltage (V_{th}) in response to waterborne ions. Some researchers work on ion-selective WGTFTs followed the design of traditional electrochemical transducers by

introducing the ionophore dispersed in a plasticised membrane as an additional component into the WGTFT architecture[15, 17].

Much more recently in 2013, List-Kratochvil *et al.* [15] revealed the possibility of combining a water-gated field effect transistor (WGFET) as a transducer with an ion-selective membrane (ISM) as an active sensing component. This builds on the earlier discovery of Kergoat *et al.* [33] that organic semiconductor films can be gated across a droplet of water using the interfacial electric double layers (EDLs) in electrolytes as a high capacitance (1–10 μF/cm^2) alternative to conventional dielectric gate media [35] (electrolyte-gated TFTs are discussed earlier in section 2.3). The design of List-Kratochvil *et al.* [15] is shown in Figure 2.9(c), using an organic semiconductor as in the original WGFET [33], and a two-chamber design with chambers separated by an ISM (in this case, selective to sodium, Na^+) similar to conventional potentiometry. Other than in the ISFET, the aqueous analyte solution is simultaneously an active part of the transducer.

In later work, Melzer *et al.* [17] designed a probable method of achieving a specific selectivity detection of an electrolyte-gated FET without the need for a reference solution. When constructing a PVC membrane, a special type of ISE was used to allow the construction of smaller and long-lasting solid-state electrodes. The configuration of the coated wire electrode involved coating the polymeric membrane onto a conductive surface such as a metal wire. To aid in distinguishing between the primary and interfering ions, the features of the transistor were analysed and the main parameters – threshold voltage V_{th} , mobility μ and the transconductance g_m – were extracted [17]. As a result, their simple design succeeded in demonstrating a good response towards the specific ions K^+ and Ca^{2+} with the limit of detection between (100nM~ 1μM.)

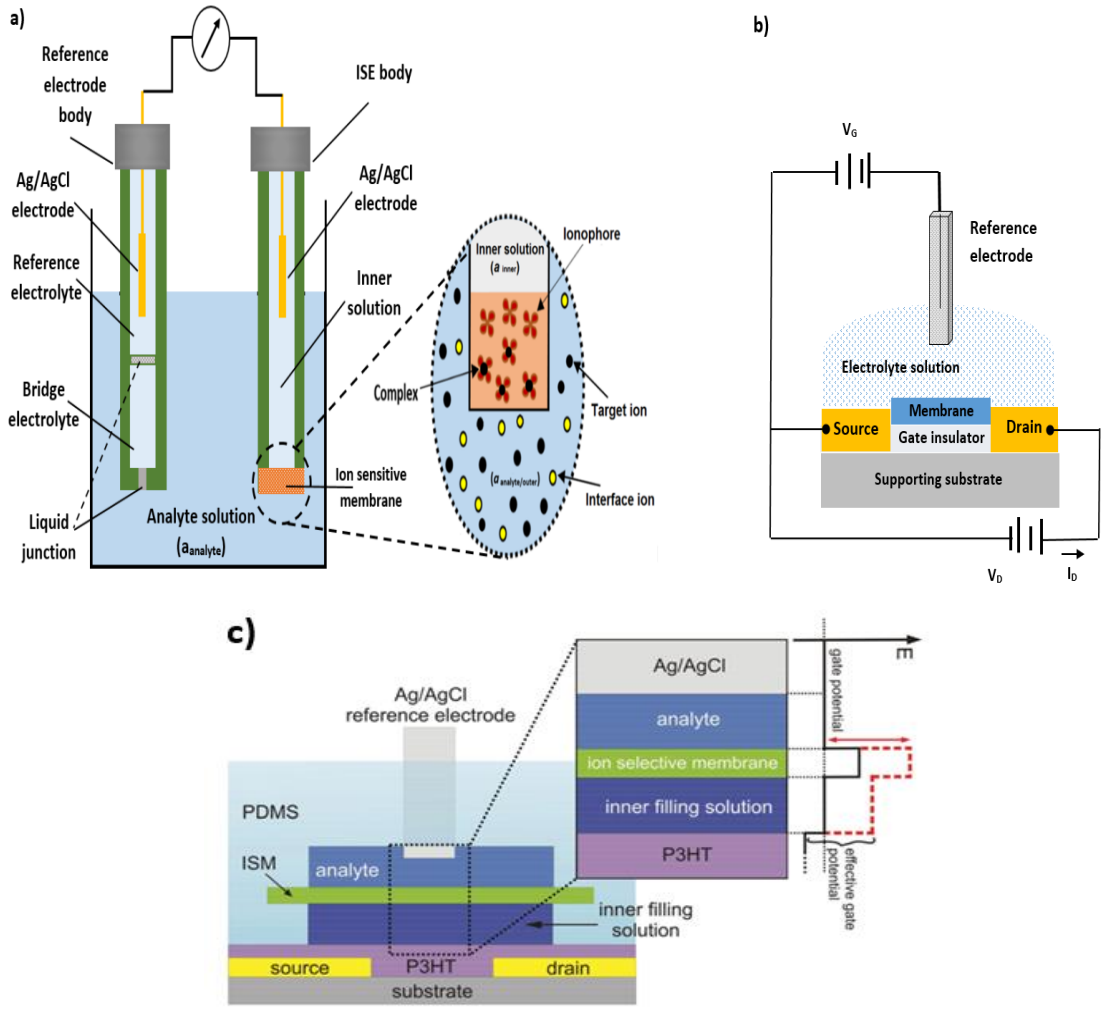

Figure 2.9 *Schematic diagram of three types of transducers:* ***(a)*** *conventional potentiometric or electrochemical transducer,* ***(b)*** *ion-sensitive FET [105]and* ***(c)*** *ion-sensitive WGOFET designed by List-Kratochvil group [15].*

This thesis reports further improvements to the WGFET ion sensor concept, revealing advantages of the WGFET over the ISFET. In chapter 6, a membrane-free WGTFT ion sensor is reported, and in chapter 7, a capacitative amplification mechanism that enhances ion sensitivity.

Chapter 3: Theory and Quantitative Concepts

In chapter 2, the basic principles of thin film transistors and potentiometric ion sensors were presented. In the following chapter, we begin by presenting a quantitative description of TFT devices in section 3.1. This is followed by an explanation of practical solution-processed TFT semiconductors, inorganic semiconductors, organic semiconductors (OSCs) including conjugation and band gap, benzene and thiophene rings, charge carrier injection in OSC, transport of charge carrier and mobility, and certain organic materials that are used in this work. In section 3.3, the behaviour of organic electrochemical transistors (OECT) is compared to electrolyte gated OFETs. Finally, in section 3.4, we discuss the quantitative concepts of ion sensing; namely, Nernst vs Nikolsky Eisenman equations, membrane potentials, and the concepts of sensitivity, selectivity and limit of detection.

3.1 Quantitative description of TFT

The basic principles of *TFT* operation were presented in section 2.1 and its quantitative operation is described in this present section. As the transistor is a three-terminal device that allows application of two different voltages (gate voltage V_G- and drain voltage V_D), there are two experimental modes of transistor characterisation: the output characteristic and transfer characteristic. The transfer characteristic is where drain current I_D is determined against V_G while maintaining constant V_D. When such characteristics are determined at high/low V_D, this is known as the saturated/linear transfer characteristic (described below). In contrast, the output characteristic can be defined as the state in which I_D is determined against the V_D while retaining the V_G in a constant condition. Output characteristics are usually presented as a family of V_D scans taken at different V_G. More details regarding the output characteristic and transfer characteristic are presented in chapter 5, section 5.2.

In an accumulation mode transistor, an accumulation layer of electrons or holes (for positive or negative gate voltage) builds up in the transistor channel near the semiconductor/gate medium interface when a sufficiently high voltage of appropriate polarity is applied to the gate. This 'sufficiently high' gate voltage V_G is known as the transistor's threshold voltage (V_{th} or V_T), and this makes the transistor channel conductive: we say it 'switches on'. The magnitude of V_{th} depends on several parameters including the specific capacitance of the gate medium C_i and the work functions W_F of gate and source metals, as seen in Eq. (3-1) [107]:

$$V_{th} = V_{FB} + \frac{qp_0 d_s}{C_i} \qquad 3\text{-}1$$

There are a number of contributions in Eq. 3-1 aside from V_{FB} which are determined by the characteristics of the materials which utilise W_F of the gate metal: either the electron affinity E_a of n-type or ionisation potential I_p of p-type in the semiconductor (discussed later in section 3.2.2.3). It should be noted that there is a difference between the fermi energy in the metal from that in the silicon substrate. In addition, the bending of energy bands is formed at V=0 and it should be eliminated [35]. With the increasing applied bias, the band bending becomes flat at a particular magnitude of voltage known as V_{FB} [35] or we can say it is "the gate bias at which charge first appears in the channel". This occurs prior to the creation of the accumulation layer.

Therefore, V_{th}, and V_{FB} can be written as:

$$V_{FB} = W_F - I_p \quad \text{Or} \quad V_{FB} = W_F - E_a \qquad 3\text{-}2$$

In Eq. 3.1, q represents (+/-) one elementary charge (+ for holes / - for electrons), p_0 represents the trap density in semiconductor bulk and the interface of semiconductor/insulator), d_s denotes the thickness of the semiconductor film, and C_i represents the capacitance per unit area of the gate medium. In the case of a dielectric gate medium (insulator), C_i can be formulated as:

$$C_i = \frac{k\varepsilon_0}{d} \qquad 3\text{-}3$$

Where k denotes the permittivity of the gate insulator, ε_0 represents the vacuum permittivity, and d is the thickness of the gate insulator. However, in section 2.3., it has been noted that with electrolyte gate media a high C_i is desirable to keep V_{th} low. The typical value of V_{FB} is smaller than 1 V. 'Normally on' is also known as depletion mode; however, in our work, we focus on accumulation mode. It should be noted that V_{FB} is almost always smaller than 1V but not all transistors are normally on. As such, most WGTFTs are normally in the off state.

The other contribution to V_{th} results from carrier traps in the semiconductor and at the semiconductor/insulator interface. This contribution is moderated by the gate medium's specific capacitance C_i. With high C_i (as in 'electric double layer' (EDL) gated devices

discussed earlier in section 2.3.1), the trap contribution to threshold can be moderated and $V_{th} \approx V_{FB} < 1$ V is achieved.

In the first, when the V_G applied has a negligible magnitude compared to that for V_{th} - ($|V_G| < |V_{th}|$) known as the subthreshold - there is no formation of an accumulation layer and the drain current is very small. Nevertheless, drain current can be determined and increases exponentially when the V_G increases until the attainment of the threshold. The drain current is expressed using Eq. (3-4) when the transistor functions are within subthreshold regime (discussed below) [107]:

$$I_D = K\mu C_i \frac{W}{L}\left(1 - e^{\frac{-qV_D}{K_B T}}\right) e^{\frac{qV_G}{nK_B T}} \qquad 3\text{-}4$$

Where K denotes a constant for a specific structure of the device and the materials used, μ represents the charge carrier mobility (discussed later section 3.2.2.3), L and W represent the length and width of the channel, respectively, q represents the charge of the elements, K_B represents the Boltzmann constant (~1.3806 × 10^{-23} m^2 kg s^{-2} K^{-1}), and T denotes the temperature. In addition, n represents the ideality factor $n = (1+C_s/C_i)$ where C_i denotes the specific capacitance of the gate medium and C_s includes both bulk traps in the semiconductor and interface traps, respectively.

Subthreshold slope (S) is the quantity that characterises the increase of drain current with gate voltage in the subthreshold regime. The inverse subthreshold slope or subthreshold swing ($\mathcal{SS}$) describes the transition between the TFT's 'Off' and 'On' states; a smaller swing leads to sharper switching. The subthreshold swing ($\mathcal{SS}$) is defined as [107]:

$$SS = \frac{\partial log_{10}(I_D)}{\partial V_G} \qquad 3\text{-}5$$

The unit of subthreshold swing $\mathcal{SS}$ is mV/dec. Since the inverse subthreshold slope is relevant to the ideality factor n, the equation 3-5 can be written in this form [107]:

$$SS = \ln(10)\frac{nK_B T}{q} \qquad 3\text{-}6$$

For instance, at a temperature of 300 k, Eq.(3-6) can be simplified into [107]:

$$SS = 60\,{}^{mV}/_{dec}\left(1 + \frac{C_s}{C_i}\right) \qquad 3\text{-}7$$

This allows evaluation of C_s from measured transistor characteristics. However, according to equation 3-7, both C_i and C_s are considered to minimise and reduce the magnitude of subthreshold swing. Since in a thin film transistor, low voltage switching occurs between two states – off and on – a very small magnitude of $\mathcal{SS}$ is required. Bao *et al.* [107] have reported the magnitude of $\mathcal{SS}$ in OTFTs mostly in the range of 500 mV/dec to 5V/dec. On the other hand, Majewski *et al.* [108] have demonstrated that the magnitude of $\mathcal{SS}$ is 130 mV/dec when utilising dielectric as a gate medium (high capacitance) and with low operation voltage. Kim *et al.*[58] have presented the value of $\mathcal{SS}$ as very low in the range of 70 mV/dec because using an electrolyte with OFET as a gate medium leads to high capacitance and minimises the subthreshold swing.

Now, above threshold, the operation of TFT can be divided into particular regimes based on the magnitude of gate voltage V_G with regard to drain voltage V_D and V_{th} as shown in Figure 3.1. These include saturation regime and linear regime. When V_G surpasses V_{th} then the saturation and linear regimes occur. As demonstrated earlier, controlling the drain current I_D can be achieved with two voltages: drain voltage V_D and gate voltage V_G.

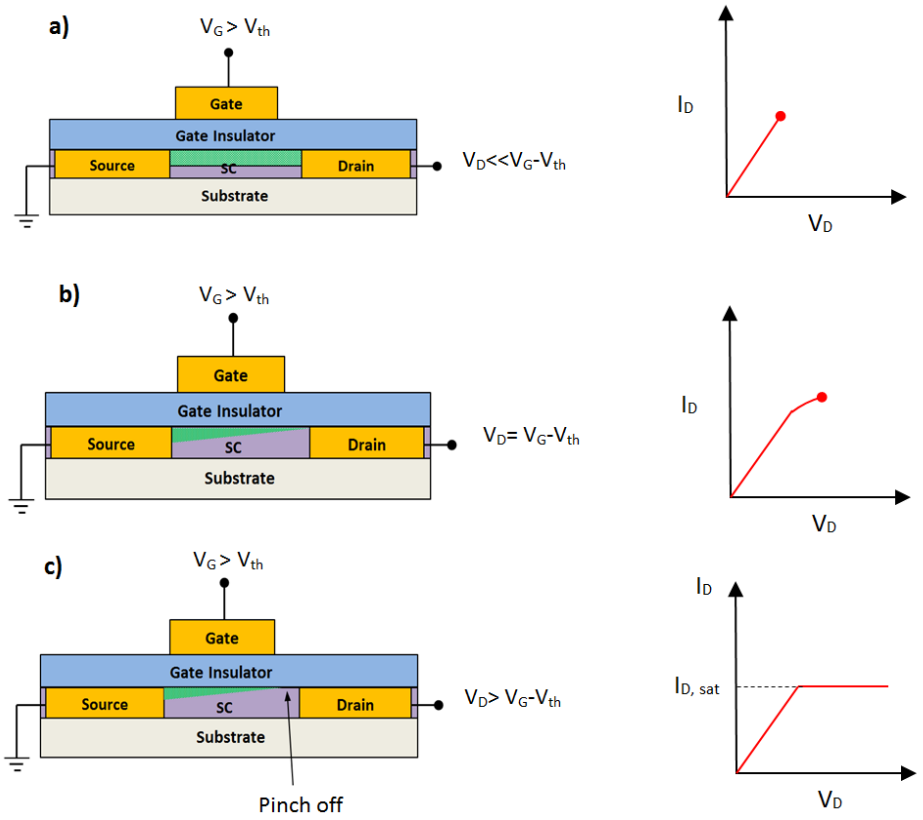

Figure 3.1 *Field effect transistor operating regimes are demonstrated by output characteristics:* ***(a)*** *in the first is the linear regime, in which ($V_G > V_{th}$), $V_D << V_G - V_{th}$ .In this regime, the accumulation layer of carriers is fully developed.* ***(b)*** *represents the start of drain current saturation when (in the output V_D is ramped, V_G is constant)$V_D = V_G - V_{th}$. In this regime, the accumulation layer of carriers is shown as triangular and TFT reaches pinch-off in this case I_D tends to be independent of the applied V_D and starts to saturate.* ***(c)*** *denotes the saturation regime at $V_D > V_G - V_{th}$. Here the accumulation layer pinches off within the channel, and leave a carrier-depleted regime within the channel [109].*

In the regime, when V_D is smaller than the difference between the threshold voltage and the gate voltage, drain current is given by Eq. (3-8) [107]:

$$I_D = \mu C_i \frac{W}{L}\left((V_G - V_{th})V_D - \frac{V_D^2}{2}\right) \qquad 3\text{-}8$$

For $V_D << V_G - V_{th}$, the quadratic term within V_D can be ignored. Thus, Eq. (3-8) can be expressed as [107]:

$$I_{D,lin} = \mu C_i \frac{W}{L}(V_G - V_{th})V_D \qquad 3\text{-}9$$

Hence this is known as the linear regime $I_D \propto V_D$, as found in ohmic resistors. In the regime whereby V_D exceeds the difference between threshold voltage and gate voltage ($|V_D| \geq |V_G - V_{th}|$), the transistor's drain current is given by Eq. (3-10) [107]:

$$I_{D,Sat} = \mu C_i \frac{W}{2L} (V_G - V_{th})^2 \qquad 3\text{-}10$$

Note that this is Eq. 3-8 for $V_D = V_G - V_{th}$. However, I_D no longer increases when V_D increases further. This is known as drain current saturation, and the physical cause is the process known as pinch-off (described by Figure 3.1(c)). Drain current can be increased further only by increasing the V_G.

According to practical measurements of output and transfer characteristics in two different regimes, it should also be noted that Eq's 3-9 and 3-10 can then be used to extract quantities such as mobility in both regimes, on / off ratio, threshold voltage, transconductance g_m and subthreshold slope from measured characteristics. These are discussed in more detail in section 5.2.1.3.

3.2 Practical solution-processed TFT semiconductors

3.2.1 Precursor-route inorganic semiconductors

Inorganic semiconductors exhibit rather a wide spectrum of physical properties and thus can be fabricated as device platforms for various applications including energy conversion, photonics, and electronics [110]. Contrasted against metals and polymers, semiconductors are particularly suited to application in photonic and electronic biointerface studies due to their ability to be configured into multi-functional devices such as switches and sensors with ideal characteristics (i.e. signal transduction and amplification) [110]. In addition to this, inorganic components provide certain advantages; specifically, different mechanisms of signal transduction at biointerfaces. Moreover, high charge carrier mobility within inorganic materials, fast responses, and higher sensitivity in inorganic devices allow more accurate investigation of complex biological dynamics than can be attained using organic components [110].

A thin solid film might be deposited from the precursors in solid, liquid, or vapour phases (or integration of numerous phases) depending on the nature of the precursor as well as the required functionality for the resulting thin solid film [111]. Chemical and physical methods of vapour-phase deposition include epitaxy and sputtering [111]. Such processes need well-controlled settings and are often undertaken within a vacuum using energy-intensive processes and expensive equipment [111]. In contrast, solution-processed methods of deposition constitute another method used to allow cheap solution-processed TFTs to be commercialised for use in sensor arrays, flexible displays, and flat-panel display backplanes [111]. Examples of this type of process include spray pyrolysis [51] (discussed later in section 4.3.2), inkjet printing [50], and spin coating [57], all of which are each characterised by certain benefits which lend them to specific uses.

3.2.1.1 Zinc oxide (ZnO)

Zinc oxide (ZnO) occurs naturally in the earth's crust as the mineral zincite. Interestingly though, most ZnO utilised for commercial purposes is produced via synthetic techniques [112]. Zinc oxide is non-toxic and exhibits compatibility towards human skin. For this reason, it is often used as an additive for surfaces and textiles which come into contact with the skin [112]. As an important semiconductor attracting technological and scientific interest, zinc oxide has a wide band gap (3.37 eV) and has outsized exciton-binding energy (60 meV) [113]. Due to the unique electrical and optical characteristics [114], it is regarded as a potential component within optoelectric applications for operating in visible and near ultraviolet spectral regimes [112].

The most prominent zinc oxide crystal structure is the 'Wurtzite' structure: the thermodynamically stable phase of zinc oxide [115] (see Figure 3.2). The structure consists of a hexagonal lattice containing two interlinked O^{2-} and Zn^{2+} sub-lattices. Each Zn^{2+} undergoes coordination through tetrahedra of O^{2-} and vice-versa. Because the zinc oxide structure phase exhibits stability at ambient temperature and pressure, it is unnecessary to preserve zinc oxide within a vacuum in a similar manner as OSCs.

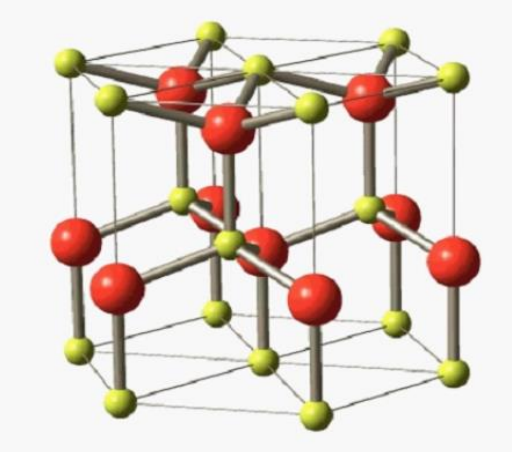

Figure 3.2 *Crystal structure of ZnO (wurtzite); (yellow is Zn and red is O) [116].*

In most instances, zinc oxide constitutes *n-type* semiconductors unless intentionally subjected to doping to exhibit p-type behaviour (n-type and p-type are discussed in section *3.2.2.4).* This can be attained through various growth techniques to introduce an accurate dopant concentration through an ion implantation technique [117]. Even though p-type conductivity in zinc oxide films has been cited, reliable and reproducible zinc oxide with high-quality p-type conductivity is yet to be achieved [115]. In addition, Bayraktaroglu *et al.* [118] have reported that the electron mobility of TFT is more significant which is very high and in the range of 110 cm^2V^{-1} s^{-1}. In comparison, Lee *et al.* [119] investigated hole mobility of ZnO and found it to be 7.8 cm^2V^{-1} s^{-1}. This can be attributed to the fact that carrier mobility within the valence band is lower than the carrier mobility within the conduction band. This is because the valence band within p-type zinc oxide is largely formed from oxygen *p* orbitals, thus reducing the mobility of the carrier [40].

In 2007, Ong *et al.* [120] found that semiconducting films of the II-VI semiconductor ZnO could be prepared through pyrolysis of the organic precursor zinc acetate (ZnAc) which dissolves in benign solvents (mixtures, ketones, alcohols). Since water-gating for precursor-route ZnO was confirmed [121], it has emerged as a common semiconductor for use within electrolyte-gated thin film transistors (TFTs) [122]. However, zinc chloride ($ZnCl_2$) rather than ZnAc precursor solution is now often converted by spray pyrolysis directly onto a hot substrate [64]. More discussions of $ZnCl_2$ as a precursor solution are reported in section 4.3.2.1.

3.2.2 Organic semiconductors

The advantages of using organic semiconductor materials as an alternative to the inorganic semiconductors are twofold: they open the possibility of engineering their bandgaps with chemical synthesis, and they require low temperatures for processing. They also often provide solutions that have the potential for economic device production and flexible applications. It should be noted that the type of bonding within organic semiconductors is largely different from that in inorganic semiconductors [123]. Organo-molecular crystals form Van-der-Waals- bonded solids, suggesting an intermolecular bonding that is significantly weaker than semiconductors that are covalently bonded such as with Si [123]. The implications are observed within thermodynamic and mechanical properties - for instance, lower melting point or hardness - and even within the significantly weaker electronic wavefunction delocalisation among adjacent molecules that directly impacts charge carrier transport and optical characteristics [123]. Within polymers, the situation tends to be different because polymeric chain morphology can result in enhanced mechanical characteristics.

3.2.2.1 Conjugation and band gap

To understand low bandgap and charge transport in organic materials, it is necessary to first introduce the electronic configuration for carbon atoms before moving on to a discussion of conjugation. Organic materials are defined as molecular compounds that contain at least one carbon-to- hydrogen bond. The electronic configuration for C is [$1s^2 2s^2 2p^2$], as shown in Figure 3.3. This suggests that carbon can form two chemical bonds; it forms four. The valence orbital hybridisation theory is used to account for this behaviour wherein it is assumed that a single *s* electron is promoted towards the last free *p* orbital, forming a total of four single valence orbitals. The remnant 2s along with all or some 2*p* orbitals are then combined to form new orbitals, the so-called *sp* hybrid orbitals. The number of *p* orbitals utilised within the process of hybridisation describes the polymer type and its structural and chemical characteristics. Three hybridisations can be achieved: *sp*, sp^2 and sp^3, where the superscript denotes the number of *p* orbitals' involved in the hybridisation process, as illustrated in Figure 3.3.

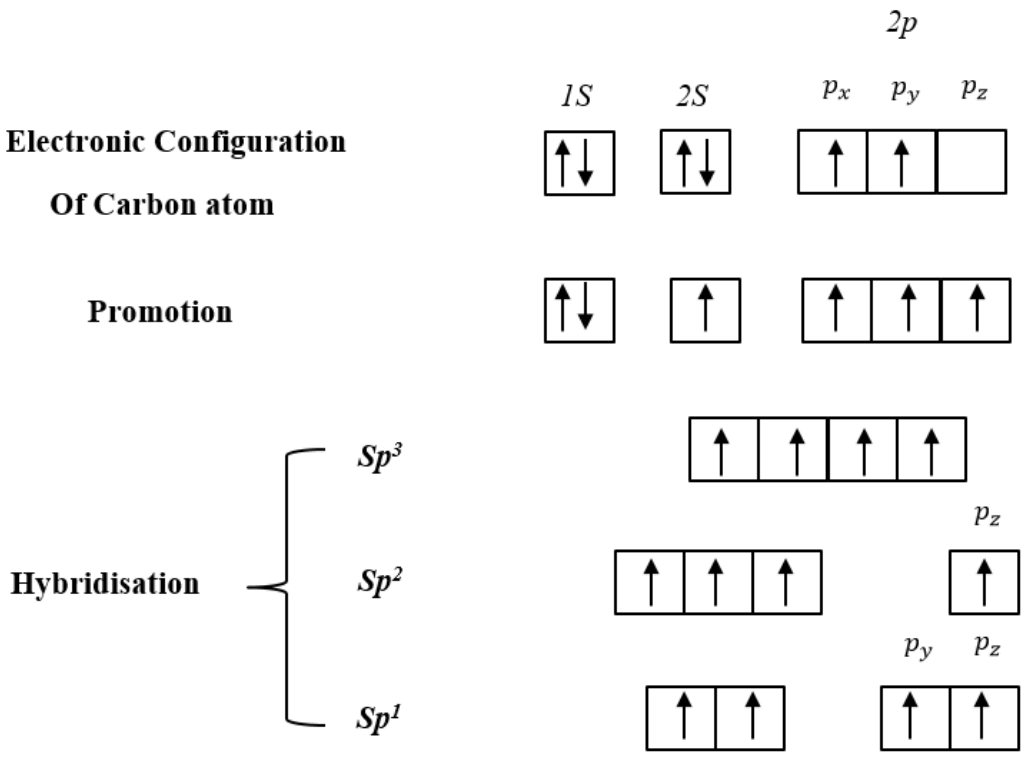

Figure 3.3 *Electronic configurations of a carbon atom which illustrate promotion and 'hybridisation'.*

In the case of sp^3 hybridisation, four equal singly occupied orbitals are formed, pointing into the four corners of a tetrahedral with an angle of 109.5 degrees between any two of them. These can then form four chemical bonds by overlapping with other singly occupied orbitals; for instance, the 1s orbital in hydrogen or another sp^3 hybrid. Bonds resulting from hybridised C orbitals are known as σ bonds. The structure of sp^3 is shown in Figure 3.4(a). When carbon forms molecules in this way, they are termed 'saturated' which is a molecule in which all C's are saturated. Since the energy needed for promotion of electrons from (bonding) σ orbitals towards an excited ('antibonding') σ* orbital is rather high – approximately 6 eV [124] – compounds within this category lack the properties of semiconductors.

In the case of sp^2 hybridisation, three segments are equi-spaced on a single plane with an angle of 120 degrees between them, as shown in Figure 3.4(b). However, there is one remaining orbital (p orbital) perpendicular to the single plane. To create or form a molecule, another sp^2 hybrid needs to be presented. Due to the strong σ bond (discussed in sp^3) as well as the weaker bond which is created from overlap of their perpendicular p orbitals, both hybrids are linked together. The weaker bond is known as π bond, and the particular contributed or shared electron is assigned as a π electron. The two bonds between them are

defined as a double bond (C=C). It should be noted that π bonds are weaker since their particular orbitals are at a greater distance from their parent nuclei, leading to π electrons being more loosely bound to them.

In the case of *sp* hybridised orbital, two segments of the orbital are on the x-axis, and the other remaining p orbitals are on the y- and z-axes which are perpendicular. When both *sp* hybrids are combined, the molecule is formed. According to the combination, three bonds are formed: the σ bond between the orbitals of the particular x-axis and two π bonds between the perpendicular p orbitals. The three bonds of 1.21 Å length are formed at an angle of 180^{o} and defined as a triple bond (C≡C). The structure of *sp* is shown in Figure 3.4(c).

Delocalisation of the π-electron occurs between the two atoms both below and above the molecular axis. A double bond is shorter than a single bond: the double bond length is 1.34 Å, whereas the length of single bond is 1.54 Å [125].

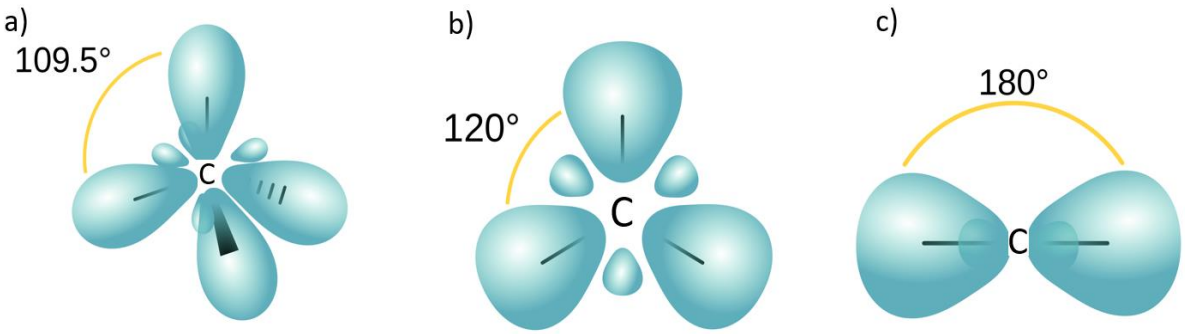

Figure 3.4 *Examples illustrating the shape of the carbon atom in three hybridization orbitals;* ***(a)*** *structure of (sp^3),* ***(b)*** *structure of (sp^2) and* ***(c)*** *structure of (sp) [126].*

When along the backbone of a carbon-based molecule, single carbon-carbon bonds alternate with carbon-carbon double or triple bonds, such a molecule is called 'conjugated'. Conjugation leads to delocalisation of π electrons over large distances, far away from their 'parent' atom. Delocalized π electron clouds decrease the spacing in energy between ground and excited states. In conjugated molecules including ~10 or more carbon atoms may have an energy spacing between 'highest occupied molecular orbital' (HOMO, ground state) and 'lowest unoccupied molecular orbital (LUMO, lowest lying excited state) of only a few eV; in other words, into the range of semiconductor band gaps E_g. Poly (acetylene) is a common example of a conjugated polymer that consists of hydrogen and carbon atoms in a linear

chain as shown in Figure 3.5. However, conjugation often also occurs in ring-shaped molecules.

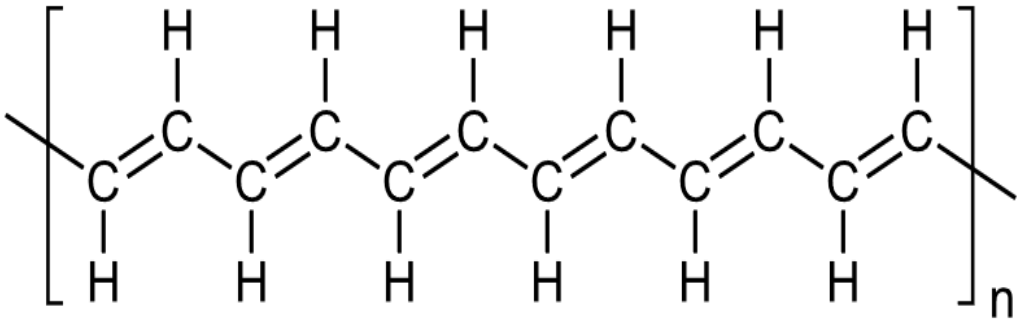

Figure 3.5 *molecule structure of poly (acetylene).*

Organic semiconductors are commonly classed into two categories: polymers and low-molecular-weight materials [127]. Both are characterised by a conjugated π -electron system created by the overlap of sp^2-hybridized C atom p_z orbitals over distances larger than immediately neighbouring C atoms (see Figure 3.3). Unlike the σ bonds forming the backbone of the molecule, π bonding is considerably weaker. In view of this, the lowest electronic excitation for conjugated molecules include the π - π* transitions, which have an energy gap mainly in the range of 1.5 - 3eV. This results in absorption (and sometimes, emission) of light within the visible spectral range. Notably, a molecule's electronic characteristics are dependents on several factors such as electron withdrawing, or donating groups and length of conjugation. Therefore, organic chemistry provides extensive possibilities for the tuning of optoelectric behaviour of OSC materials.

3.2.2.2 Benzene and thiophene ring

As alternating carbon single/double bonds form an angle of 120^o and a sequence of six sp^2 hybridised C atoms can form a planar ring in the shape of a regular hexagon. In this so-called benzene ring – as illustrated in Figure 3.6(a) – π electrons delocalise around the entire ring. While such rings still do show a bandgap larger than typical semiconductors, they constitute an important building block in many organic semiconductors (*OSCs*). It is important to note that benzene rings can be part of larger conjugated structures; for example, they can be 'daisy chained' by linking or connecting them together at two of their corners. At opposite corners, the linkage known as 'para', at neighbouring corners known as 'ortho', or in between known as 'meta'. Neighbouring rings are linked in a similar fashion so that they can still rotate around the link. Nevertheless, rings can also be fused together at two neighbouring corners,

forming rigid planar conjugated systems known as ‘acenes’ .For example, pentacene contains five linearly fused rings of benzene, as shown in Figure 3.6(b), and belongs to the acene family that has been widely investigated as an OSC [128] [129].

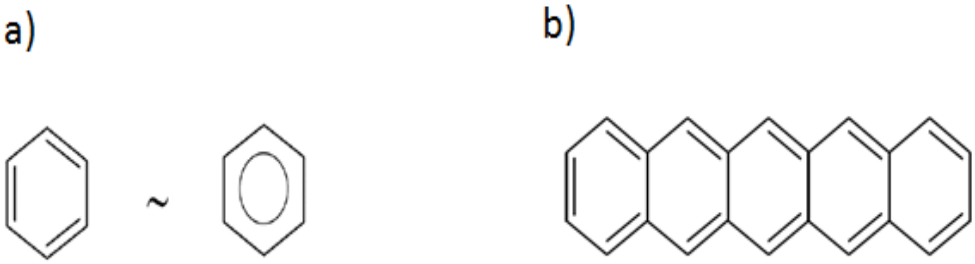

Figure 3.6 (a) *Benzene ring structure and* ***(b)*** *molecule structure of pentacene.*

Thiophene exemplifies a structure known as heterocycles: conjugated rings containing both carbon and other atoms. Thiophene is a 5-membered ring (pentagon) including a sulphur atom and four carbon atoms, as illustrated in Figure 3.7. Again, a single thiophene ring does not yet have a band gap sufficiently small to be classed as semiconductor, but the ring is a key component in several OSC materials such as hexithiophene (linear sequence of 6 thiophenes), or the polymers abbreviated as P3HT and PBTTT (also including fused thiophene rings), which are described later in section *3.2.2.5*.

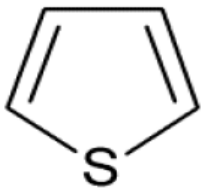

Figure 3.7 *Thiophene ring structure.*

3.2.2.3 Charge carrier injection in OSCs

Charge carrier injection is an important factor to ensure the optimum performance of OSCs. This requires carriers to cross the interface between a metal electrode and the OSC. Holes and electrons are injected into the highest occupied molecular orbital (*HOMO*) in the case of p-type OSCs (discussed later in section 3.2.2.4) and lowest unoccupied molecular orbital (*LUMO*) in the case of n-type OSCs (discussed later in section 3.2.2.4), respectively.

As shown in Figure 3.8, injecting of holes and electrons changes the conformations of molecular orbitals and positions of nuclei that in turn react through relaxation towards new minimum energy positions. Due to robust coupling between the local lattice relaxation and charge carrier, removing electrons from the energy level necessitates slightly less energy than the HOMO suggests, and addition of electrons provides the molecule with slightly more energy than the LUMO suggests. As a result, a polaron (either hole polaron or electron polaron) results from the distortion of the conjugated chain according to the action of the charge [129]. The energy needed to transfer an electron from the *HOMO* level to the vacuum level, which means hole injection, is known as ionisation potential ($\mathbf{I_p}$), and the energy gained when an electron transfers from the vacuum level to *LUMO* level is known as electron affinity ($\boldsymbol{E_a}$).

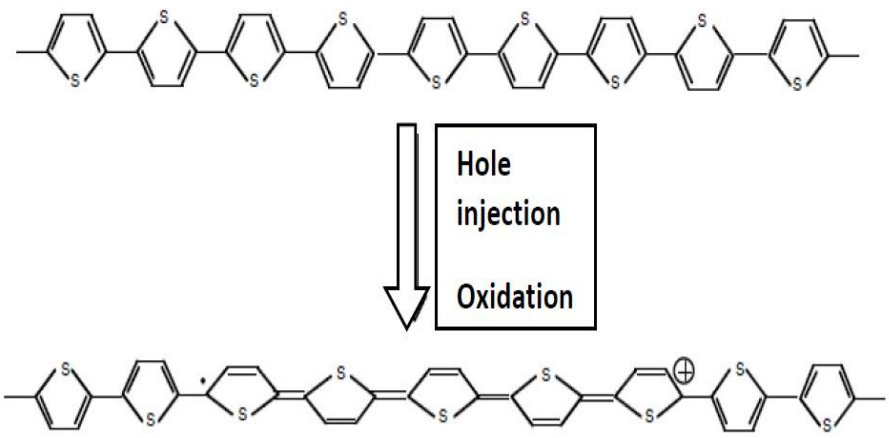

Figure 3.8 *Example of a polythiophene segment showing that injecting of holes changes the conformations of molecular orbitals and positions of nuclei.*

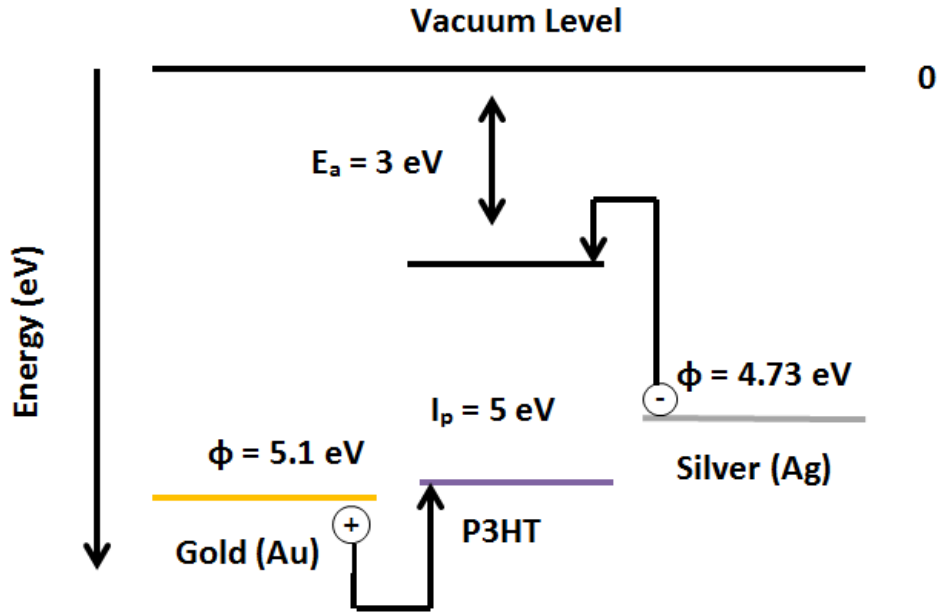

Figure 3.9 *The energy level diagram for OSC 'P3HT' contacted with different metals – gold (Au) and silver (Ag). The energy barriers for hole/electron injection are illustrated. Note, before applying a potential there is no injection.*

For efficient injection of electrons/holes into OSC materials, the injection barriers separating the electron affinity/ionisation potential and the electrode work function must be overcome. Figure 3.9 shows an example of an organic semiconductor (P3HT) located between two electrodes of metal. The horizontal lines in Figure 3.9 display the carrier energy at a specific region. In the first case, when the P3HT/silver is at the interface, the offset between the work function of silver and the electron affinity of P3HT displays an 'injection barrier' of 1.73 eV. This would cause difficulty for the injection of electrons into P3HT. In the second case, when the gold/P3HT is at the interface, the injection barrier for an electron injection is higher (2.1 eV) because the gold has a high work function. However, the injection of holes into the *HOMO* of P3HT (i.e. the extraction of electrons from the HOMO) is barrier-free, since the gold metal has a work function which is lower than the ionisation potential of P3HT.

The simple means of decreasing the injection barriers involves using a deep organic semiconductor *LUMO* with high electron affinity or through selection of low working function metals for injecting electrons and high HOMOs or high work function metals for injecting holes. This method was employed by Ahles *et al.* [130] who used calcium contact (2.8 eV) for electron injection to attain the pentacene transistors' *n*-channel operation (*LUMO*=2.5 eV). After the application of the voltage between the contacts, HOMO / LUMO

levels tilt as a result of the electric field that now spans the OSC layer, as illustrated in Figure 3.10. The energy level gradient is given by E = V/d, where V is the voltage and d is the thickness.

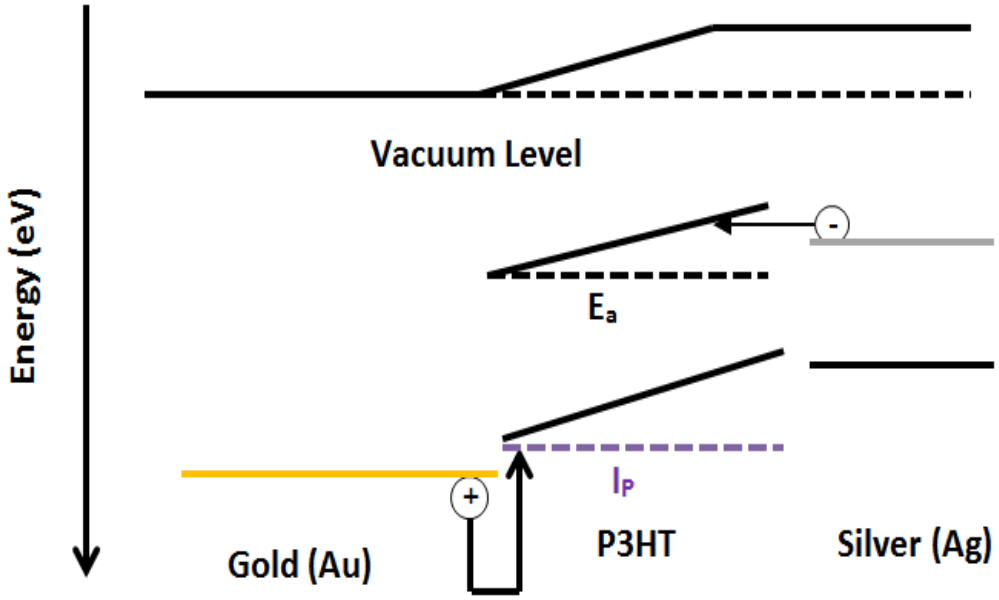

Figure 3.10 *The level of energy of a polythiophene semiconductor (P3HT) when applying bias to Au and Ag electrodes.*

Two separate mechanisms lead to injection of carriers from metal electrodes into an OSC even in the presence of injection barriers and are illustrated in Figure 3.11: thermionic emission and Fowler-Nordheim tunnelling. Thermionic injection is controlled by the probability of a charge carrier being thermally activated to sufficient energy to overcome the injection barrier, which strongly depends on temperature. In contrast, Fowler-Nordheim tunnelling is quantum mechanical tunnelling under the injection barriers. The Fowler Nordheim tunnelling rate is controlled by the distance from the injecting electrode when the tilted energy level first drops below (electron injection) or rises above (hole injection) the work function of the injecting contact. In other words, it strongly depends on the applied voltage.

Thermionic injection is described by the Richardson-Schottky equation as follows:

$$J_{RS} \propto T^2 \, exp\left(\frac{\phi_B}{KT}\right) . exp\left(\frac{\beta_{RS}\sqrt{E}}{KT}\right) \qquad 3\text{-}11$$

Where β_{RS} represents a constant, Φ_B denotes potential barrier height, and J_{RS} is the tunnelling current density. J_{RS} is weakly dependent on the *E*-field and strongly dependent on temperature. In contrast, the Fowler-Nordheim tunnelling equation 3-12 shows J_{FN} is largely dependent upon the *E*-field and not on temperature.

$$J_{FN} \propto \frac{E^2}{\phi_B} exp\left(-\frac{\gamma \phi_B^{\frac{3}{2}}}{E}\right) \qquad 3\text{-}12$$

Where the constant is denoted by γ.

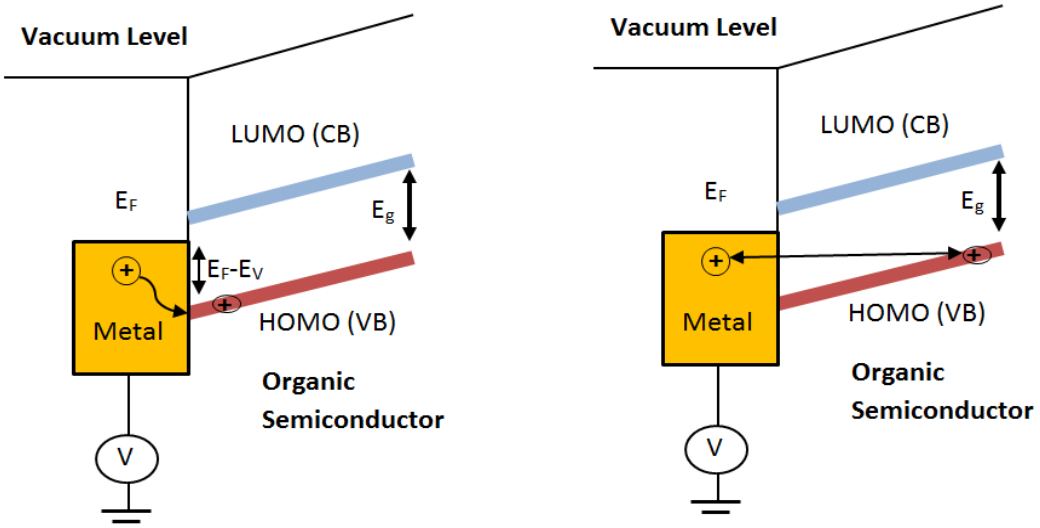

Figure 3.11 *The mechanisms of charge injection from metal into organic semiconductors applying bias: thermionic emission* ***(left)*** *and Fowler-Nordheim tunnelling* ***(right).***

3.2.2.4 Transport of charge carriers and mobility

The nature of charge carrier transport within OSCs is a widely discussed topic [129], with several competing models attempting to offer an accurate description of the experimental observations [107]. It is believed that a semiconductor's level of purity and crystallinity, as well as their chemical identity, are key factors in the resulting carrier mobility.

Formally, both J_{RS} and J_{FN} display a divergence to 'infinite' injected current density in the absence of injection barriers ($\Phi_B \rightarrow 0$); however, this is unphysical. In the absence of barriers, the current density flowing across a device is instead limited by charge transport across the OSC film rather than by injection. As carriers pass across the film, they represent a

space charge that, at the injecting electrode, exactly screens the externally applied field so that injection remains finite. Such a device is considered space charge limited ('space charge limited conduction, 'SCLC') or 'transport limited', rather than 'injection limited'. For a full discussion of SCLC, I refer to [131]. Here only one aspect of carrier transport in OSCs is discussed; namely, the carrier mobility, μ, as SCLC itself is not relevant in the thin film transistor devices that form the focus of this work.

Charge carrier mobility (symbol μ) is a key property of semiconductors. Carrier mobility is defined as a charge carrier's average drift velocity per unit of the electric field as in Eq. 3-13.

$$\langle v \rangle = \mu E \qquad 3\text{-}13$$

Where ‹*v*› denotes the average velocity of the carrier.

Eq. 3-13 is an oversimplification though, as in OSCs carrier mobility depends on E-field and charge carrier density [132]. Mobility is conventionally expressed in units of $cm^2\ V^{-1}s^{-1}$. In contrast to inorganic semiconductors, the carrier mobilities in OSCs are generally smaller by several orders than in inorganic semiconductors. To be specific, the mobilities of OSCs are in the range of $\sim 10^{-6}$ to$\sim 10^{2}$ $cm^2\ V^{-1}s^{-1}$, with significantly disordered amorphous materials appearing to possess lower mobility whereas the high mobility results from the high order of crystallinity [107]. Paterson *et al.* [133] present the recent progress of high-mobility in OFET as well as finding that the reliable hole mobility values of 20 $cm^2\ V^{-1}s^{-1}$ have yet to be achieved and the electron mobility does not reach this value of 10 $cm^2\ V^{-1}s^{-1}$.

The classical transport model for the inorganic semiconductor band is dependent upon the fact that there is an overlap in all constituent atom orbitals of the semiconductor. This forms a reliable band transport that supports charge carrier mobility. In addition, band transport is disturbed by temperature and according to that, the scales as $\mu \propto T^{-n}$(where n is negative), indicating that mobility is improved when the temperature is reduced.

For organic structures with good order (for instance, vacuum sublimed pentacene) there is a proposed model for explaining the temperature dependence of mobility which in some instances is seen. The model is known as multiple trapping and release [134] and asserts that

thermally activated removal of trapped carriers increases with the temperature that in turn increases mobility.

The model is based on the assumption that localised trap states exist close to the edge of the transport bands (LUMO for n-types and HOMO levels for p-types) and that trap states arrest any adjacent charge carrier with a probability of approximately 100%. The final premise is that the release of trapped carriers is thermally activated. Eq. (3-14) gives effective mobility as

$$\mu_{eff} = \mu_0 \alpha e^{-(E_c - E_t)/kT} \qquad 3\text{-}14$$

Where α denotes the ratio for trap density of states (DoS) to the density of states at the edge of the transport band, E_t represents the trap states' energy, E_c denotes the edge of the transport band, and μ_0 denotes the mobility in the absence of traps.

Amorphous or disordered structures of semiconductors have also been found to show thermally activated mobility: it is believed that transport of charge carriers within amorphous materials is by "hopping", wherein charge carriers are localised on a single molecule but can undergo thermally assisted tunnelling to another neighbouring molecule. In some instances, a description of hopping transport is achieved through an equation resembling the Poole-Frenkel (PF) equation [134], as shown in Eq. (3-15).

$$\mu_{eff} = \mu_0 e^{-(\Delta_0 - \beta\sqrt{E})/kT_{eff}} \qquad 3\text{-}15$$

Where $\mu_0 = \mu(T{=}T^*)$, Δ_o represents the energy barrier required, β donates the Poole-Frenkel factor and $T_{eff}^{-1} = T^{-1} - T^{*-1}$. This is consistent with experimental results reported by Redecker *et al.* [135] which are characterised by field dependence of mobility of ln (μ) $\propto E^{0.5}$. In the current model though, there is an issue that T_{eff} does not have a physical meaning.

The importance of charge carrier traps is evident when designing organic devices because high trap state levels can significantly alter the device's properties. Notably, traps refer to localised low states of energy which seem to occur in the band gap. They appear as carriers specific – that is, they are hole traps or electron traps. Electrons can be trapped from the

LUMO level (conduction band) and holes can be trapped from the *HOMO* level (valence band). Trapped carriers are immobilised (i.e. they no longer contribute to charge transport but still represent a space charge and reduce the strength of the E-field in the semiconductor). To free the trapped carriers, an activation energy is needed. Finally, materials can be classified according to the type of charge carrier that can be transported into p-type or hole transporters. These classifications refer to a material that oxidises to transport a positive charge [136] and n-type or electron transporters, which constitute a material that reduces to gain a negative charge [137].

3.2.2.5 Organic semiconductor materials

According to the discussion at the end of section 3.2.2.1, a notable difference between the OSC categories pertains to the manner in which they are processed to create thin films. While small molecules are often deposited from the vapour phase through evaporation or sublimation, conjugated polymers can be processed from solutions (e.g. by printing [138] or spin-coating methods [84]). While some low-molecular weight materials can be prepared as single crystals, polymer OSCs are fully amorphous or semi-crystalline, with the degree of crystallinity depending on molecular architecture and processing conditions; in particular the processing solvent. The two most important OSCs used in this thesis are discussed: both polymers based on the thiophene ring, as described in section 3.2.2.2.

3.2.2.5.1 Poly (3-hexylthiophene-2,5-diyl) or P3HT

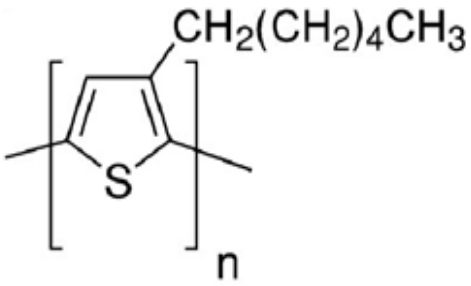

Figure 3.12 *Chemical structure of regioregular poly (3-hexylthiophene-2, 5-diyl) rrP3HT.*

P3HT is one of the most widely studied organic semiconductors in many fields of organic electronics in diverse applications [84, 139, 140]. P3HT refers to a conjugated polymer consisting of a polythiophene-backbone with lateral hexyl side chains, as illustrated in Figure 3.12. Alkyl side-chains help the P3HT to dissolve easily within organic solvents, allowing solution processing. Three sequencing formats exist for alkyl chain position on thiophene rings: tail-tail (TT), head-head (HH), or head-tail (HT). The TT and HH couplings trigger twisting within the rings of thiophene and increase the torsional angle. Subsequently, this disrupts the π-conjugation. It also hinders crystallisation, thus producing larger band gaps and reduced mobility. Polymers containing TT and HH couplings are termed regiorandom, not regular. To achieve the preferred sequencing format HT along the backbone entirely to give what is known as regioregular P3HT ('rrP3HT')(>95% head-to-tail regioregular), polymerisation has to be conducted along a particular route first shown by McCullough *et al.* [141]. Sirringhaus *et al.* [142] reported the highest hole mobility of rrP3HT at approximately 0.1 cm^2 V^{-1} s^{-1} when rr-P3HT adopts an edge-on backbone orientation relative to the substrate. Hence, the orientation relative to the substrate by polymer backbone is a key aspect that determines the electrical performance [142]. Moreover, rrP3HT is dissolved in 1,2-dichlorobenzene (DCB) [84] or toluene [15] or may be another organic solvent (more details reported in section 4.3.1.1). The limitation of P3HT lies in its sensitivity towards oxidation.

3.2.2.5.2 Poly (2,5-bis(3-hexadecylthiophen-2-yl) thieno[3,2-b]thiophene) PBTTT

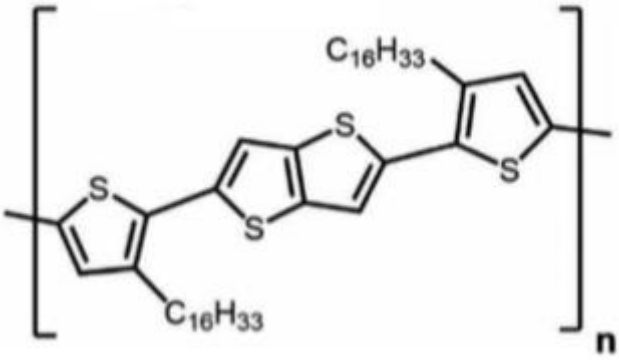

Figure 3. 13 *The chemical structure of poly (2,5-bis(3-hexadecylthiophen-2-yl) thieno[3,2-b]thiophene) or PBTTT-C16.*

Poly(2,5-bis(3- hexadecylthiophen-2-yl)- thieno[3,2- *b*]-thiophene) (PBTTT) [143] is another extensively investigated and successful polythiophene derivative. The structure of PBTTT is shown in Figure (3.13). PBTTT is comprised of TT-alkylated bithiophene moieties co-polymerized alongside a thieno[3,2- *b*]thiophene unit which, aside from strengthening the backbone and increasing the ionisation potential (I_P), serves as the spacer between solubilising alkyl chains, enabling interdigitation of the side chains [144]. Due to its more planar and rigid backbone than in P3HT, PBTTT displays a liquid crystalline phase at 180^{o}C on a hot plate after casting a film [143]. In addition, annealing within the LC phase has been found to improve charge carrier mobilities from 0.1 -1 cm ^{2} V $^{-1}$ s $^{-1}$ [145]. In summary, PBTTT displays better mobility than P3HT and is more stable against oxidation due to its lower I_P, but it displays rather poor solubility. It should be noted that PBTTT-C16 was dissolved in 1,2-dichlorobenzene (DCB) and due to its rigid backbone formation, it is necessary for the DCB to be dissolved at high temperature, and for it to be stirred using a magnetic stirrer intensely (more details reported in section 4.3.1.1).

3.3 Organic electrochemical transistor (OECT) vs electrolyte-gated (EGOFET) behaviour

Electrolyte-gated organic field effect transistors (EGOFETs) can, in principle, operate in two modes: an organic field effect transistor (OFET) mode, or an organic electrochemical transistor (OECT) mode, as shown in Figure 3.14 [146, 147]. In the OFET mode, a gate voltage applied across the electrolyte leads to interfacial electric double layers (EDLs) at the

gate/electrolyte interface and the electrolyte/semiconductor interface. The latter consists of an excess of one type of ion in the water and an opposing charge carrier accumulation layer at the semiconductor's surface. In principle, this can be anions *vs* holes or cations *vs* electrons. However, practical EG OFETs are usually hole transporting. A negative gate voltage, when exceeding a transistor-specific threshold, will generate hole accumulation and conductivity in the transistor channel: EG OFETs work in accumulation mode. Transconductance is proportional to the EDL capacitance, C_i, ($\approx$ 3 $\mu F/cm^2$ for water gating[33]) but is independent of semiconductor film thickness, d. In contrast, in OECT mode, the gate voltage does not lead to an interfacial EDL but drives ions across the electrolyte/semiconductor interface into the bulk of the semiconductor. OECT mode operation is further divided into 'depletion mode' and 'accumulation mode'. In accumulation mode, ions dope a previously undoped semiconductor channel; in the depletion mode, ions de-dope a previously doped channel [148, 149]. As we now have bulk rather than interfacial transport, transconductance is proportional to dC*, where C* is a capacitance per unit volume, and d the thickness of the semiconductor film. A 130 nm film of the synthetic metal PEDOT: PSS displays dC* $\approx$ 500 $\mu F/cm^2$ [150], two orders of magnitude larger than C_i in field effect mode, leading to correspondingly larger 'on' currents. This also gives a simple experimental criterion to distinguish OFET from OECT operation, namely that OFET current is smaller and independent of semiconductor film thickness, d, while OECT current is larger, and increases with d. More details regarding electrochemical gating with aqueous media are reported in chapter 8.

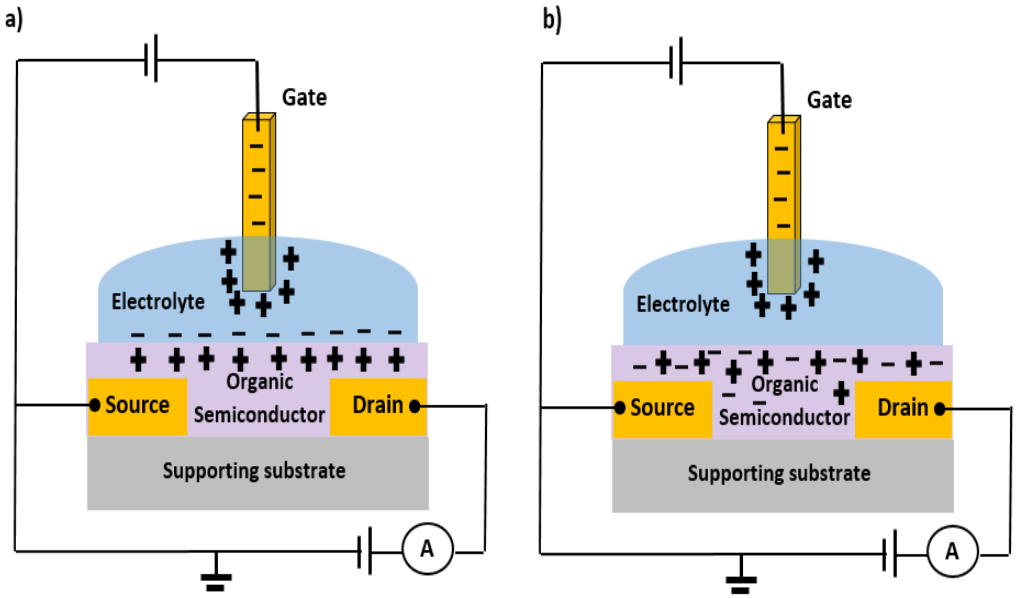

Figure 3.14 *Diagram illustrating the modes of OFET when applying a gate voltage; (a) Electrolyte-gated OFET and (b) OECT.*

3.4 Quantitative concepts of ion sensing

The basic principles of potentiometric ion sensors have been presented earlier in section 2.4. In fact, validating a method of analysis constitutes an important step in the assessment of its ability to offer accurate quantitative data. This is applicable to a novel technology that incorporates electronic detection [47]. The analytical figures which should be evaluated in this case include quantification, sensitivity, selectivity, limit of detection, Nernst vs Nikolsky Eisenman principles, and membrane potential [47]. Even though there have been numerous attempts to globally standardise bio-analytical technique validation guidelines, it is still necessary to explain the interpretation and meaning of important features of detecting assay credibility [47]. The quantitative concepts are presented below.

3.4.1 Membrane potential (E_m)

In section 2.4 the ionophore and ion selective membrane (ISM) and how they can be combined were introduced. Briefly, ISMs build up a membrane potential depending on the identity and concentrations of ions in the adjacent aqueous media, which can then be transduced into a voltage reading with different transducer concepts.

List-Kratochvil *et al.* [15] presented the possibility of combining a WGTFT as a transducer with an ISM (discussed earlier in section 2.4) as an active sensing component able to select and reverse detection of specific ions. Typically, ISMs are plasticised PVC membranes

containing ionophores as cation-selective sensitisers (discussed in section 2.4 and shown in Figure 2.9 (c)). The ISMs comprise an ionophore, ion exchanger, plasticiser and polyvinyl chloride (PVC). If ISMs are placed between two chambers: one chamber contains a reference solution of known ion concentration; the other contains the sample solution with unknown analyte ion concentration. The rrP3HT transistor was in contact with a reference solution held in an 'internal' chamber that is separated by the sensitised PVC membrane from a second, 'external' chamber. The external chamber is initially also filled with the reference solution, but this is then subsequently replaced with different ion concentrations, while the internal chamber remains filled with the reference solution. The ISM builds up a membrane potential that is related to the difference in analyte ion concentrations between the two chambers. The membrane potential is associated with the external and internal solution ionic activities and approximated by the Nernst equation [15]:

$$E_m = \Delta V = 2.3\frac{RT}{zF}\, log\left(\frac{a_{external}}{a_{internal}}\right) \qquad 3\text{-}16$$

Where E_m denotes the membrane potential – the potential difference ΔV between the membrane's two interfaces – and 2.3 = ln 10. 2.3 (RT/zF) denotes the Nernst slope (s) or calibration curve slope, a represents the corresponding activity of the targeted ions within the internal (reference) filling solution and the analyte (external), and z represents the valency of the detected ions (e.g. 1 for K^+ and 2 for Mg^{2+}).

In Eq. (3-16) Above, activity (a) refers to the effective concentration of ions in the presence of the electrolyte [151]. The concentration (c) can be related to the activity (a) via the activity coefficient (f) where $[a] = f\ (c)$. With dilute aqueous solutions, and in the lower concentrations, the activity coefficient is close to unity: $f = 1$ [151]. In this case the activity is approximately equal to the concentration. $\frac{a_{external}}{a_{internal}} \approx \frac{c_{external}}{c_{internal}}$

3.4.2 Sensitivity, selectivity and limit of detection (LoD)

According to the development of sensor technology, it is very important to ensure that a particular response (signal) emanates from the existence of targeted analytes within the sample being investigated. This section presents a description of three important sensor technology characteristics; namely, sensitivity, selectivity and limit of detection. Sensitivity

refers to the ability to discriminate small variations in test analyte mass or concentration and is equivalent to the calibration curve's slope; selectivity constitutes the analytical method's ability of discriminating the analytes from interfering parts such as other analytes [47].

Ionophores can interact with all ions, not just the intended target ion. However, interaction with one particular ion will be stronger than with any other, which allows a quantitative definition of selectivity. Quantification of selectivity is undertaken through selectivity coefficients $K_{M,N}$ where N represents the discriminated or interfering ion and M represents the primary or target ion. Interference results are simplified based on Eq. (3-17).

The $K_{M,N}$ parameter is defined as the selectivity coefficients and can be expressed as:

$$K_{M,N} = \frac{a_M}{(a_N)^{z_M/z_N}} \qquad 3\text{-}17$$

When the parameter $K_{M,N}$= 1, this implies that the membrane reacts to N and M ions. In the case ($K_{M,N}$ <1), it is implied that the membrane has a higher reactivity to the analyte ions against interfering ions. From a commercial point of view, the manufacturer supplies the selectivity coefficient value; nevertheless, the value can be measured experimentally through constantly adding interfering ion concentrations to a diverse analyte concentration. The $K_{M,N}$ can be located using a calibration curve, as illustrated in Figure 3.15.

When membrane potentials resulting from interfering as well as target ions are included into the Nernst equation, we get the Nikolsky-Eisenman equation (NEQ) [152]:

$$\Delta V = \frac{0.0592\,V}{z}\, log[a_M + a_{st}\,] \qquad 3\text{-}18$$

Where

$$a_{st} = K_{M,N}\,(a_N)^{\frac{z_M}{z_N}} \qquad 3\text{-}19$$

a_{st} denotes the respective ion-sensitive system's constant property and is approximately equivalent to the *LoD* concentration. This is due to the presence of interferents which serve as the constant of *LoD* observed.

The Nikolsky-Eisenman response approaches the Nernstian response at high activity (concentrations) $a_M >> a_{st}$, but flatlines for $a_M << a_{st}$ while the Nernst law predicts an unrealistic divergence of E_m in the limit of $a_M \rightarrow 0$. a_{st} therefore represents a limit-of-detection for a_M. Note that in the aqueous medium, the concentration of interfering ions can never approach zero, not even for high quality deionised water due to autoprotolysis. Practically, for membranes sensitised with organic macrocycles as ionophores, we find $a_{st} = c_{st}$ = LoD in the order (100 nM … 1 µM)[15, 17], in certainly, rarely below 100 nM [18].

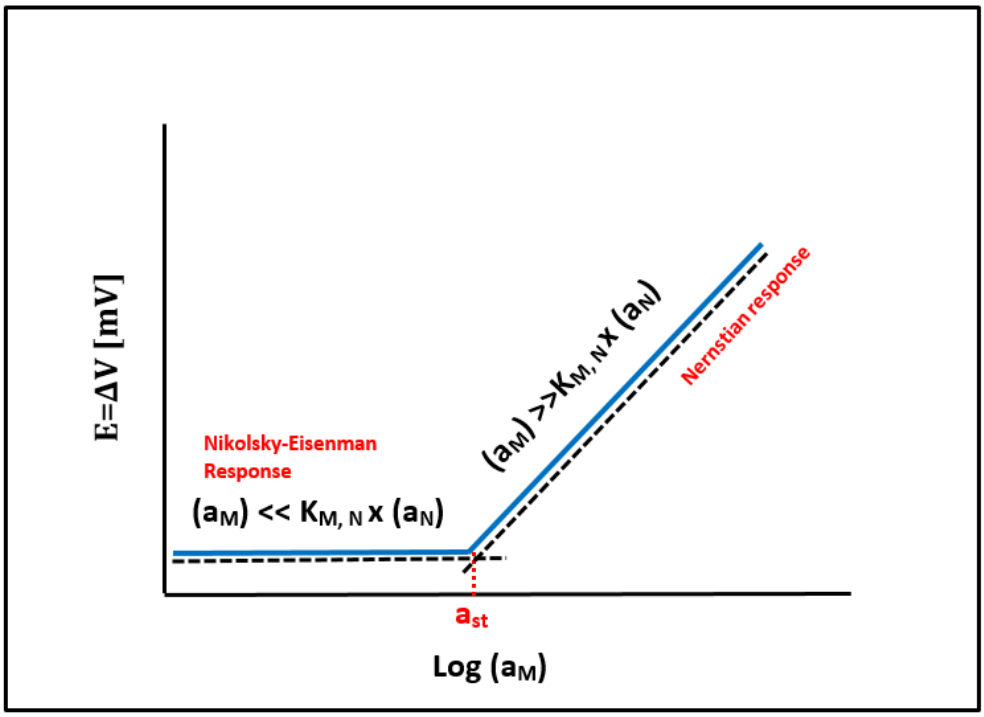

Figure 3.15 *Diagram showing the relationship between the membrane potential and logarithmic of ion activity with the Nernstian and Nikolsky-Eisenman responses where a_{st} is the limit of detection.*

Eq. (3-18) can be written in this form:

$$\Delta V = \frac{0.0592\,V}{z}\, log\left[a_M + K_{M,N}\,(a_N)^{\frac{z_M}{z_N}}\right] \qquad 3\text{-}20$$

Where the parameter a_N represents the activity of the interfering ion in the sample solution, a_M represents the activity of the target ions in the sample solution, and z_N and z_M represent the interfering and primary ion charges, respectively. The Nikolsky-Eisenman law is illustrated schematically in Figure 3.15.

If the activity of the analyte surpasses that for $K_{M,N}\times$ (a_N), the potential of the membrane constitutes the log (a_M), linear function, as Eq.(3-17) denotes. However, if the activity of the analyte is considerably smaller than that for $K_{M,N} \times$ (a_N), the potential of the membrane remains unchanged. The $K_{M,N}$ value can be calculated from two intersecting linear regimes of the interferent and analyte's activity.

Chapter 4: *Fabrication of water-gated transistor substrate*

The construction of a WGTFT is split into two steps; the first step is the forming of a transistor substrate - a pair of opposing contacts, source and drain, on a supporting substrate connected by a semiconducting film. The second step is applying a drop of water as electrolytic gate medium and contacting it with a third contact, the gate (Figure 4.1 (d) described later in section 5.2). Within this current chapter, the manufacture of such transistor substrates shown in Figure 4.1 (a-c) will be described. In section 4.1, the cleaning and preparation of a solid supporting substrate are described. This is followed in section 4.2 by an explanation of the mode of depositing TFTs contacts, such as gold or chrome, using thermal evaporation to create contact substrates. In section 4.3, the method of depositing thin film semiconductors using spin coating and spray pyrolysis to create transistor substrates is explained. Finally, in section 4.4, the treatment of metal oxide by hexamethyldisilazane (HMDS) is explored.

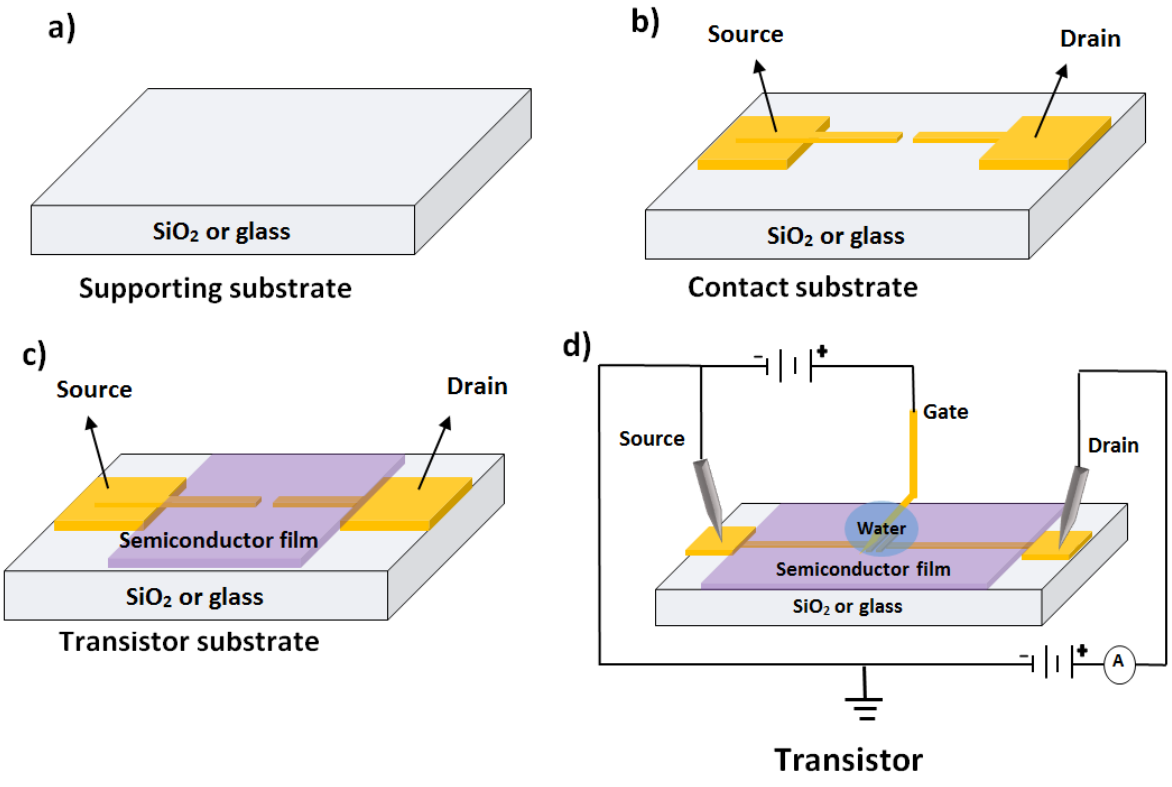

Figure 4.1 *Schematic diagram of the steps of building the transistor:* ***(a)*** *supporting substrate,* ***(b)*** *contact substrate,* ***(c)*** *transistor substrate, and* ***(d)*** *transistor.*

4.1 Supporting substrate

The type of supporting substrate used plays an essential role in the application of thin films and dictates its specific uses. In this current research, one type of supporting substrates was used. To prepare transistor substrates that could then be transformed into WGTFTs through the application of a gate medium and the gate contact, 20 mm x 15 mm flat glass slides coated with 20 nm of SiO_2 sourced from Ossila Ltd. were used.

4.1 .1 Supporting substrate cleaning

Cleaning the slides or supporting substrates is essential to obtain high quality fabricated devices as it allows good adhesion of later deposits. It is important that the supporting substrates are cleaned prior to any additional processing.

Organic residues found on supporting substrates were eliminated through the use of various organic solvents via sonication in various stages. Each subsequent step of the procedure was conducted in a clean environment (cleanroom) under room temperature conditions using clean gloves and tweezers. Initially, cleaning of all slides or supporting substrates was performed using acetone with a lab-wipe, followed by drying with dry nitrogen. Acetone acts as a de-greasing agent, removing fatty residues. Subsequently, the supporting substrates were stored in a Teflon holder with suitable dimensions to guarantee that each side of the supporting substrates could be cleaned easily. Then, the supporting substrates were submerged in a clean glass dish that had been filled with 1:100 (v/v) diluted alkaline cleaning solution. Following this, they were deposited in an ultrasonic bath for a period of 5 minutes at 55 ^{o}C. Once this step had been completed, the supporting substrates were extracted from the alkaline solution and washed carefully using DI water. They were then dried with dry nitrogen. In the next stage of the process, the dried slides were once again placed in the Teflon holder, then submerged in a clean Petri dish filled with alcohol (isopropanol, IPA) and deposited in an ultrasonic bath at 55 ^{o}C. After this, the supporting substrates were extracted from the isopropyl alcohol and dried with dry nitrogen. Finally, each of the supporting substrates was stored in a small clean box.

4.1.2 Ultraviolet (UV) ozone cleaning

After the cleaning process detailed in Section 4.1.1 had been completed, any residual organic substances remaining on the surface of the supporting substrates were cleaned using Ultraviolet (UV) ozone treatment, as shown in Figure 4.2. Ozone is a powerful oxidising agent [153, 154] that has the capability of decomposing any organic matter that remains on

the surface of the slides or supporting substrate. In this final stage of the process, a clean Petri dish that held the slides was placed for 4.5 minutes into the chamber of an instrument that was illuminated by intense UV light of 184.9 nm through which ozone was produced from atmospheric oxygen. Note that the oxygen is absorbed to create ozone when UV rays are at 184.9 nm wavelength and vice versa when the UV rays are at 253.7 nm wavelength.

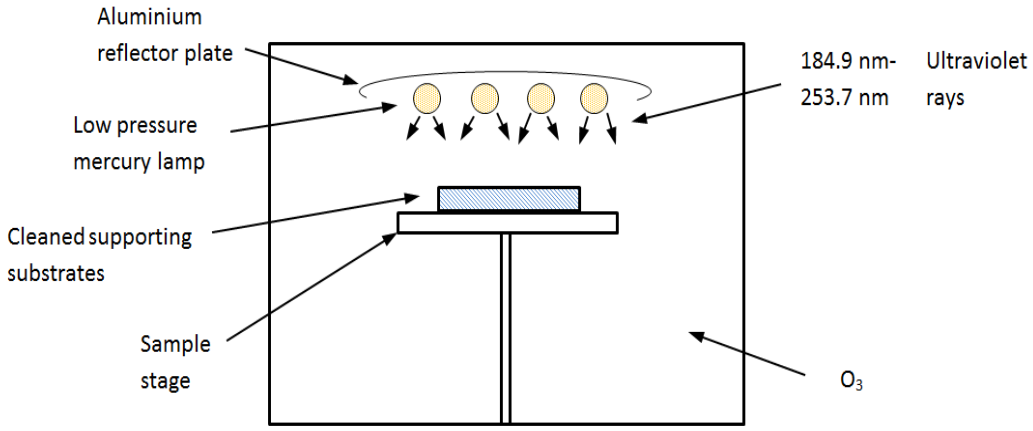

Figure 4.2 *Schematic diagram of the Ultraviolet-irradiated cleaned surface.*

4.2 Deposition of TFT contacts

After cleaning the slides to be used as supporting substrates, the next step in the preparation of transistor substrates was the deposition of a pair of metal contacts that would later serve as the transistor's source and drain contacts. We deposited metal contacts by thermal evaporation – also known as physical vapour deposition (PVD) – using a shadow mask. Fundamentally, thermal evaporation involves the transition of materials in a solid condition to a vapour condition by heating them within a high vacuum. The high vacuum is a particularly important factor in this process, as it prevents oxidation, collisions or reactions that may occur during the process [155].

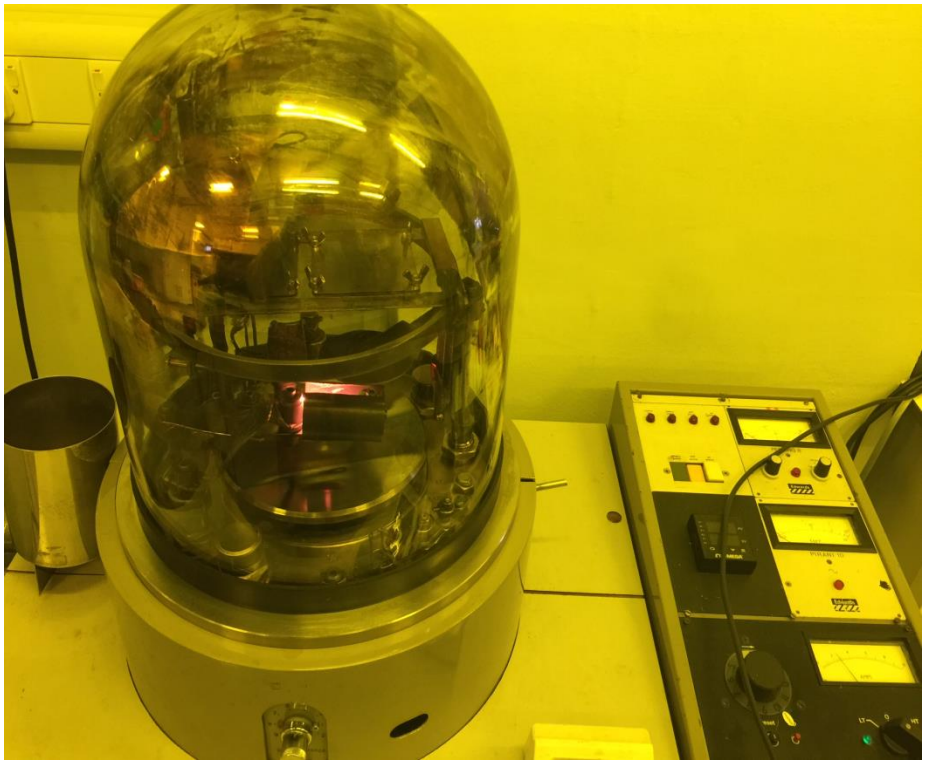

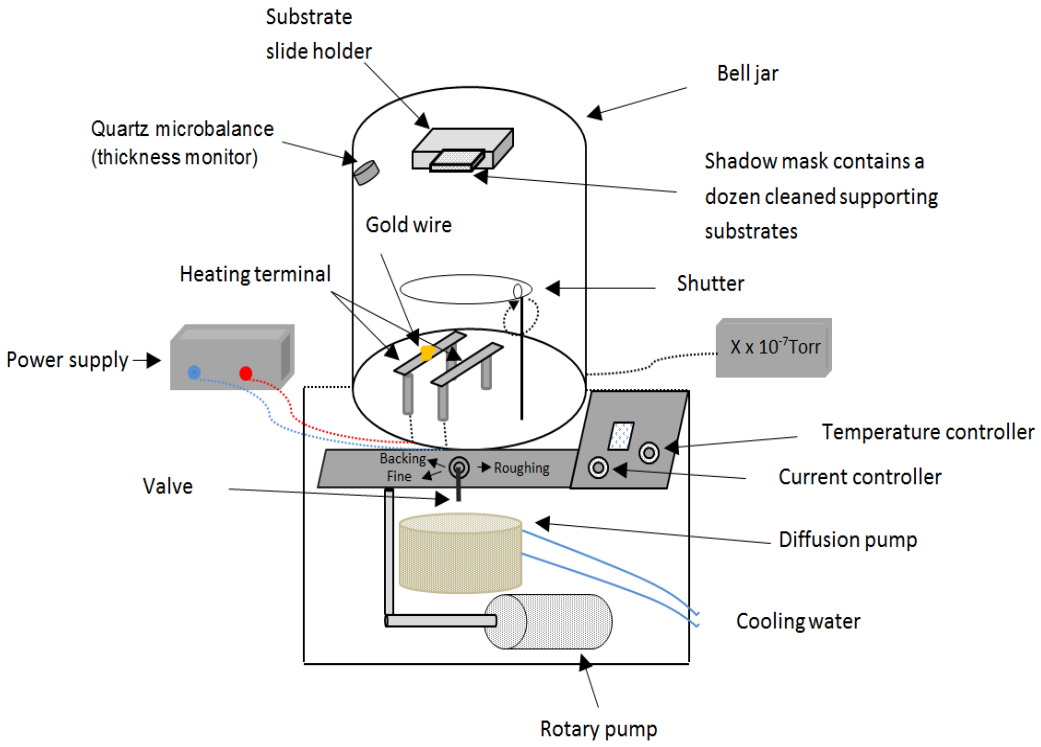

Figure 4.3 *Photograph of the thermal evaporator (Edwards E306) (top) and schematic diagram of the thermal evaporator with all components labelled (bottom).*

As shown in Figure 4.3 (bottom), the Edwards (E306) thermal evaporator was constructed of a glass bell jar with 305 mm diameter and 356 mm height. A shadow mask stack was used which contained a dozen cleaned SiO_2- coated slides/supporting substrates (as shown in Figure 4.4) and was carried in a substrate slide holder. A shutter disc was located between the heating terminal and the target surface which could be utilised as protection for the target surface from leftover volatile contaminants that were in the source material. The quartz crystal microbalance (QCM) was positioned equidistant to the evaporation source and was used to read the electronics residing outside the chamber of the evaporator. This could be used as a monitor to supply data on the thickness of the deposited films. Other feeds and electrical components such as the rotary pump, gauges, diffusion pump, vacuum and pipe of cooling water were placed at the metal bottom of the dome and are described below.

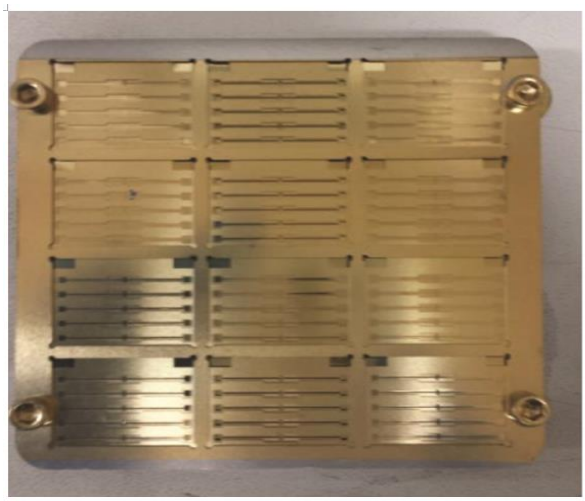

Figure 4.4 *Photograph of a shadow mask stack containing a dozen cleaned SiO_2- coated slides.*

The pumping system contained a fine pumping and a rotary pump. The first was achieved via water, and liquid nitrogen (LN_2) cooled diffusion pump: the second acted a rough pumping system. In each case, the pumping sequence could be controlled manually. In the initial stage, the dome was roughly pumped to a pressure of 1.3332 Pascal. After that, the diffusion pump took over and immediately reduced the pressure to 1.3332×10^{-3} Pascal. It should be noted that when pumping is prolongued and aided by continuous liquid nitrogen cooling, pressure can be reduced to 1.3332×10^{-5} Pascal.

The pumping system had two gauge pressures: one of them was used to measure the pressure in the vacuum chamber and the other to measure the backing pressure in the backing/roughing pipeline.

The evaporator contained two sources which allowed evaporation of different metals (e.g. Au, Cr) subsequently without breaking the vacuum. As evaporation sources, a tungsten boat with a short wire of pure gold placed in it and tungsten coils that were coated with Cr or Ti were used. This is because tungsten (W) has a very high melting point, which allows the melting of almost all other metals in a W boat. The tungsten boat and coated coil were connected to a DC current source which led to the Joule heating of the boat and coil and the respective metal. The current values of the materials used in our work for the thermal evaporation in the range from 1 Å to 2.2 Å.

The following procedure was used to prepare a pair of contacts on supporting substrates that were previously cleaned (as described in 4.1). The supporting substrates were positioned on steel frames such that the face coated in SiO_2 would later face the evaporation source. Subsequently, a thin shadow mask (obtained from Ossila) composed of five contact pairs for each substrate was positioned in front of the face of the supporting substrates coated in SiO_2, Following this, the supporting substrates were arranged by shadow masks and then positioned on a pair of parallel steel pieces placed opposite the heating terminals. In order to ensure that the shadow masks remained stable throughout the process of evaporation, a magnet was placed to their rear. A short wire consisting of pure gold (Au) (approximately 4 cm of length) was located at the centre of a small-sized tungsten boat which had previously been connected to terminal B on the evaporator's current source, as shown in Figure. 3.3 (bottom). As gold does not adhere to glass surfaces with sufficient strength, it was necessary to use terminal A of the evaporator device to connect the chromium (Cr) metal. Note that Cr acts as an adhesion layer for gold on SiO_2 and various oxide glasses. After the bell jar was closed, evacuation of the vacuum system was achieved through the two-stage pumping process described above which enabled the pressure inside the jar to be lowered to 1.3332×10^{-5} Pascal. The DC current for Joule heating of evaporation boats was ramped up manually, and the resulting rate of Cr or Au deposition was monitored with the QCM. Heater current was adjusted, and during this adjustment stage, the evaporator shutter was closed, shielding slides from metal evaporation. Once a steady deposition rate was adjusted, the shutter was pulled away, thus allowing Cr or Au vapours to deposit on the shadow-mask covered slides at a constant rate of evaporation. The quartz crystal microbalance (QCM) monitored the thickness of the deposited film on a continuous basis. Once the desired film thickness had been acquired, the shutter was closed again, and the heater current was stopped. After Cr adhesion layer deposition a similar process was repeated for Au. The rate used to deposit a 10 nm thin

adhesion layer of chromium on the supporting substrate was 0.2 Å/s and the rate used to deposit 100 to 120 nm thin film layer of Au on the same supporting substrate was 1 Å/s.

At a pressure of 1.3332 x 10^{-4} Pa, a free path length λ of metal vapours can be calculated using Eq. 4-1.

$$\lambda = \frac{k_B T}{\pi p d^2 \sqrt{2}} \qquad 4-1$$

Where p represents the vapour pressure, λ denotes the mean free path of molecules/atoms, d represents the diameter of the atoms/molecules, k_B is the Boltzmann constant and T is defined as the absolute temperature. According to Eq 4-1, λ = 44 m assuming a typical metal atom has a diameter d = 0.4 nm. This is far longer than the distance between the supporting substrates and the hot source in our equipment, which was only ≈15 cm. As a result, the vacuum achieved in our evaporator was good enough for physical vapour deposition (PVD).

The thermal evaporator was designed to electrically sustain the resonant mechanical oscillations of the quartz crystal and measure their frequency via the electromechanical coupling afforded by the piezo effect. The resonant frequency shifts as a result of the mass deposited on the surface of the quartz crystal according to the Sauerbrey equation [156].

$$\frac{\Delta f}{\Delta m} = \left(-\frac{2 f_0^2}{A\sqrt{p_q \mu_q}}\right) \qquad 4-2$$

Where Δf represents the frequency alterations, f_0 denotes the resonant frequency, p_q is the quartz density (= 2.648 g/cm^3), μ_q is the shear modulus of the quartz (=2.947x10^{11} g·cm^{-1}·s^{-2}), A denotes the area of the quartz crystal that is exposed, and Δm represents the change in mass.

Different factors can influence the ultimate quality of the film deposited on the supporting substrate, including the rate of evaporation, the substrate temperature, the position of the substrate relative to the source of evaporation, any impurities on the substrates, and the existence of any ambient gas within the evaporator equipment prior to the vacuum being established.

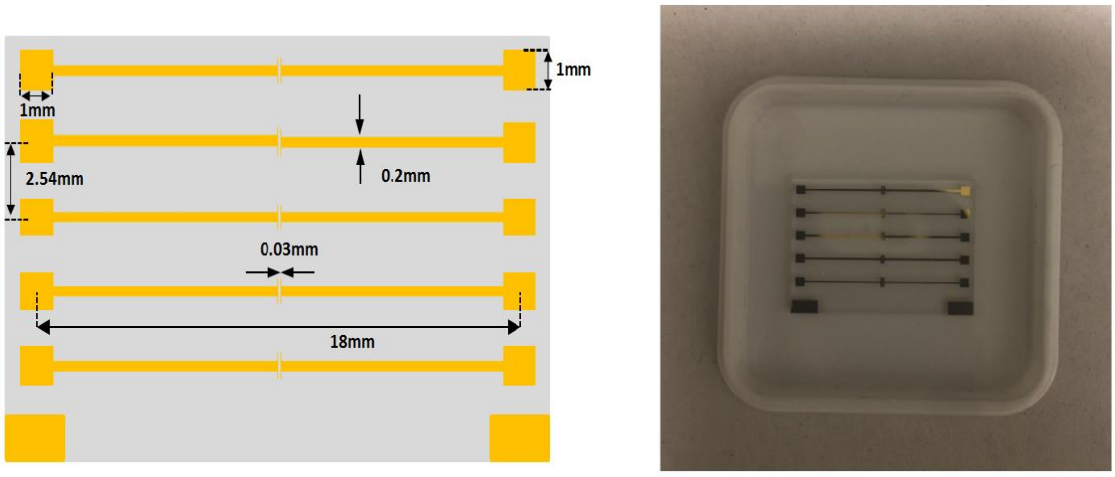

Figure 4.5 *Contact substrate geometry (left) and supporting substrate after deposition of chromium and gold contacts (right) creating a contact substrate.*

Figure 4.5 shows the contact substrate with five Au electrode pairs of width W= 1mm separated by a channel of length L=0.03 mm; W/L = 33.3. Au electrodes with a Cr adhesion layer were evaporated onto supporting substrates through a shadow mask as described above.

Following this stage, the contact substrates were then ready to deposit thin film semiconductors onto them to create transistor substrates. This process is described in the next section.

4.3 Deposition techniques for thin film semiconductors

Having explained the technique used to create a contact substrate, this section describes the process that leads to the production of a transistor substrate by applying a semiconducting film that connects the contact pair of the contact substrate. In this research, two types of solution-processed semiconductors were used; namely, organic semiconductor polymers and precursor route oxides. The processing routes used were different for each: spin coating technique and spray pyrolysis technique, respectively. These are explained in the following sub-sections.

4.3.1 Spin coating technique

One of the most frequently used deposition techniques for soluble materials is a spin coating (also known as spin casting). In this process, optimal outcomes can be accomplished when the solute is a polymer such as the organic semiconductor polythiophene. Through spin

coating, films with consistent thickness across large areas can be acquired without the use of evaporators. This technique is distinguished by its simplicity, ease of use, and the reproducibility of the procedure for batch production.

As shown in Figure 4.6, spin coating devices are generally constructed using *Polytetrafluoroethylene*, also known as Teflon, which exhibits increased resistance to all chemicals and can be easily cleaned. Normally, spin coaters are covered with a clear lid with a small aperture in the centre, which enables the user to insert a few droplets of solution onto the substrate. These are secured on a turntable by a vacuum created within the coater. Dry nitrogen is consistently utilised inside the spinning chamber as this reduces moisture or ambient oxygen during the spin coating procedure.

Figure 4.6 *Spin-coater used in our laboratory (WS-400BZ-6NPP/LITE Model).*

Spin coating involves spinning a solution on a substrate while it dries using centrifugal force to achieve an even spread of a thin film of solution over the entire substrate. Figure 4.7 shows the four basic steps of the spin coating technique: deposition, acceleration, flow domination and evaporation. These four steps are described through two different types of deposition.

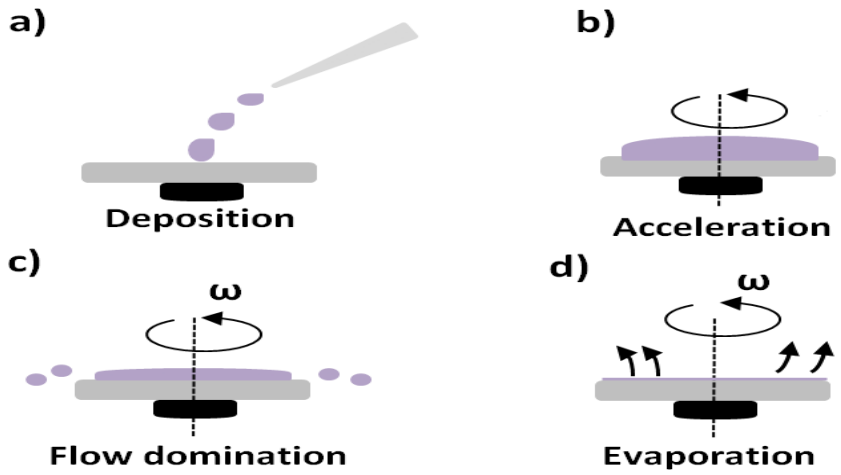

Figure 4.7 *The basic steps in the spin coating technique: (a) deposition, (b) spinning or acceleration, (c) flow domination or spread out and (d) evaporation.*

The first is called dynamic deposition, in which a few drops of the solution are inserted through the aperture and then applied on the substrate whilst the spinning process is ongoing. The second is static deposition, which was used in this present work, and can be described as a few drops of the solution being inserted through the aperture in the lid onto the substrate prior to the commencement of the spinning process.

Essentially, the spin coating method used for this research can be explained according to these generic steps. Firstly, drops of solution (approximately 35 µL from the solution by a Pasteur pipette) are applied to the surface of the contact substrate (reported in section 4.2), which is secured to the table as a result of the vacuum generated within the spin coater. Subsequently, angular velocity ω is ramped up with an angular acceleration α until it reaches a pre-selected value. ω is then held constant for a time T. The units for α and ω typically used are not SI units: the SI unit for α is radians/second squared (rad/s^2) and for ω is (rad/s), but revolutions per minute (rpm) is usually used for α, ω.

This technique employs a centrifugal force, whereby the solution is distributed across the contact substrate due to the balance of forces causing the solution to impulse off the surface and subsequently to stick to it. Throughout the rapid spinning procedure, drying of the wet thin film produced occurs as a result of the evaporation of the solvent, with the final result being a film of uniform thickness.

Equation (4-3) is used empirically to link the effect of solution parameters to find the film thickness:

$$t \propto \frac{c\,\eta(c)}{\sqrt{\omega}} \qquad 4\text{–}3$$

Where c denotes the solution concentration, η(c) represents the solution's viscosity, ω is the angular velocity of spinning, and *t* is the thickness of deposit film.

It is a widely acknowledged fact that both the quality and the morphology of the deposited films are strongly correlated to the specific solvent utilised [157]. For example, for the transistor, high crystallinity is desired for good mobility, and a solvent of low volatility should thus be used to allow more time for crystallisation during the spin process and are obstructive to the polymer chains in the process of ordering and crystallisation [157, 158]. We can conclude from the discussion above that a solvent must be used which has the right volatility (i.e. low for transistors) and has to wet the substrate well.

In this research, a spin coater was employed to create and deposit a thin film (TF) of organic semiconductors. As part of this thesis, two different organic semiconducting polymers were used; namely, regioregular poly (3-hexyl thiophene) (rrP3HT) (obtained from Sigma Aldrich) (Cat No 698989, average M_n 15,000-45,000), reported in section 3.2.2.5.1 and poly (2, 5-bis (3-hexadecylthiophen-2-yl) thieno [3, 2-b] thiophene) (PBTTT-C16 sourced from Ossila Ltd (Cat. No. M141 PBTTT-C16) (with an average molecular weight M_w = 61 309 g mol^{-1}), reported in section 3.2.2.5.2. To prepare a thin film of organic semiconducting using a spin coating technique, it must be noted that the type of organic solvent plays an important role to dissolve organic material efficiently.

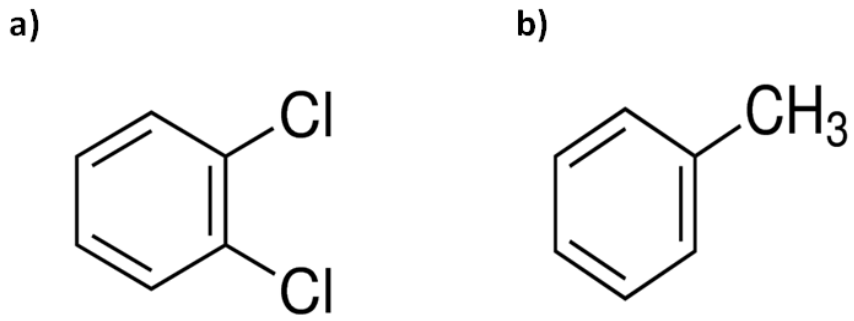

Figure 4.8 *The chemical formula of two organic solvents: (a) 1, 2-Dichlorobenzene and (b) Toluene*.

For rrP3HT two solvents were used: 1, 2-dichlorobenzene (DCB) and toluene as indicated in Figure 4.8. Both of these solvents provided a good film [15, 84]. For rrP3HT solutions in DCB, 10 mg of rrP3HT material was added through a dark vial which dissolved in 1mL of 1, 2-dichlorobenzene (DCB). Due to the fact that chlorinated solvents were being used, and also to prevent any chemical reactions occurring between the solvent and solute, it was necessary

to prepare the organic semiconducting polymers employed under reduced light conditions with solution vials made of either dark or brown glass. The dark vial was positioned on a hot plate at a temperature of 65 ^{o}C and continuously stirred for a period of 15 minutes using a magnetic stirring device. For rrP3HT solutions in toluene, 4 mg of rrP3HT material was added through a dark vial which was then dissolved in 1mL of toluene. The dark vial was positioned on a hot plate at a temperature of 75-80 ^{o}C and continuously stirred for a period of 15 minutes using a magnetic stirring device. Subsequently, a 0.45 μm polytetrafluoroethylene (PTFE) syringe filter was used to filter the rrP3HT solutions prior to spin coating.

To spin-cast films from such solutions, a Pasteur pipette was used to drop approximately 35 μL of solution onto a contact substrate that had been prepared previously (as described in section 4.2). Then, the contact substrate was spun for 60 seconds at 2000 rpm. After this, the films were dried completely in a dynamic vacuum at a temperature of 110 ^{o}C for 40 minutes for DCB and 120 ^{o}C for 60 minutes for toluene. The film thickness was determined with a Veeco Dektak XT surface contact profilometer (later described in section 5.1.2) as 22 nm for DCB and 15 nm for toluene.

PBTTT (C16) is another organic semiconducting polymer which is related to polythiophene but displays fused thiophene rings (as reported in section 3.2.2.5.2). Its synthesis and high carrier mobility in organic TFTs has been reported by McCulloch et al. [143]. 7 mg/ml of this polymer was dissolved by stirring it into hot DCB with a magnetic stirrer at 100 ^{o}C for a period of 10 minutes. As it can be challenging to dissolve PBTTT due to its rigid backbone formation, it is necessary for the DCB to be dissolved at high temperature, and for it to be stirred intensely using a magnetic stirrer. After this, a small amount of solution (approximately 35 μL) was dropped onto the TFT contact substrate using a Pasteur pipette to allow spin coating. The spin coating speed was fixed at 5000 rpm for 40 seconds. After casting was complete, drying of the films was performed in a drying vacuum at a temperature of 110 ^{o}C for 45 minutes. The eventual film thickness was 17.6 nm as an average (three films were prepared on supporting substrates then the thickness was measured for each substrare. The average was taken from these measurements).

4.3.2 Spray pyrolysis technique

Pyrolysis is the chemical conversion of a chemical educt, known as a ‘precursor’, into the desired product by heating it to a high temperature. Here, spray pyrolysis was used whereby the precursor was in a solution that was sprayed onto a hot surface using an airbrush.

Hence, although the process has similarities to chemical vapour deposition [159], it utilises a carrier solvent instead of a vacuum as the medium of deposition. A significant example of this is Zinc acetate (ZnAc), which converts into the inorganic II-VI semiconductor Zinc oxide (ZnO) at 450 ^{o}C [57]. Although ZnAc is a widely known chemical, its spray pyrolysis into ZnO was not reported until 2007 when Ong et al. [120] demonstrated TFTs with ZnO prepared from spray-pyrolysed ZnAc gated via a solid dielectric. A number of spray pyrolysis routes using metal chloride solutions as precursors have led to the creation of metal oxide semiconductors such as ZnO, SnO_2, TiO_2, IGZO or In_2O_3 [56, 120, 160-162]. These metal oxides lead to electron-transporting TFTs, while water-gated organic TFTs are usually hole-transporting [163].

Spray pyrolysis is a processing technique that has been utilised by researchers to generate films of different thicknesses as well as dense and porous films, ceramics and powders [164]. Additionally, this technique can facilitate the process of preparing films with multiple layers. Compared to other deposition techniques, these methods have various benefits, including more cost-effective processing due to the simple and inexpensive nature of the equipment used [164]. Further advantages are the capability to deposit over a larger area and the fact that different types of substrates that have complex geometries can be coated. In addition, it is not necessary to begin with substrates or chemicals of particularly high quality, and the resulting film are homogeneous with a consistent film thickness of between 0.1 – 1 μm [164, 165].

4.3.2.1 Spray pyrolysis deposition method of inorganic semiconducting solution

The basic functionality of spray pyrolysis is relatively simple and involves spraying a precursor solution - generating small droplets in the direction of a heated substrate - using an atomiser which creates the required spray. The only equipment necessary when performing this technique includes the precursor solution and a temperature control device. Different types of atomiser can be used in this technique such as compressed air atomisers, electric field atomisers and ultrasound atomisers [164]. In the present study, a compressed air atomiser was employed, also known as an airbrush, which sprays the precursor solution through a jet of air, as shown in Figure 4.9.

A number of parameters affect the spray deposition such as surface temperature, the atomisation process, the concentration of solutions, and the time between two drops striking the same surface [166].

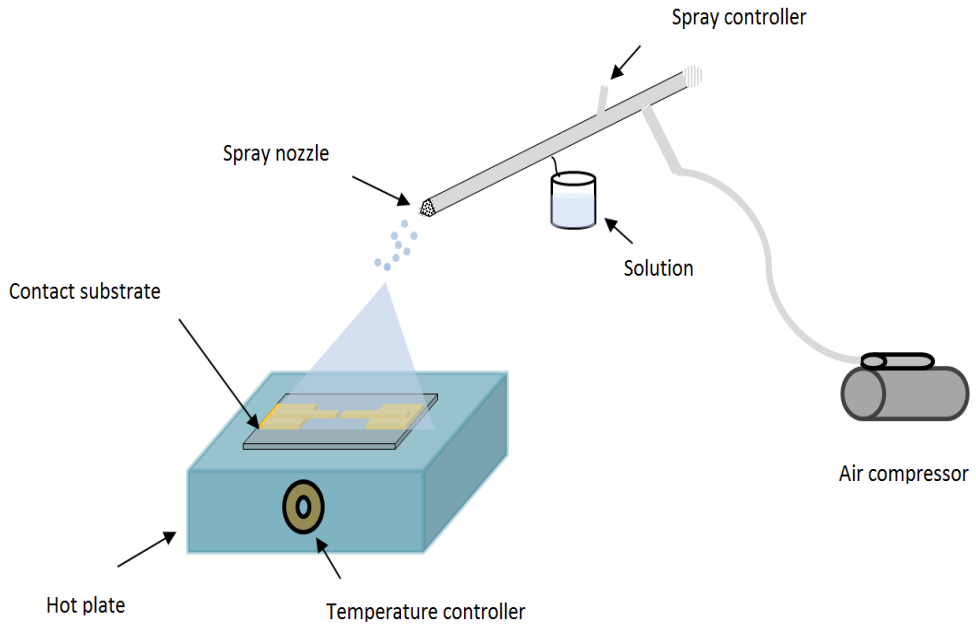

Figure 4.9 *Schematic diagram illustrating the spray pyrolysis technique when an airbrush is connected to an air compressor with a hot plate.*

Falcony et al. [167] reported a mechanism for spray pyrolysis which includes four different stages which occur when the droplet is exposed to different surface temperatures in two scenarios, as shown in Figure 4.10 (a and b). In the first scenario (a), the size of the droplet is constant, whereas the temperature of the substrate is varied and increases from A to D. In the second scenario (b), the size of the droplet is varied and increases from A to D, while the temperature of the substrate is fixed. Based on this, the mechanism can be described as follows: in process A, in which the substrate has a very low temperature and the size of the droplet is initially large, a small portion of the droplet with the solvent is vaporised as it reaches the surface. When the droplet strikes the surface of the substrate, the dry precipitate of a ring forms on the substrate. In process B, in which the substrate has a low temperature, and the size of droplet is smaller than the droplet in process A, the solvent is vaporised, and a dry precipitate strikes the surface of the substrate where a pyrolysis reaction is achieved. In process C, in which the substrate has a high temperature, and the size of droplet is smaller than in B, the droplet experiences the stages described in B sooner and then close to the surface of the substrate; the dry precipitate is vaporised, propitiating a chemical vapour reaction on the surface of the substrate. In the final process D, in which the substrate has a very high temperature, and the size of the droplet is smallest, within the vapour phase, the

vaporised precipitate is subjected to a chemical reaction and turned to the powder prior to reaching the surface of the substrate.

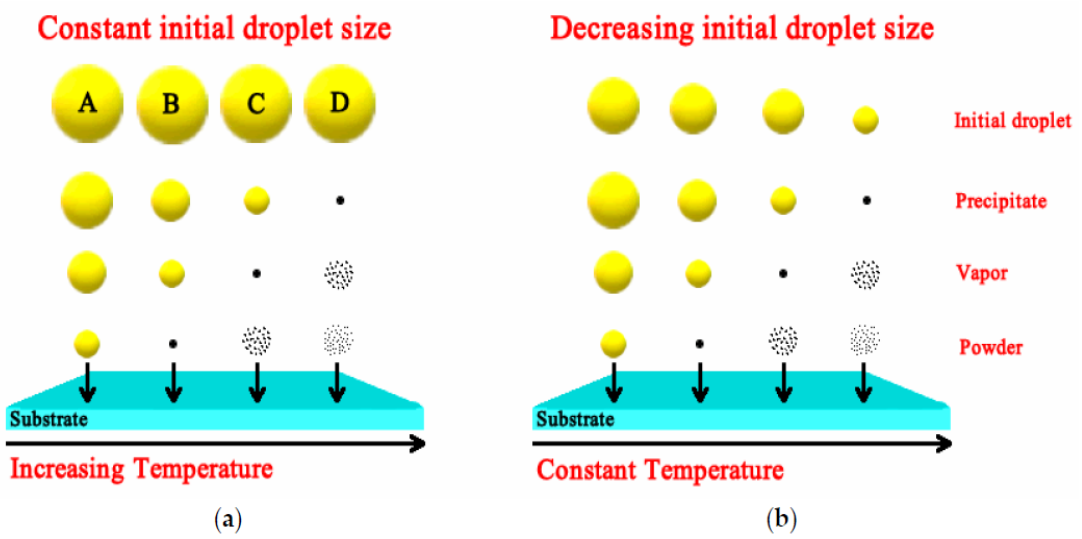

Figure 4.10 *Diagram of the mechanism of four different stages when the droplet is exposed to different surface temperatures for two scenarios: (a) changing substrate temperature, and (b) constant substrate temperature [167].*

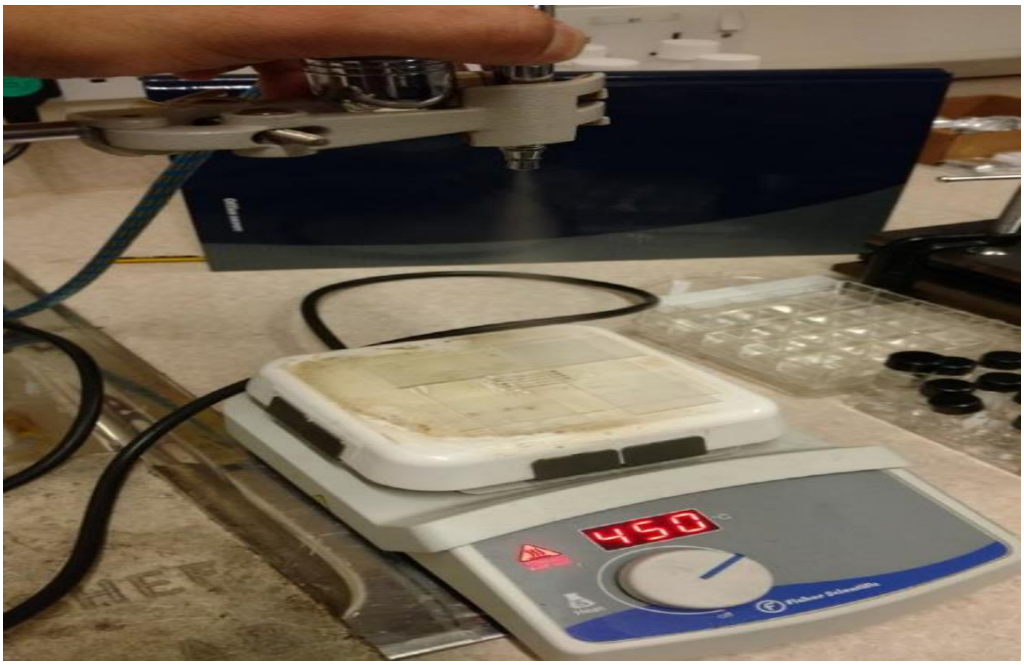

Figure 4.11 *Spraying $ZnCl_2$ precursor solution onto a contact substrate held at 450 ^oC on a hotplate.*

In this current work, chloride was used rather than acetate or nitrate precursor route to ZnO because it is known that the chloride precursor route leads to the highest degree of crystallinity in the resulting ZnO films, while ZnAc leads to largely amorphous films. This

has been studied systematically by Lehraki et al. [168]. In addition, Bacaksiz et al. [169] studied the effects of using chloride, acetate and nitrate precursor as a route to ZnO. They conclude that the mobility of zinc chloride precursor is the highest compared to zinc acetate and zinc nitrate precursor, which are 10.4, 8.6 and 5.1 $cm^2/V.s$ respectively.

A 100 mM solution of zinc chloride ($ZnCl_2$) was used as it is the optimum molarity used by most researchers in the field [168, 170]. This molarity leads to high crystallinity and high mobility [171]. 1.36 g of $ZnCl_2$ was added to 100 mL of DI water, wherein it is readily dissolved. This solution was then sprayed, using a pressure air atomiser at 1.5 bar pressure, onto a contact substrate (reported in section 4.2) that was held at temperatures ranging from 250 to 450 ^oC on a hotplate, as shown in Figure 4.11. For this purpose, a commercial GaGa Milano 134K airbrush with a 0.2 mm nozzle was used. The spraying technique consisted of 3 'puffs' from a distance of 15cm over the substrate at intervals of 20 seconds, with each lasting 1-2 seconds, as seen in Figure 4.11. The contact substrates then remained on the hot plate for an additional 30 minutes, which resulted in the production of semiconducting ZnO films [51, 168, 169].

4.4 Hexamethyldisilazane (HMDS) treatment

The surface of metal oxides (i.e. SiO_2, ZnO, and TiO_2) are amphoteric, which means that the state of chemical reaction with both acids as well as bases leads to the production of salts and water. Here, it must be noted that there is a major disadvantage of using TiO_2 as a semiconductor for sensor applications [172]. The surface of TiO_2 is sensitive to humidity which leads to the unreliable response of sensors in atmospheres when the level of humidity is different [172]. In addition, all metal oxides have a hydroxyl group on the surface which leads to the same issue as with TiO_2 [172]. In order to improve these surfaces, Hexamethyldisilazane (HMDS) was used in this research to passivate the amphoteric surface of metal oxides (ZnO). The chemical reaction mechanism is shown in Figure 4.12; note that under ambient conditions HMDS is a liquid.

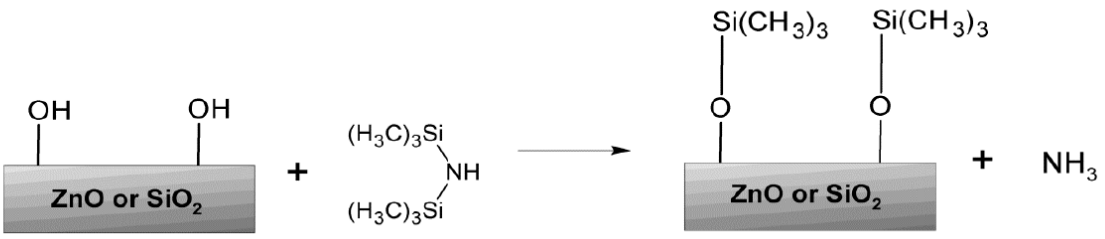

Figure 4.12 *The chemical reaction mechanism of superficial (metal oxide)-OH groups with HMDS.*

Initially, spray-pyrolysed ZnO transistor substrates were cleaned (as described in 4.1.1) before HMDS treatment occurred. Then, ZnO transistor substrates were placed into a vacuum oven pre-heated to 80 ^{o}C. The oven was evacuated but then the evacuation valve was shut, and the air inlet valve was briefly opened so that ~ 1 mL of HMDS could be spayed into the oven where it vaporised. Films were kept in this atmosphere for 2 hours to facilitate the reaction shown in Figure. 4.12. Subsequent contact angle measurements with water confirmed the transformation of the ZnO surface from hydrophilic to hydrophobic (full details in section 5.1.3).

In this chapter, the preparation of transistor substrates (supporting substrates, contact substrates and semiconductors) with organic semiconducting polymers as hole transporters or surface-passivated precursor-route ZnO as an electron-transporting semiconductor has been fully described. In chapter 5, the way in which such TFT substrates are gated with water to form WGTFTs and how such devices are characterised will be explained.

Chapter 5: Devices and electrical characterisation of WGTFTs

This chapter begins with an introduction of the various techniques used to characterise the thin films that formed a transistor substrate deposited using the methods described in chapter 4. This is followed in section 5.2 by a description of the method used in this research to transform transistor substrates into transistors. The chapter ends with a summary of the transistors' electrical characterisation.

5.1 Characterisation of thin film morphology and electronic properties

In the following section of this chapter, the devices that were utilised to study the morphology and properties of TFT semiconductors such as optical microscopy, surface profilometry and contact angle goniometry are described.

5.1.1 Optical microscopy

Optical microscopy is a method used to closely inspect a sample via magnification and was used in this study to check the quality of contact substrates (reported earlier in section 4.2). Before preparing the transistor substrate (reported earlier in section 4.3), a final step was required to check for any shorts and misalignment between drain and source contact or for an unwanted connection in the channel area. This is because shorts might have occurred if the supporting substrates were wrongly placed through the process of evaporant with a shadow mask. Figure 5.1 illustrates a contact substrate and channel area with dimensions W= 30 μm and L= 1mm which was evaluated with the help of a scale bar that was calibrated according to the manufactures specifications (reported in section 4.2).

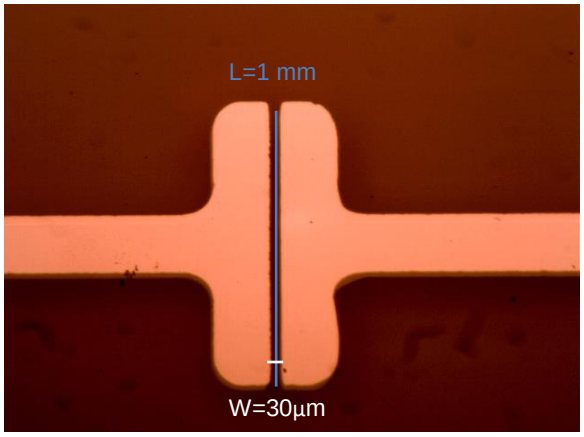

Figure 5.1 *Image of a contact substrate and channel area measured by optical microscopy.*

5.1.2 Surface profilometry

A surface profilometer measures the contour of a surface in one dimension with a vertical resolution sub-nm over the range of 6.5 µm. It then laterally scans within a single direction across the surface of the sample for a specific distance. Surface profilometers exist in two forms; namely, non-contact profilometers (optical profilometers) and contact profilometers. In our work, we used a Veeco Dektak XT Surface contact profilometer as shown in Figure 5.2 to determine the thickness of deposited semiconductors by scanning across the profile of scratches that were previously scratched in the film using a scalpel blade. Thus, the depth of the resulting scratch was found by comparing the result with the thickness of the film prior to scratching.

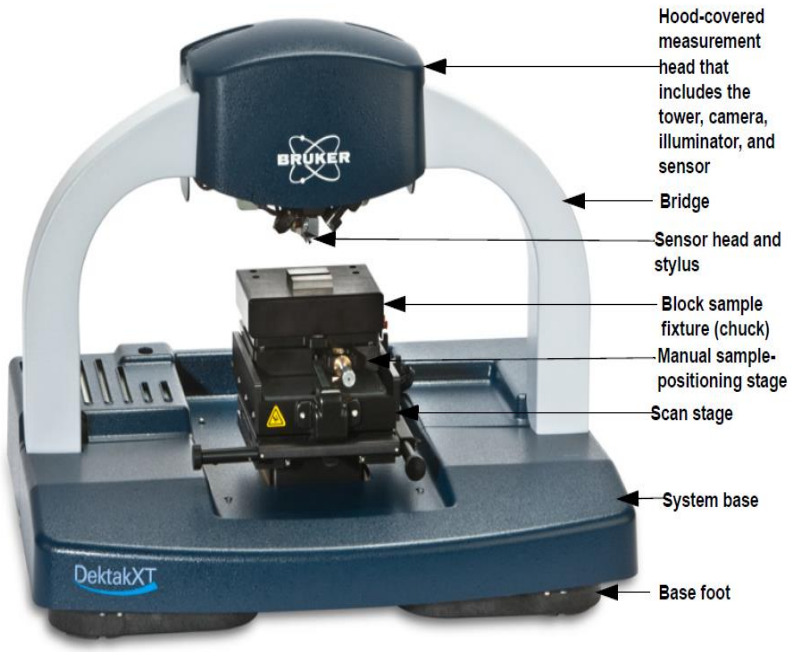

Figure 5.2 *Diagram illustrating the components of the surface profilometry instrument (Dektak XT) that was used in the laboratory [173].*

Surface profilometry consists of a stylus, sensors, scan stage and other components, as illustrated in Figure 5.2. In terms of their function, sensors determine the point at which the sample lies and the sample stage is used to hold the sample. The key component is the diamond stylus which is used as a probe to detect the surface. Based on the roughness of the surface, the stylus rebounds during the scanning process. Thus, the stylus' movement on the surface of the sample is converted from mechanical signals into electrical signals via a Linear Variable Differential Transformer. As demonstrated earlier, the mechanical movement is

monitored with a feedback loop designed to measure the force from the sample pushing up against the probe as it scans along the surface. In terms of data processing, the profile of the surface is noted and preserved digitally. After this, the data are evaluated and presented in the form of a single-dimensional height profile.

Figure 5.3 *Profilometry data output graph showing ZnO film thickness as 80 nm. A spray pyrolysed film was deliberately scratched on the supporting substrate in the red-shaded zone to reveal its original thickness.*

As an example from our measurements, Figure 5.3 displays ZnO film thickness of 80 nm as measured by the Veeco Dektak XT Surface after spraying 3 'puffs' of ZnO. This is classed as significant roughness; however, spraying fewer than 3 puffs does not lead to working devices. On the other hand, there is no case for spraying more often, as TFT operation generally does not improve with thicker semiconductor films.

5.1.3 Contact angle goniometry

Surface tension occurs between a solid surface and a drop of liquid – often water – and is defined by the moment when the fluid surface tends to shrink into the minimum surface area. It is measured in Newton/meter or Joules/m^2. Often, those investigating surfaces place drops of water on a surface to investigate its properties (i.e. determination of the shape or form of the liquid droplet on the surface according to the surface tension of the liquid). The drop's

edge makes an angle with the surface which is related to the surface tension as defined by Young's Equation [174, 175]:

$$\sigma_{SG} - \sigma_{SL} = \sigma_{LG} cos\theta_C \qquad 5\text{-}6$$

Where σ_{SG} is the solid–vapor interfacial energy, σ_{SL} is the solid–liquid interfacial energy, σ_{LG} is the liquid–vapor interfacial and θ_C is the equilibrium contact angle. The water/semiconductor interface is particular interest to our study because we are investigating WGTFTs.

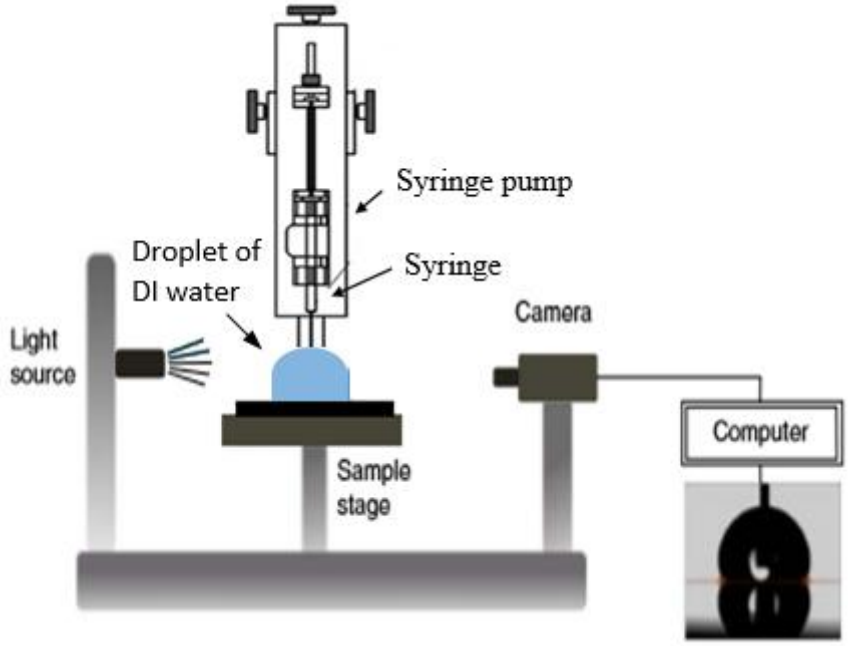

Figure 5.4 *Schematic diagram of contact angle goniometer instrument[175].*

Surface tension can then be calculated from the contact angle – the angle briefly created by the intersection of the liquid-vapour interface and the liquid-solid interface – using Young's equation. Surface cleanliness after and prior to cleaning operations, rinsing process effectiveness, and the ease of surface wettability by waterborne coatings have all been estimated using water contact angles [175]. Another advantage of studying contact angles is that it allows the determination of the extent of hydrophobicity or hydrophilicity of the material. When the contact angle is smaller than 90^o it is classed as a hydrophilic; larger than 90^o it is classed as a hydrophobic [176].

In this work, a goniometer instrument with software and a camera for capturing and analysing the drops' shapes was used to measure the contact angle (see Figure 5.4). The goniometer was connected to Attension Theta software package to identify contact angles for deionised water on semiconductors (ZnO films and rrP3HT) [163]. The most important consideration here was the effect of surface passivation as occurs with HMDS (discussed in section 4.4) and as an example of HMDS treatment on ZnO, as reported below. Figure 5.5 shows the contact angle of two thin films of ZnO. The first is untreated ZnO film and has a contact angle of 12.8°; the second is HMDS-ZnO film and has a contact angle of 84.7°.

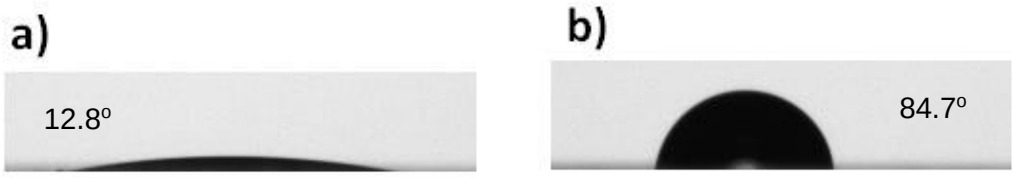

Figure 5.5 *The contact angle of (a) untreated ZnO thin film and (b) HMDS-ZnO.*

5.2 Electrical characterisation of WGTFTs

In section 4.3, the method of transistor substrate manufacture was reported. In this present section, the method of transforming a transistor substrate into a transistor by gating across a drop of electrolyte (specifically water) is described and shown in Figure 5.6. (bottom). Following this, the electrical characterisation of water-gated thin film transistors is explored such as transfer and output characteristics (also reported in section 3.1). Finally, the way in which these characteristics are analysed to calculate TFT parameters is explained; namely, the threshold voltage V_{th}, charge carrier mobility μ, inverse subthreshold slope *SS*, on/off ratio and transconductance g_m.

5.2.1 Source measure units

This study employed two Keithley 2400 source measure units regulated using bespoke LabView software, as shown in Figure 5.6 (top). The units can be utilised for sourcing voltage and measuring the resulting current or as the source of current whilst determining the voltage required for driving the set current. Here, I only used the voltage source – current meter option. One of the transistor substrate contacts was connected using a contact needle

positioned with a Suss microtec PH100 probehead and linked to electrical ground via a coaxial cable. This contact was the ‘source’ (S) contact of the water-gated TFTs built in this setup. The other contact, which became the ‘drain’ (D) contact, was connected in the same way but was linked to a Keithley 2400 source/measure unit used in voltage source/current measurement mode. Following this, the transistor was formed by applying a gate voltage and contacting the electrolytic gate medium (water) as shown in Figure. 5.6 (bottom). It should be noted that the gate Keithley does not only apply gate voltage but also measures gate current albeit ideally that should be zero.

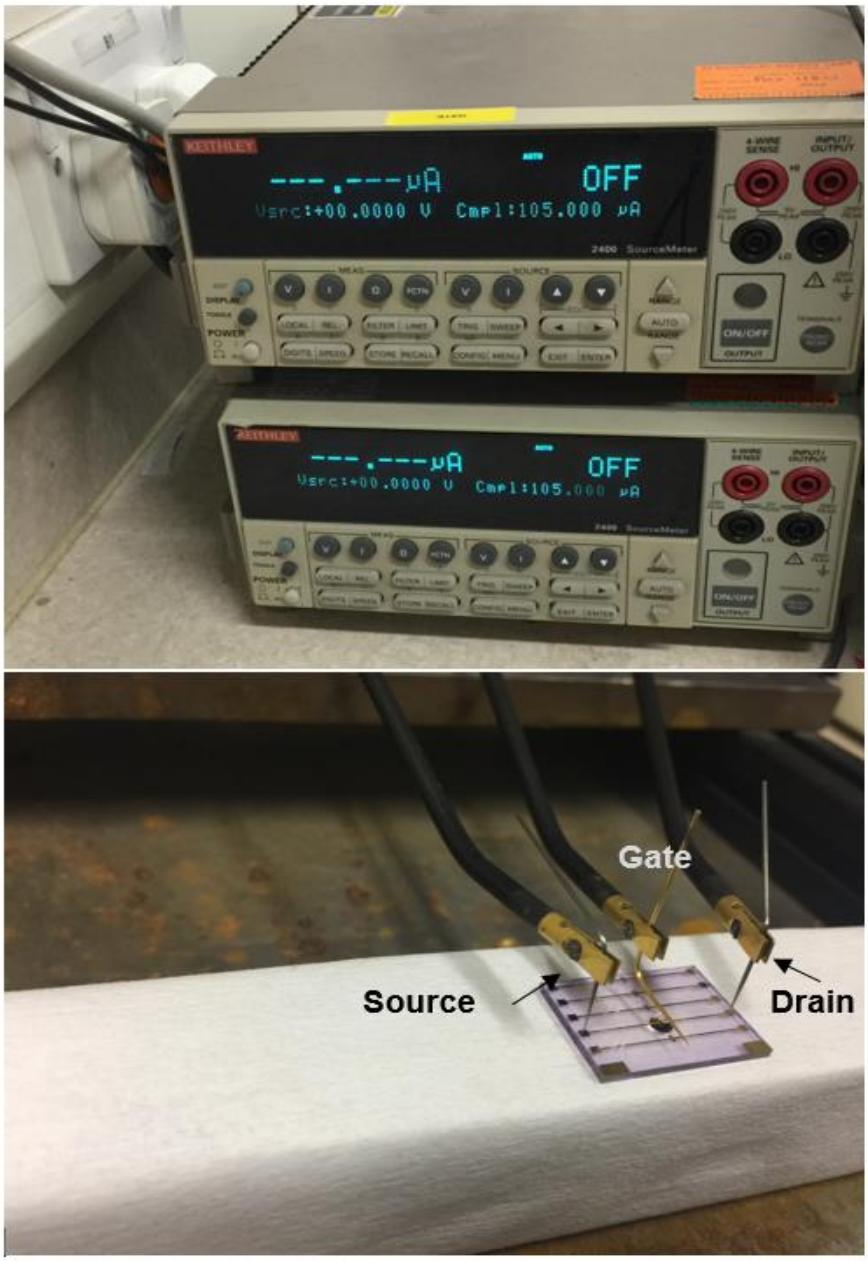

Figure 5.6 *A photograph of two Keithley 2400 source measure units* ***(top)*** *and the three probeheads of FETs instrument: the needles are connected to the right electrode and overlap the droplet that covers the channel area (rrP3HT TFT)* ***(bottom).***

To record output and transfer characteristics, the Keithley 2400 devices were linked to a PC running bespoke LabView software through GPIB-PCI cables that were developed by two former post-graduate students from our research group, Dr. Lee Hague and Dr. Antonis Dragoneas. Besides selecting between transfer and output characteristic measurements, the software allowed setting a number of measurement parameters. These included voltage range, step size, delay period between the steps, voltage step size, and repeated measurements sweeping voltage from zero to positive or negative values and then back to zero. After choosing the desired parameters, the software took measurements in automated mode, as shown in Figure 5.7, and 5.8, displayed the results and transmitted them in the form of excel data files for comprehensive analysis.

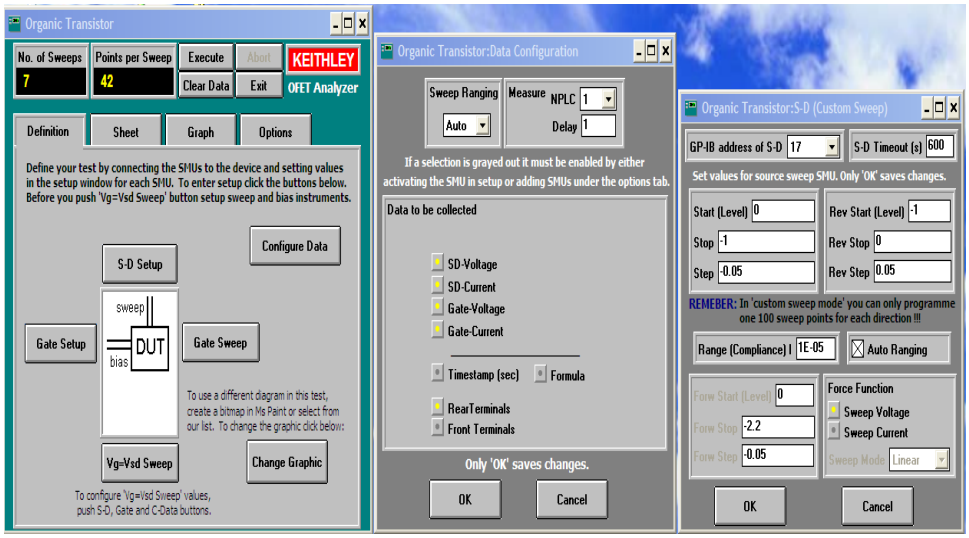

Figure 5.7 *Screenshots of the user interface of our bespoke LabView software developed by Dr. Lee Hague and Dr. Antonis Dragoneas. The software was set to record output characteristics.*

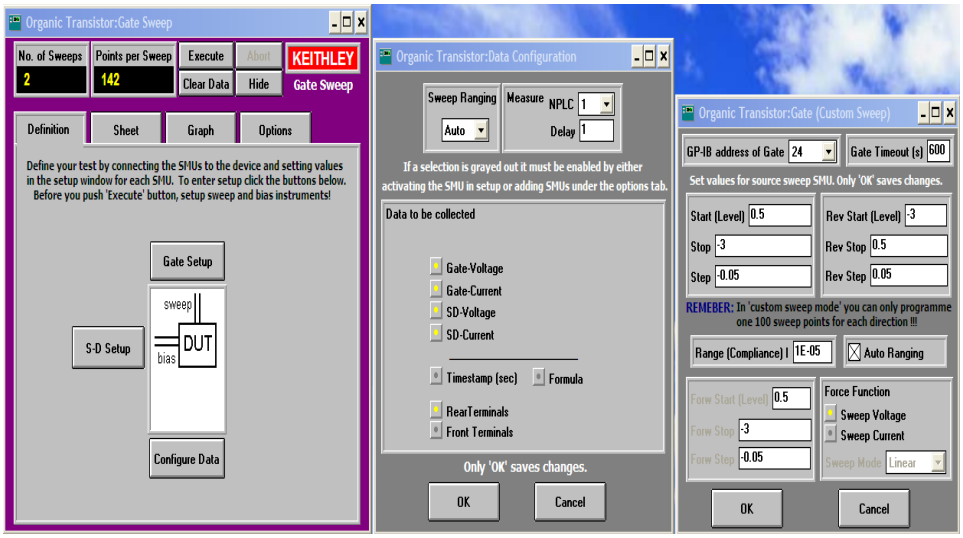

Figure 5.8 *Screenshots of the user interface of our bespoke LabView software developed by Dr. Lee Hague and Dr. Antonis Dragoneas. The software was set to record transfer characteristics.*

5.2.1.1 Output characteristics

An output characteristic is a relation between the drain current (I_D) and source-drain voltage V_{SD} taken for a set of different but constant gate voltage V_G.

Note, since source is defined by electrically grounding the source contact, source voltage is zero by definition, and $V_{SD} = V_D$. This is recorded by sweeping V_D in several small steps beginning from 0 to maximum modulus (usually 1 V or less in our work, i.e. water) and returning to 0 within reversed steps. In this case, gate voltage V_G does not change. To characterise a 'normally off' (accumulation mode) transistor, gate and drain voltages must have opposite polarity to that of the semiconductor carrier. The procedure is repeated for several V_G, thus resulting in a family of $I_D(V_D)$ characteristics' parametric within V_G.

Output characteristics play an important role in diagnosing if practical TFTs conform to theoretical behaviour as indicated within section 3.1, or if there are deviations that indicate non-ideal properties of one or several components of the transistor. Figure 5.9 presents a graphic illustration of output characteristics similar to those given in Eq. 3-8, section 3.1; implying adherence to those equations. At low V_D, there is linear behaviour $I_D \sim V_D$ whereas, at high V_D, I_D undergoes saturation (does not increase with an increase in V_D).

When the I_D value continues to rise steadily within the saturated regimes at high drain voltage, doping within the semiconductor of the TFT is implied. Moreover, doped semiconductors carry an ohmic current independent of gating. This can be modelled by an ohmic resistor that runs parallel to TFT. It should be noted that hysteresis (see section 5.2.1.5**)** might emerge within output curves due to impurities at the semiconductor and insulator interface or the bulk of the semiconductor. Furthermore, if the output characteristic does not cut across the origin, but the I_D close to $V_D = 0$ is of opposite sign to I_D at high modulus of V_D and increases with increasing gate voltage, this indicates gate leakage (i.e. a non- zero current from S or D (or both) to G).

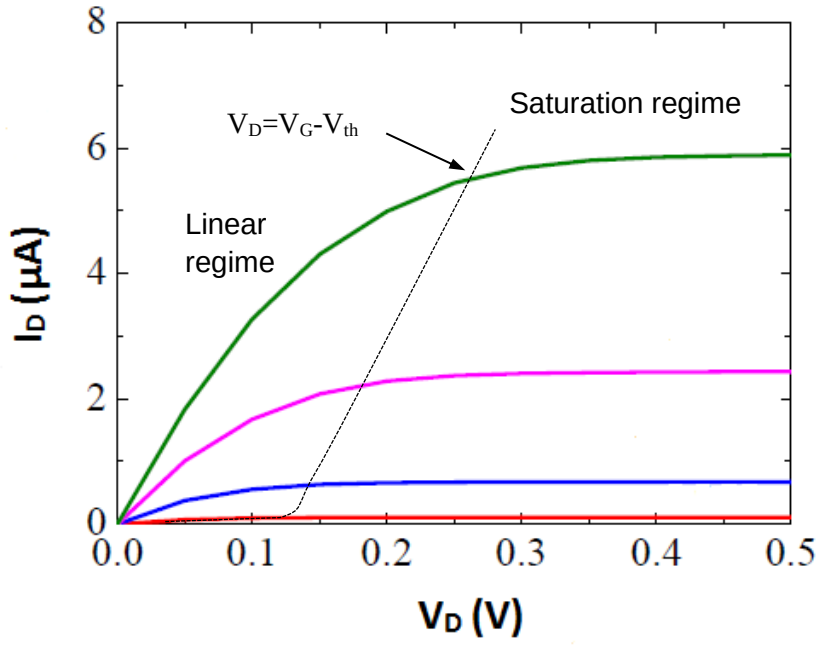

Figure 5.9 *Example of typical output characteristics for n-type TFT showing both regimes (linear and saturated). The dashed line separating the regimes is derived from $V_D=V_G-V_{th}$. Moreover, TFT reaches pinch off. Further pinch off, I_D tends to be independent of the applied V_D and starts to saturate.*

5.2.1.2 Transfer characteristic

A transfer characteristic is a relation between the drain current (I_D) and gate voltage (V_G) for constant source-drain voltage (V_D). Linear and saturated transfer characteristics are described in section 3.1 in full detail. Figure 5.10 illustrates the linear transfer characteristic at the negligible drain voltage value (V_G, max >> V_D) whereas the saturated transfer characteristic is illustrated when a significant source-drain voltage value (V_G, max < V_D) was used. Furthermore, Figure 5.11 shows the saturated transfer characteristic plotted on logarithmic or square root scale of (I_D) vs (V_G). This corresponds to the saturated drain current and sub-threshold behaviour equations explored in section 3.1.

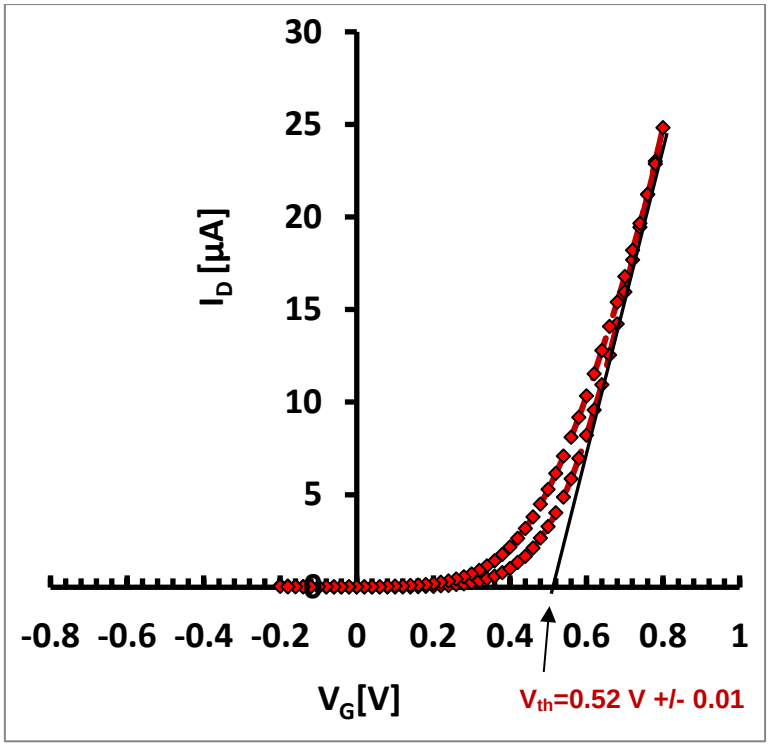

Figure 5.10 *Example from our results illustrating a linear transfer characteristic of water-gated ZnO TFT. The black line fitted at high gate voltages shows how threshold voltage can be determined.*

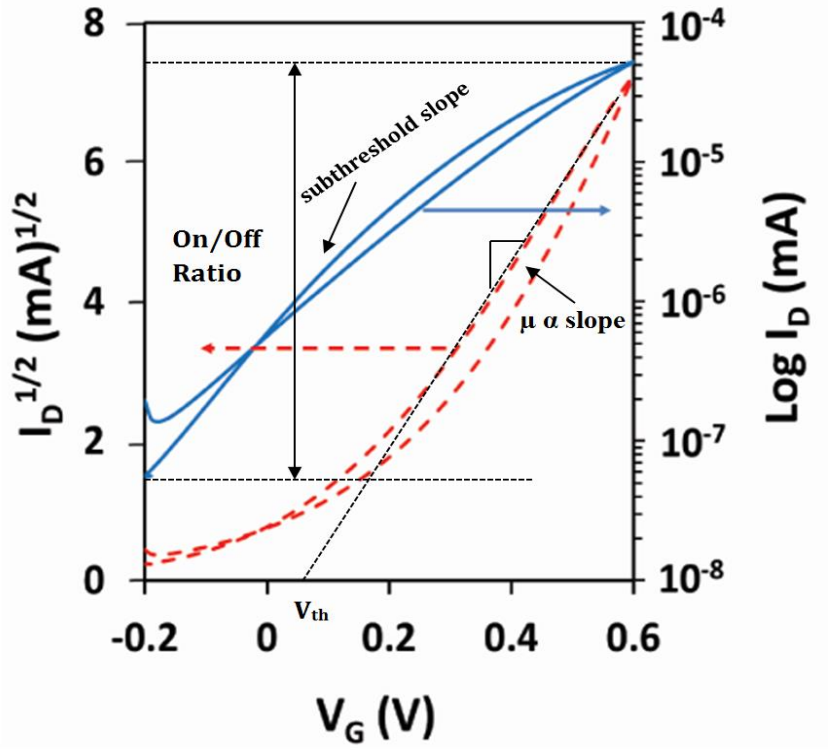

Figure 5.11 *Saturated transfer characteristic of ZnO TFT. The same characteristic is plotted twice: once against $I_D^{1/2}$ and once against log I_D. Several straight lines are fitted to evaluate inverse subthreshold slope, on/off ratio, carrier mobility and threshold voltage.*

5.2.1.3 Evaluation of TFT parameters from transfer characteristics

5.2.1.3.1 Threshold voltage (V_{th} or V_T)

Threshold voltage is the most important characteristic in this work and is discussed in full detail in section 3.1. Briefly, threshold voltage V_{th} is the gate voltage where an accumulation mode transistor first develops an accumulation layer in the channel: we say it 'switches on'.

Practically, threshold voltage V_{th} can be extracted from transfer characteristics by one of two ways [35]: from linear transfer characteristics, by considering the intersection between the extrapolated linear fit to (I_D) at high V_G and the V_G axis, as shown in Figure 5.10; and from saturated transfer characteristics by considering the intersection between the extrapolated linear fit to the square root of (I_D) and the V_G axis, as shown in Figure 5.11.

5.2.1.3.2 Charge carrier mobility (μ)

Charge carrier mobility μ [35] is defined as the ratio of carrier drift velocity and electric field, as defined in section 3.2.2.4, and represents one of the key performance parameters of a semiconductor. The commonly used unit of measurement for mobility is $cm^2\ V^{-1}\ s^{-1}$. The orders of magnitude of mobilities we find in different families of semiconductors with different carrier transport mechanisms have been reviewed in section 3.2.2.4. In the linear regime, carrier mobility at high gate voltages are related to the linear transfer characteristic as described by Eq. 5-7:

$$\mu_{lin} = \frac{L}{WC_i}\left(\frac{\partial I_D}{\partial V_G}\right) \qquad 5\text{-}7$$

Wherein C_i denotes the specific capacitance of the transistor's gate medium, W is the channel width, L refers to the channel length, I_D is the drain current and, V_G is the gate voltage. The derivative in Eq. 5-7 is the slope of the fitted line shown in Figure 5.10.

In the saturated regime, carrier mobility at high gate voltages is related to the saturated transfer characteristic as described by Eq. 5-8:

$$\mu_{sat} = \frac{2L}{WC_i}\left(\frac{\partial \sqrt{I_{D,sat}}}{\partial V_G}\right)^2 \qquad 5\text{-}8$$

The derivative in Eq. 5-8 is the slope of the straight line fitted to the dashed red line in Figure 5.11. Hence, when the specific capacitance C_i and TFT geometry W/L are known, mobility can be computed from TFT transfer characteristics by fitting straight lines, as in Figure's 5.10 and 5.11, and through the application of Eqs. 5-7 and 5-8.

However, when using electrolytic gate media, C_i is often strongly dependent on frequency, even when the frequency is very low, and can also somewhat depend on the concentration of salt in the gate medium [177]. C_i values quoted in the literature, therefore, do vary, albeit they are typically in the range (1-10) $\mu F/cm^2$ [15]. The reason for the high capacitance of such media was explained in section 2.3 of this thesis. Hence, the literature values for carrier mobility in electrolyte-gated TFTs must be regarded with care. Instead, rather than attempting to delineate the specific capacitance (gate medium characteristic) and mobility (semiconductor characteristic), it is recommended that the combined figure-of-merit μC_i as it appears in Eqs 5-7 and 5-8 in this combination is evaluated.

5.2.1.3.3 Inverse subthreshold slope (SS)

In section 3.1, subthreshold behaviour was introduced and the terms inverse subthreshold slope or subthreshold swing (*SS*) was defined along with its equation and units. Briefly, subthreshold behaviour is determined by evaluating saturated transfer characteristics plotted upon a *log* I_D *vs* V_G scale by fitting a straight line at gate voltages below V_{th} [35].

5.2.1.3.4 Transconductance (g_m)

Linear transconductance g_m is defined as the slope of the linear transfer characteristic ($|V_D| << |V_G - V_T|$), $g_m = \partial I_D/\partial V_G$, at high gate voltages. It is evaluated from linear transfer characteristics as before for Eq. 5-7, and is closely related to carrier mobility by Eq. 5-9

$$g_m = W/L\ \mu C_i V_D \qquad 5\text{-}9$$

Note the same ambiguity for C_i as discussed above.

5.2.1.3.5 On/Off current ratio

On/Off current ratio is the ratio of maximum and the minimum drain current in saturation regime of the transfer characteristic. As an example, for metal oxides, when I_{on}/I_{off} current ratio is 10^6 or higher, this is preferable for digital circuits[38]. However, an I_{on}/I_{off} ratio of

>10^4 is suitable for analogue circuits [38]. A TFT's on/off ratio is defined by the following equation:

$$\frac{I_{on}}{I_{off}} = \frac{I_D\,,(V_G,max)}{I_D\,,(V_G=0\,)} \qquad 5\text{-}10$$

From the *log* I_D *vs* V_G plot Figure 5.11, we can directly read the on/off ratio.

5.2.1.4 Threshold voltage shift via linear transfer master curve

In section 5.2.1.3.1, two methods to find threshold voltage from transfer characteristics were presented. However, both methods rely on fitting straight lines at high gate voltages and extrapolating to a low gate voltage intercept. In addition, both methods assume that measured characteristics follow the theoretical equation Eq. 3-8. In this work, we are mostly concerned not with determining an absolute value for threshold, but its shift when media with different concentrations of an analyte are used to gate the TFT. For our purposes then, Casalini et al. [106] have reported how to evaluate transfer characteristics for threshold shift (ΔV_{th}) in a parameter-free manner without fitting or reliance on theoretical models.

The method is illustrated in Figure 5.12. On the left, we see two linear transfer characteristics of the same transistor but gated with aqueous salt solutions of different concentrations (1 µM vs 100 mM of KCl solutions). The origin of the threshold shift due to salt concentration is an electrochemical membrane potential, as explained in section 3.4. To determine its magnitude, it is possible to fit straight lines, find their intercepts, and examine the difference of the intercepts. However, we instead used a simpler procedure: using the 1 µM (blue) characteristic as a reference and shifting the 100 mM (red) characteristic along the V_G axis by adding as many mV to it as needed to make the 100 mM characteristic match the 1 µM reference characteristic as closely as possible, as shown on the right of Figure 5.12. Shifting was optimised by trial and error iteration (visual first guess and subsequent improvement). The gate voltage shift needed for best overlap equals the threshold shift between the two characteristics: here we found that ΔV_{th} = -80 mV. The fact that the two characteristics could be brought to overlap well shows that only the threshold voltage was different between the two gate media. If carrier mobility or specific capacitance had also changed, the slope at high

gate voltage would have been different, but it was found to be virtually the same. Note how this procedure is independent of the precise mathematical form of the $I_D(V_G)$ characteristics.

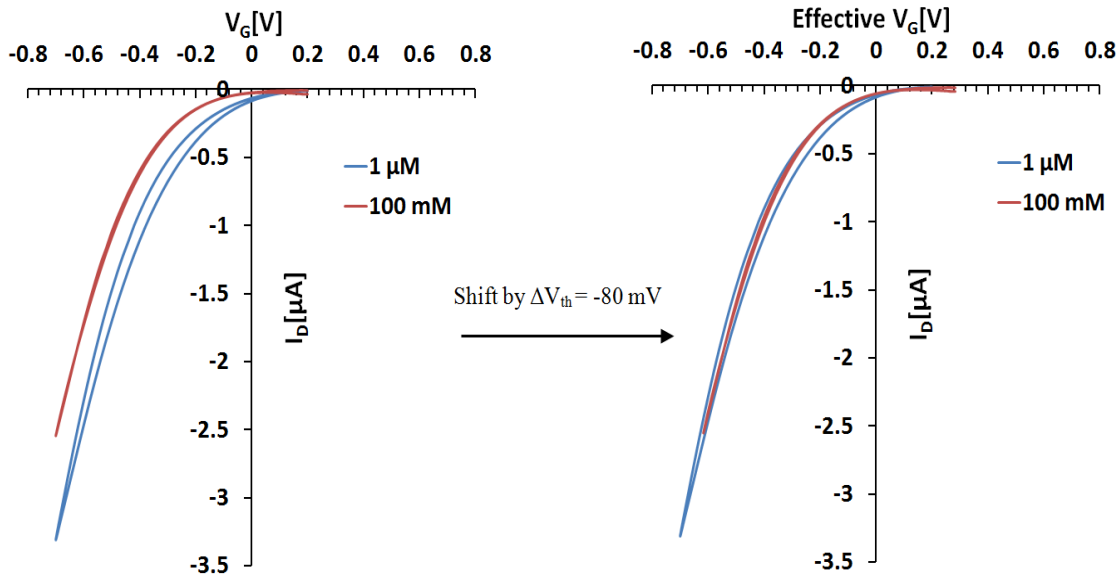

Figure 5.12 *Example illustrating the determination of threshold voltage shift ΔV_{th} via parameter- free shift procedure.* ***Left:*** *Original linear transfer characteristics of the same transistor substrate gated with different media (1µM vs 100 mM of KCl solutions).* ***Right:*** *The 100 mM characteristic was shifted laterally by 80 mV along the V_G axis to achieve the best overlap with the 1 µM characteristic that was used as a reference.*

When a set of transfer characteristics under different salt concentrations – c – in the gate medium are obtained, one of them (under low or zero salt concentration) is assigned as a reference, and all other characteristics are shifted by whichever voltage shift $\Delta V_{th}(c)$ gives the best match to the reference. In this way, a 'master curve' can be constructed that effectively extends the reference over a wider range than the original scan. After shifting, the former gate voltage axis is now labelled 'effective' gate voltage, as it no longer is the gate voltage that was actually applied (apart from the reference characteristic which is not shifted). The set of threshold shifts $\Delta V_{th}(c)$ needed to construct the master curve is the TFT's response characteristic to salt concentration, c, with $\Delta V_{th}(c_{ref}) = 0$ by definition.

5.2.1.5 Hysteresis

Hysteresis is the difference in the $I_D(V_D)$ or $I_D(V_G)$ characteristics when V_D or V_G is swept from zero to 'on' (positive/negative voltage for electron/hole transporting semiconductor) vs sweeping from 'on' back to zero. Hysteresis is often observed in particular in electrolyte-gated transistors, in particular when these contain an ion-selective membranes. Hysteresis is

caused, for example, by delays in releasing charge carriers from traps which are situated in the interface between dielectrics and semiconductors, and within the semiconductor bulk [178]. In some studies, ferroelectric gate media have been used to deliberately cause hysteresis for transistor memories [179, 180].

Hysteresis is illustrated in Figure 5.13 and is termed 'clockwise' or 'anticlockwise' according to the sense of 'rotation' between the off → on, and on → off, voltage sweep, as indicated by the arrows in Figure 5.13. The direction of hysteresis for p-type material is clockwise, whereas the direction of hysteresis for n-type material is anticlockwise [181].In addition, the direction can be changed from clockwise to anticlockwise when the gate voltage starts from a negative voltage $-V_g$ [182].

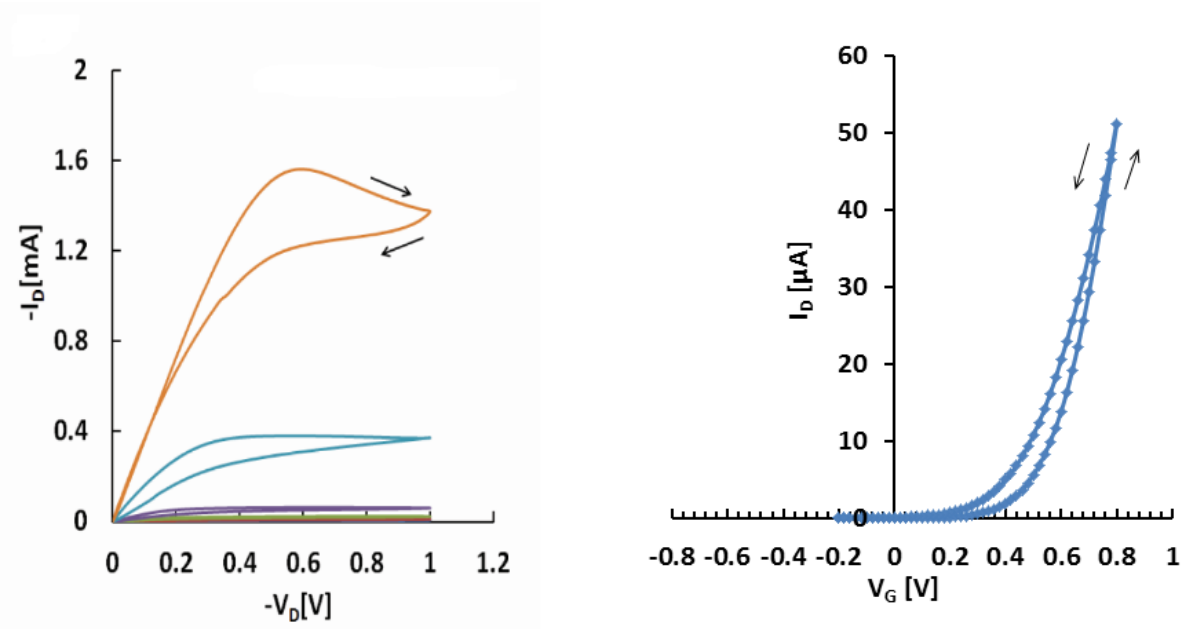

Figure 5.13 *Examples of output characteristic of PBTTT TFT* ***(left)*** *and transfer characteristic of ZnO TFT* ***(right)*** *showing clockwise and anticlockwise TFT hysterics respectively.*

Chapter 6: A membrane-free cation selective water-gated transistor

6.1 Introduction

Organic chemistry has designed more portable, affordable agents of organic metal complexing in the form of sensitisers, which can be bound to waterborne cations, known as (ionophores). Common examples of different macrocycles that have been reported recently, namely, phthalocyanines[183, 184], porphyrins[185], and calixarenes[87, 88], alongside conjugated crown-bearing ether ligand polymers[186], have been found to have highly selective metal cation complexes within their central cavities. One of the most important properties of cation is their selective macrocycle. In some instances, colourimetry could be used in the transduction of ionophores to retain optical absorbance that might be altered when cation complexation is used. In most cases, complexation, rather, leads to electrochemical transduction [e.g.[18]] by changing the potential in the interface.

The option to gate thin-film transistors (TFTs) with water and aqueous electrolytes [33] has led to their use as sensor devices for waterborne analytes. The presence of an analyte in the gating water leads to an interaction or binding of the analyte, either to the semiconductor itself or to a deliberately introduced analyte-specific sensitiser, which in turn is transduced into a change of the transistor's electrical characteristics. Analytes may be electrically neutral solutes (e.g.[45, 106], or ions (e.g. [15, 17]]. In the latter case, the quantitative response is, typically, approximately close to 'Nernstian' threshold shift, i.e. threshold shifts linearly with the logarithm of analyte concentration with 58/z mV/decade, wherein z is the ion's valency.

Here, we demonstrate a highly simplified design for an organic thin film transistor (OTFT) based ion sensor. Unlike previous studies[15, 17], our device requires no electrochemical reference electrode, and no sensitised membrane that separates a sample compartment. Instead, we add (1% wt./wt.) of a calcium-selective calix[4]arene ionophore, or "calcium ionophore VI" [96] as a sensitiser to rrP3HT spin casting solution. We find that resulting WGTFTs cast from ionophore- doped rrP3HT solutions selectively respond to calcium cations dissolved in the gating water with similar characteristics as previous ion- selective WGTFTs. The ionophore- doped rrP3HT simultaneously acts as a semiconductor, and ion-

sensitive layer, without the need for a separate ion- selective membrane. This method can be used in general with other selective cation macrocycles.

6.2 Experimental details

6.2.1 Device Preparation, Materials and Solutions

Supporting substrates coated with 20 nm of SiO_2 were used for fabricating transistor substrates (details in Chapter 4). Briefly, an Ossila shadow mask is used for preparing and depositing drain/source contact pairs (Cr 10nm as adhesion layer/ Au 120 nm) by thermal evaporation. Each substrate contains 5 pairs of electrodes separated by a channel with a length L = 30 µm and width W = 1 mm (W/L = 33.3). The hole transporting semiconducting polymer regioregular poly (3-hexyl)thiophene (rrP3HT) was purchased from Sigma Aldrich (Cat. No. 698989, average M_n 15,000-45,000) dissolved at 10 mg/mL in 1,2-dichlorobenzene (DCB) at 75 ^oC and filtration undertaken using 0.45 µm polytetrafluoroethylene syringe filter. Regarding preparing the sensitiser, we added 0.1 mg/mL (1% wt. /wt.) 'Calcium ionophore VI' to the similar casting solution of rrP3HT. According to McKittrick et al. [96], Calcium ionophore VI sourced from Sigma Aldrich (Cat. No.72385) is a calix [4]arene macrocycle (Figure 6.1 in the inset) that selectively complexes Ca^{2+} in its central cavity. McKittrick *et al*. [96] used it practically with PVC membrane under classic potentiometry in the detection of waterborne Ca^{2+}. Notably, sensitisation of the rrP3HT was not undertaken in the control measurement. Completion of TFT substrates was achieved by spin casting them on the contact substrates for 60s at 2000 rpm. When casting had been completed, dynamic vacuum at 110 ^oC for 40 minutes dried the films.

Preparation of stock solutions of $BaCl_2$, NaCl, KCl, $ZnCl_2$ and $CaCl_2$ was undertaken at a concentration of 100 mM within deionised (DI) water. A stock solution for $CaCl_2$ was subjected to a repetitive dilution ten times downwards to 1 µM. PTFE films with little windows for exposure of individual drain/source contact pairs to intermediate transistor channel covered substrates of the transistor. A small plastic chamber with a capacity of 50 µL was positioned on the window (active area) and filled using DI water for accurate measurement. Afterwards, the plastic chamber was drained and filled with $CaCl_2$ solution that ranged between 1 µM and 100 mM, increasing in concentration. Similar tests were done for

fresh substrates of OTFT substrates on NaCl, KCl, $ZnCl_2$ and $BaCl_2$ but only using DI water and a concentration of 0.1M.

6.2.2 Electrical Measurements

In section 5.2, I have described the technique that was used to measure TFT characteristics with high precision Keithley 2400 source measure units. Electrical measurement of TFT's was through an L-shaped Au gate needle that touched the aqueous gate media surface. Electrochemical reference electrodes were not utilised within the experiment, as illustrated in Figure 6.1. Transfer characteristics of OTFT were recorded through shifting the voltage of the gate V_G which is started from 0.2 to -0.7 V and then returns to 0.2 V in 0.02 voltage steps at constant drain voltage V_D = -0.3 V. Following every step of gate voltage, 2 seconds were allowed for equilibrium prior to recording the current of the drain I_D (V_G). Minimal hysteresis was identified between the ramping points of the gate voltage. Following every measurement, DI water was used for washing gate needles.

To locate the shift in the threshold voltage ΔV_{th} between the gated OTFTs (sample solution) and DI water, the transfer characteristics of the gated sample and those for DI water-gate were plotted on one graph, and sample-gated characteristics were shifted along the V_G axis to determine the suitable overlap of the DI gate's characteristic. The threshold voltage constitutes the required shift to achieve the best-matched overlap as indicated in Figure 6.3(b).

A similar method of detecting OTFT of water-gated dopamine was adopted by Casalini et al. [106]. The depicted method does not follow a particular mathematical expression for $I_D(V_G)$ characteristic that holds for the existing case, as the transfer characteristics are neither saturated nor strictly linearised. The required change on the axis of the gate voltage was considered the change of the threshold in the concentration of ion and was attached to the use of the linear fitting routine within Origin software.

6.3 Results and discussion

The set up for sensitive water-gated OTFT that is used for sensing waterborne Ca^{2+} is illustrated in Figure 6.1; the section of the experiment presents the details of the procedure.

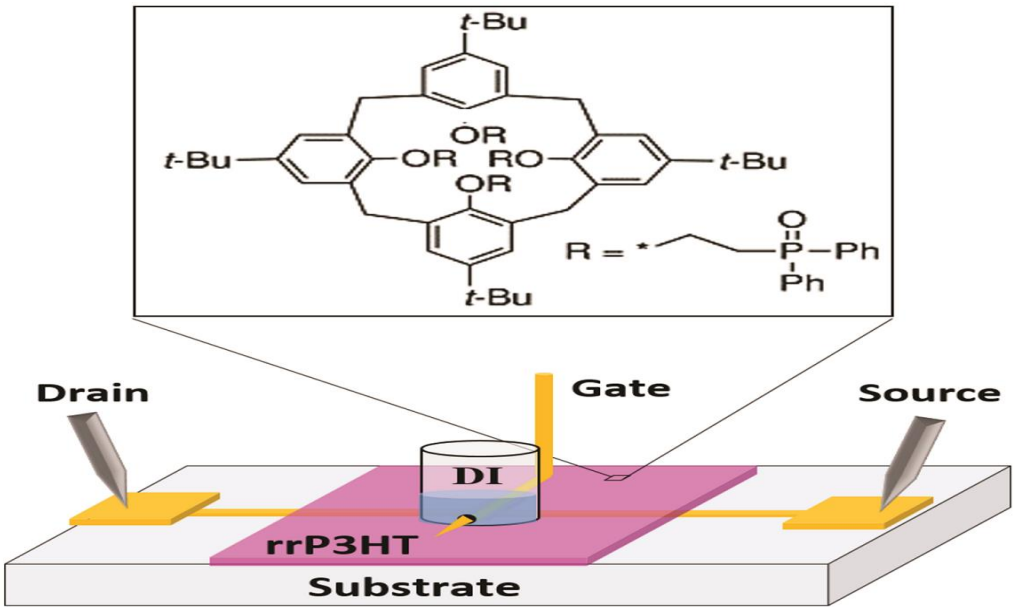

Figure 6.1 *Our device illustrates Ca^{2+} sensitive water- gated OTFT. 1% wt./wt 'calcium ionophore VI' shown in the inset which is embedded to spin casting solution of rrP3HT[84].*

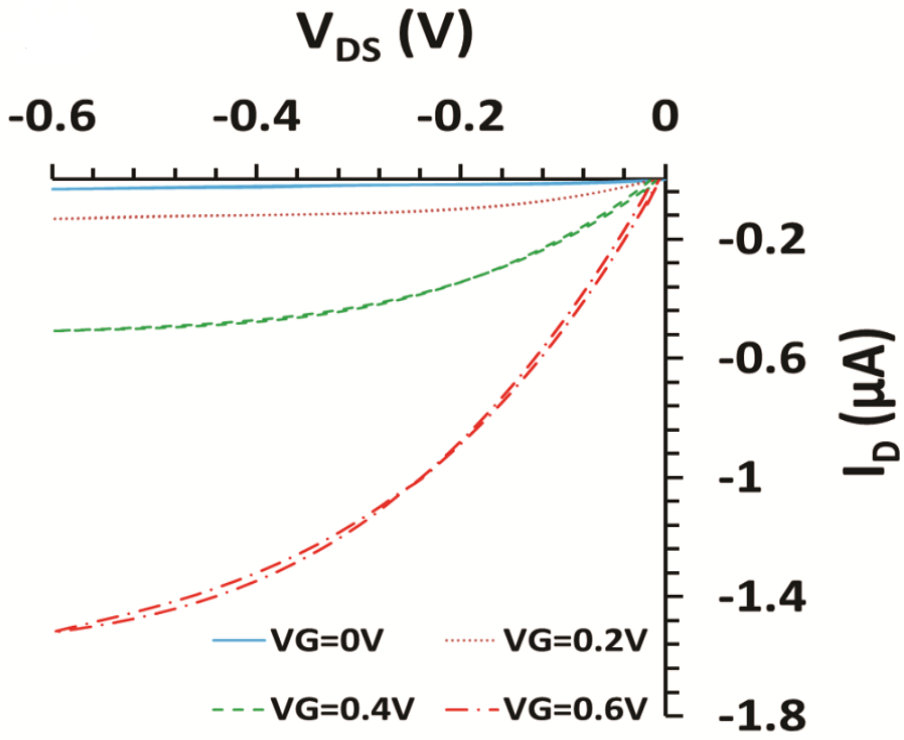

Figure 6.2 *Output characteristics of DI water gated OTFT sensor devices[84].*

Notably, the setup of this experiment resembles that for water- gated OTFT (e.g.[33]), with the only difference being that the film of the semiconductor here is doped by 1% wt./wt. of calcium ionophore VI. In addition, there are no electrochemical reference electrodes and no PVC membranes presented in this work. The OTFT output characteristic is illustrated in Figure 6.2, which is close to ideal, and the characteristic has a low threshold (≈ 0.2 V) with much less hysteresis. Arguably, the carrier mobility of ≈ 0.2 cm^2/Vs for water-gated rrP3HT: 1% ionophore film could be approximated through assumption of specified gate capacitance of (3 μF/cm^2)[33]. The application of rrP3HT films within water-gated OTFTs cannot be compromised when 1% ionophore is used in doping; however, it sensitises them selectively for identification of Ca^{2+} ions added to gated water, as illustrated below.

The transfer characteristic for 'Calcium ionophore VI'sensitised rrP3HT TFTs in a $CaCl_2$ solution and DI water of concentrations increasing from 1μM -100mM within factors of 10, all obtained from one OTFT substrate are presented in Figure 6.3. An increase of ΔV_{th} with an increment in the concentration of Ca^{2+} is indicated in Figure 6.3 (a). The master curve in Figure 6.3 (b) that quantifies it indicates that all transfer characteristics are shifted on the V_G axis for an ideal overlap with the characteristic of DI water. The ideal overlap characterising the curves is an indication that Ca^{2+} only affects the threshold, rather than the mobility of the carrier. The V_G shift needed to acquire the excellent overlap is considered threshold shift, $\Delta V_{th,}$ and Figure 6.4 illustrates its plot against the logarithmic concentration.

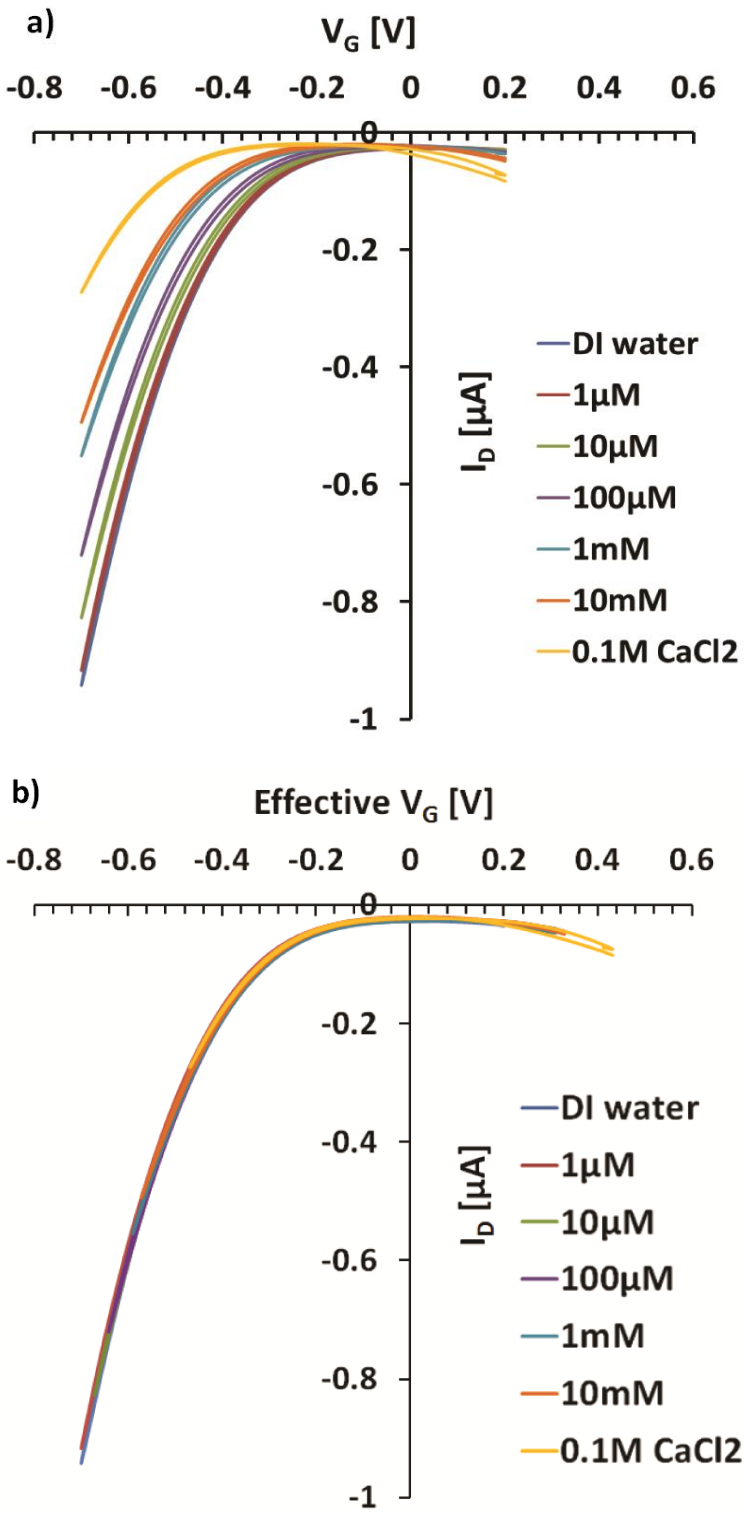

Figure 6.3 (a) *Transfer characteristics of water- gated rrP3HT TFTs which is 1% Calcium ionophore VI embedded to the film. Gating is with water with different concentrations of Calcium (Ca^{2+}, from $CaCl_2$), increasing from 1µM .. 100mM in factors of 10.* ***(b):*** *Transfer characteristic 'master curve' constructed by shifting characteristics along the gate voltage axis to give the best possible overlap with the characteristic under lowest (1µM) Ca^{2+} concentration.*

In section 3.4, the quantitative concept of Nernst equation and Nikolsky-Eisenman equation were investigated clearly. However, regarding the quantitative analysis of this chapter, I have mentioned again briefly.

$$\Delta V_{th} = s\Delta \log(a)\ (6a)$$

$$\Delta V_{th} = s\Delta \log(a + a_{st})\ (6b)$$

Where 58/z mV/decade represents the slope at a temperature of 20ºC, z represents the detected ions valency, that is, z = 2 for Ca^{2+}, and s = 29 mV/decade; a represents the activity of ions, whereas a_{st} denotes a constant characteristic for a system that is cation-sensitised. Consistent with equation 6, the shift in threshold voltage does not depend on the concentration of ionophore. Thus it was unnecessary to increase it here. Approximation of ion activities (a) in equation 6 is achieved through the concentration of ions (c). Regarding c >> c_{st}, equations 6a and 6b have a virtual similarity. Nevertheless, for negligible concentrations in the sequence c_{st} and less, the Nikolsky- Eisenman equation proposes a limit- of- detection (LoD) $c_{LoD} \sim c_{st}$ that is seen in practice but the Nernst equation that unrealistically seems to - ∞ for $c \rightarrow 0$ does not indicate it. For approximation of c_{st}, the experiment adopted this extrapolation: observed ΔV_{th} data was plotted against logarithmic (c) and fitted under high (c) with the linear fitting routines within Origin software, determining the slope (s) and limit of detection. The line was extrapolated towards low c to locate the concentration where determined data is over the extrapolated line via s log 2. Consistent with equation (6b), the concentration is equivalent to c_{st}. Here, the value of c_{st} is found to be = 3.7± 0.012 µM ~ c_{LoD}, and later ΔV_{th} *is* plotted against log (c) as indicated in Figure 5.4. The result is a straight line that aligns to slope s = 36.5± 2.2 mV/decade. Additionally, PVC membrane sensitised water-gated transistors exhibit a LoD in the sequence (1...10 µM)[15, 17], for certain electrochemical transducers, this could be minimal (e.g. 40 nM in[18]). When McKittrick et al.[96] undertook transduction of a similar ionophore through conventional membrane potentiometry, they did not show the value of a LoD explicitly; however, Figure 1 in [96] proposes a similar value as that is identified in this experiment.

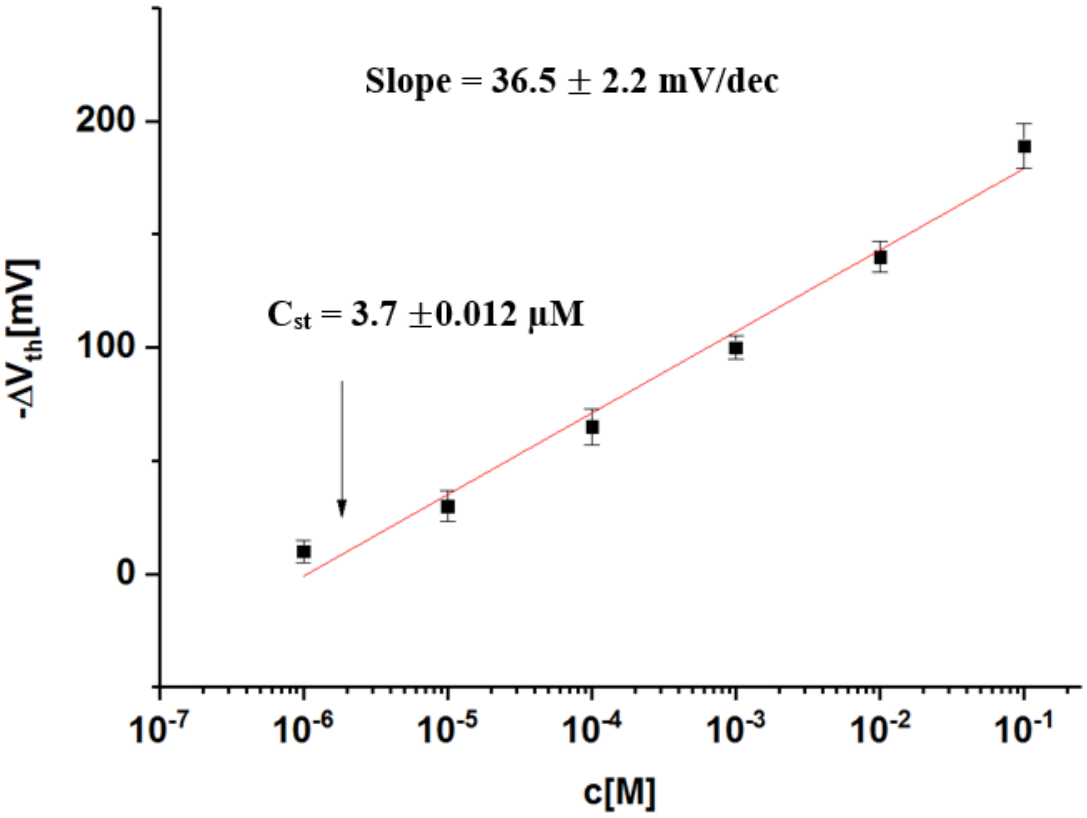

Figure 6.4 *Threshold shifts $\Delta V_T(c)$ in escalating concentration c for Calcium within the rrP3HT gated water: 1% Calcium ionophore VI OTFTs gated using an array of $CaCl_2$ aqueous solution concentrations.*

This was followed up using several controlled experiments Figure 6.5 to demonstrate that the result within Figure 6.3 is indeed caused by sensitising rrP3HT with calcium ionophore VI, and that our transistors are selective to the 'target' analyte Ca^{2+} over other waterborne cations. Next, a comparison of OTFT's gated using 0.1M cation solution against DI water gate is undertaken.

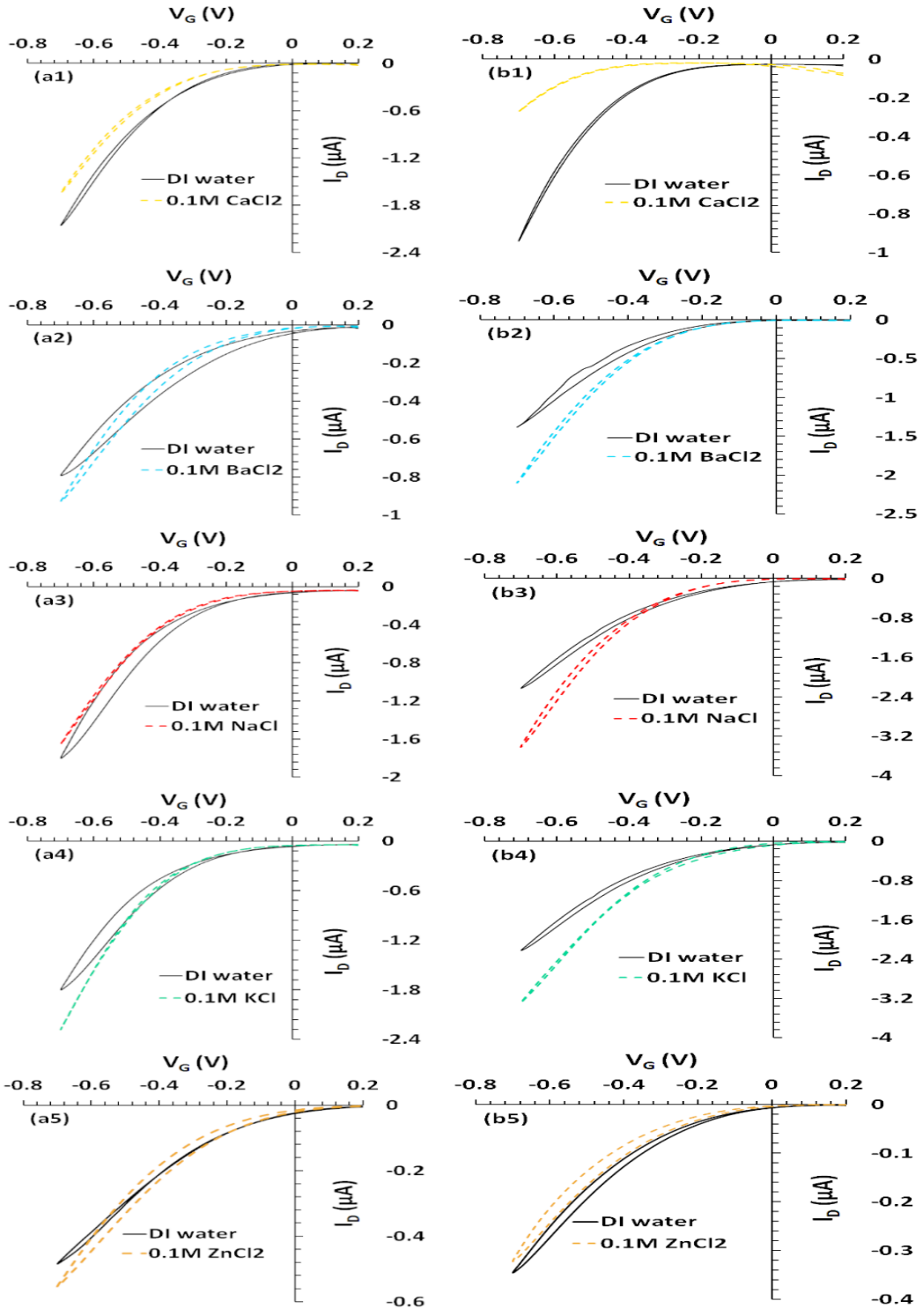

Figure 6.5 *Control experiment is shown in section* ***(a)*** *only rrP3HT TFT tested with different ions which is 0.1 M(Ca^{2+},Ba^{2+},Na^{+},K^{+},Zn^{2+}) as shown above from* ***(a1 to a5)*** *respectively.* ***(b)*** *with 1% 'Calcium ionophore VI' doped to rrP3HT TFT and tested with the same ions reactions. The selective sensitiser imparts high sensitivity to Ca^{2+} (b1) but not to other ions such as Ba^{2+} (b2), Na^{+} (b3),K^{+} (b4) and Zn^{2+} (b5)[84].*

Figure 6.5 (a1 and b1) provides a comparison of sensitised rrP3HT TFT against un-sensitised rrP3HT TFT gated using 0.1M $CaCl_2$, compared to DI water as the gating medium. While the transfer characteristic of the unsensitised transistor (a1) is identical in 0.1M $CaCl_2$ and DI water, the sensitised transistor (b1) exhibits a robust reaction to 0.1M $CaCl_2$ (consistent with Figure 6.3 (a)), the unsensitised transistor's transfer characteristic (a1) is very similar under DI water and 0.1M $CaCl_2$. This is a confirmation that rrP3HT does not exhibit innate sensitivity to bivalent cations. Indeed, sensitivity to calcium is achieved through the inclusion of 'calcium ionophore VI' to casting solutions. Figure 6.5 (a2 and b2) contrasts the reaction of sensitised and unsensitised rrP3HT transistors to other bivalent alkali cation, 0.1M $BaCl_2$. The two characteristics are identical as well as to the gated characteristic of DI water. This proves that 'calcium ionophore VI' has selectivity towards calcium, and does not impose barium sensitivities. Likewise, Figures 6.5 (a3 and 4) and (b 3 and 4) present a comparison of the sensitised and unsensitised rrP3HT TFTs reactions to 0.1M NaCl and KCl. Similarly, the reaction to 0.1M cation concentrations is negligible even for sensitised transistors (b 3 and 4), as well as in the other direction from Ca^{2+}. Moreover, McKittrick et al. [96]have identified the selectivity of Ca^{2+} for a similar ionophore over Mg^{2+}, NH^{4+} and Li^{+} with conventional membrane potentiometry and their results have shown a negligible reaction for un-sensitised OTFTs (a 3 and 4). Moreover, a sensitised transistor exhibits a negligible reaction to 0.1M Zn^{2+} (transition metal) as illustrated in Figure 6.5 (b5). To summarise the controlled experiments, it could be inferred that unsensitised rrP3HT transistors lack any response to gated water cations. Notably, rrP3HT transistors subjected to 1% 'calcium ionophore VI' respond selectively to Ca^{2+} ions within gated water with changes in threshold, but with the exception of other identical ions.

6.4 Conclusions

Two processes can be used to detect waterborne cations electrically with non-dissolving ionophores they include cation complexation through ionophore and complexation transduction into electrical signals through the related changes of the interface potential. Common sensors have divided these processes into two different functional parts, namely, a sensitised PVC membrane for ionophore/cation complexation, as well as an electrochemical transducer [e.g.[18]], or TFT[15, 17], for detecting the potential shift. This experiment combines the two functions into a single layer, which is placed in one step. We add (1% wt./wt.) of a calcium- selective calix[4]arene ionophore, or "calcium ionophore VI" [96]as a

sensitiser to rrP3HT spin casting solution. We find that resulting WGTFTs cast from ionophore- doped rrP3HT solutions selectively respond to calcium cations dissolved in the gating water with similar characteristics as previous ion- selective WGTFTs. The ionophore-doped rrP3HT simultaneously acts as a semiconductor, and ion- sensitive layer, without the need for a separate ion- selective membrane.

Chapter 7: Comparing electron- and hole transporting semiconductors in ion sensitive water- gated transistors

7.1 Introduction

The discovery of Kergoat et *al*. [33]that organic thin film transistors (OTFTs) can be gated using water as an electrolytic gate medium has opened the possibility of using such devices as transducers for the sensing of waterborne analytes. In contrast to the classic ion- sensitive field effect transistor (ISFET [102]), here the sample itself is an active part of the transducer. A number of workers have since demonstrated 'water-gated thin film transistor' (WGTFT) sensors for biologically relevant molecules [45, 106, 187, 188], pH [46], and specific cations [15, 17, 84], usually by introducing analyte-specific receptors ('sensitisers') into the WGTFT architecture. To sensitise for cations, cation selective 'ionophores' were used, e.g. calixarenes[84], or valinomycin [17]. The ionophore was introduced similarly as in conventional electrochemical (potentiometric) cation sensors [e.g.[18, 189]], namely, by including a plasticised PVC membrane with embedded ionophore in the WGTFT[15, 17], or alternatively, dispersed within an organic semiconductor film[84, 190]. The threshold of ionophore- sensitised WGTFTs shifted as a result of an ion concentration dependent membrane potential with characteristics logarithmic in ion concentration, similar to Nernstian (more precisely, Nikolsky- Eisenman) characteristics observed in potentiometric ion sensors

As an alternative to organic semiconductors, solution- processed precursor route inorganic semiconductors have recently gained popularity, as they can be processed with similar ease. Precursors may be metal acetates, chlorides, or nitrates, processed by spin casting and later pyrolysis, or spraying directly onto hot substrates (spray pyrolysis) from solutions in polar solvents or water. Pyrolysis converts such precursors into semiconducting oxides such as ZnO, SnO_2, TiO_2, IGZO or In_2O_3 [56, 120, 160-162]. These metal oxides lead to electron-transporting TFTs, while water- gated organic TFTs usually are hole- transporting. ZnO-based devices, in particular, have recently been widely used in various sensor devices [191-194].

We present here a systematic study comparing cation- sensitive WGTFTs using either, a hole transporting semiconducting polymer (rrP3HT), or an electron- transporting precursor- route metal oxide (ZnO), as the semiconductor. In both cases, we used a simplified WGTFT architecture, similar as Melzer et *al*. [17], where the ion- selective membrane was prepared on the gate electrode, and analyte solution is used as the gate medium. In the original report on WGTFT ion sensors, List- Kratochvil et *al.*[15], had instead used a more complicated two-chamber system where a free-standing membrane separated the analyte from a reference solution, with gating by the reference solution. As ionophore, we used water-insoluble dibenzo crown ether (Dibenzo-30-crown-10, DB30C10, inset Figure 7.1) [89, 195]. DB30C10 has previously shown sensitivity for potassium [196] and selectivity over sodium (selectivity constant 117) as established by the equipotential method in mixed Na^+/K^+ solutions in a potentiometric ion sensor [197], but so far crown ethers have not been introduced into ion- sensitive WGTFTs.

7.2 Experimental details

7.2.1 Device fabrication

In chapter 4, I have reported the preparation and fabrication of TFT used in my experiment. However, briefly transistor substrates were prepared by shadow mask evaporation of Au source/drain contact pairs with Cr adhesion layer (contact width W = 1 mm separated by an L = 30 μm channel; W/L = 33.3) onto clean supporting substrates (details described in chapter 4). The hole transporting semiconducting polymer regioregular poly(3-hexyl)thiophene (rrP3HT) was purchased from Aldrich (Cat No 698989, average M_n 15,000-45,000), dissolved at 4 mg/mL in toluene solution, heated gently at 75 °C for ≈10 min, and spin cast onto contact substrates at 2000 rpm for 60s. After casting, films were dried under dynamic vacuum at 120 °C for 1 h. The semicrystalline morphology of rrP3HT films used in sensors has been studied in detail before, e.g. [140, 198, 199]. Zinc oxide films were prepared by spraying 3 'puffs' of 100 mM $ZnCl_2$ solution in DI water onto similar TFT substrates heated to 400 ^oC on a hotplate, which leads to the formation of semiconducting ZnO films('spray pyrolysis', more processing details in [51]). Film thickness was determined with a Veeco Dektak XT surface contact profilometer as 15 nm for rrP3HT and 80 nm for ZnO; ZnO films also are significantly rougher. This agrees with the report of Lehraki *et al.* [168] who showed that spray pyrolysis from zinc chloride precursor leads to highest crystallinity (compared to acetate and nitrate) with largest crystals. This promises higher carrier mobility, but also leads to rougher films and the need for higher thickness to ensure continuity. After spraying, films

were first cleaned by DI water, isopropanol, acetone, and UV ozone. Then, ZnO films were treated with hexamethyldisilazane (HMDS) to passivate their amphoteric surface (reported earlier in section 4.4). This was by spraying ~ 1 mL of HMDS into the air inlet of a pre-heated (80 ^{o}C) and previously evacuated vacuum oven and keeping films in this atmosphere for 2 hours. A goniometer tensiometer coupled with Attension Theta software package was used to determine contact angles of deionized water on rrP3HT and ZnO films.

7.2.2 PVC membrane preparation

To prepare K^+ selective membranes, we mixed PVC membrane cocktails from 1.3% of potassium tetrakis [4-chlorophenyl]borate salt, 3.1% 2,3,17,18-Dibenzo-1,4,7,10,13,16,19,22,25,28-decaoxacyclotriaconta-2,17-diene ('DB30C10', Aldrich Cat. No 332518) ionophore, 30% poly(vinyl chloride) (PVC), and 65.6% 2-Nitrophenyl octyl ether as plasticiser, similar as in [17] . In total 100 mg of membrane components were dissolved in 3.5 ml of tetrahydrofuran (THF). An L- shaped Au needle was immersed in this solution for several hours, and then dried overnight, as in previous studies [e.g.[17, 18]]. Coated needles were pre-conditioned in 1mM KCl for several hours. Introducing the ion-sensitive membrane as a coating on the gate needle rather than as a free-standing layer was introduced by Melzer *et al*. [17] for a different ionophore.

7.2.3 Solution preparation and setup devices

Aqueous cation solutions were prepared by dissolving KCl or NaCl in deionised (DI) water to a concentration of 100 mM and repeatedly diluted to prepare sample solutions down to 1 nM. Transistors were completed using aqueous cation solutions as electrolytic gate media, starting at the lowest concentration (1 nM) and successively replacing them with solutions of increasing concentration. Electrolyte solutions were held in a small plastic pool of 50 μL capacity that was mounted over the TFT substrate's channel area, as described previously [84]. The solution in the pool was contacted with L- shaped Au needles overlapping the channel along its width to act as a gate contact. Figure 7.1 illustrates the resulting WGTFT architecture.

7.2.4 Electrical characterisation

In section 5.2, we described the technique used to measure TFT characteristic by Keithley 2400 source measure units.We recorded transfer characteristics by measuring drain current I_D at drain voltage, V_D = - 0.1 V for rrP3HT TFTs (+0.1 V for ZnO TFTs), while sweeping gate voltage V_G at 10 mV/s from +0.2 V to -0.7 V, and back to +0.2 V for rrP3HT TFTs (from -0.2 V to +0.7 V and back to -0.2 V for ZnO TFTs). After each gate voltage step, we allowed

2s for equilibration before recording drain current $I_D(V_G)$. We limited voltage sweeps to 0.7 V rather than the full 'electrochemical window' of water of 1.23 V because it was shown previously that rrP3HT long-term stability may be compromised at higher voltages[15]. Results are presented on a linear drain current (I_D) scale, and 'master curves' were constructed by shifting transfer characteristics along the gate voltage axis until they best matched with the 1nM characteristic. Carrier mobility was evaluated from master curves with standard transistor equations, assuming a capacitance of 3 $\mu F/cm^2$ [33]. The required shift along the gate voltage axis was taken as the threshold shift under respective ion concentration and was fitted to the Nikolsky- Eisenman equation (Eq. 7-2 below) with the nonlinear fit routine in Origin software.

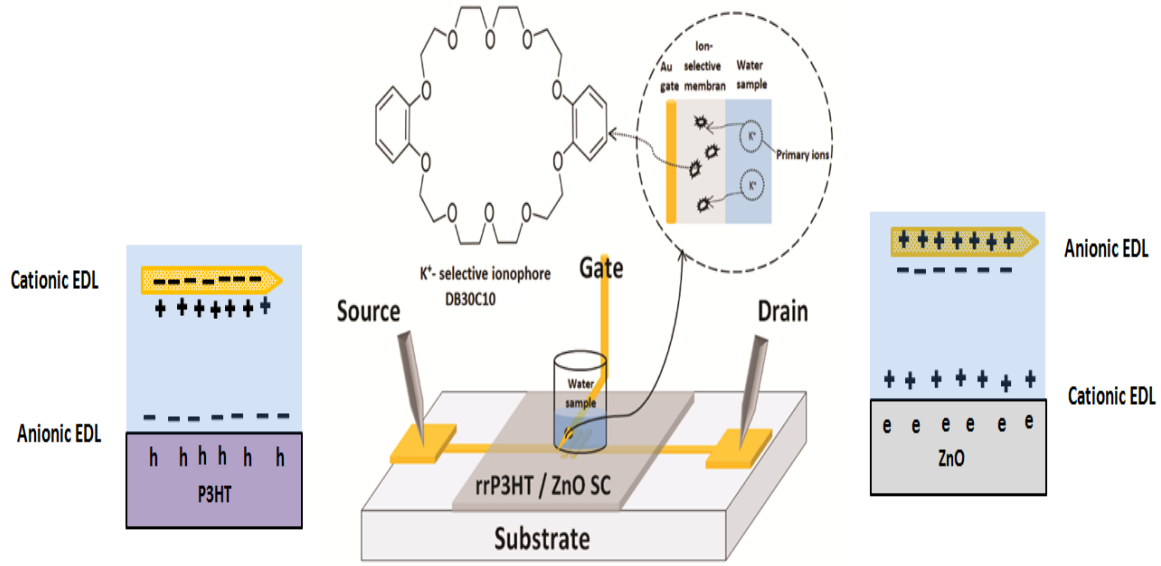

Figure 7.1 *Design of K^+ sensitive water- gated TFT. Au gate needle sensitised with DB30C10 ionophore embedded in a plasticised PVC membrane. The ionophore's molecular structure is shown in the inset. On both sides are the ratio of cationic to anionic electric double layers which leads to capacitative amplification or attenuation based on super- vs sub- Nernstian response characteristics in p-type vs n-type WGTFTs.*

7.3 Results and discussion

Figure 7.2a shows families of rrP3HT WGTFT linear transfer characteristics when contacted with a gate needle coated in DB30C10- sensitised PVC membrane, and gated with aqueous potassium solutions in the concentration range (1 nM … 100 mM). The transfer characteristic under deionised ('MilliQ') water (c = 0) is not shown here as it is effectively indistinguishable from the characteristics under 1 nM K^+, and later data analysis is on a logarithmic concentration scale which does not allow to show data for c = 0. All transfer characteristics are typical of the hole- transporting TFTs: Once the gate voltage is more

negative than a threshold, the TFT delivers a negative drain current of increasing magnitude as the gate voltage is made increasingly negative. Also, Figure 7.2a clearly shows that threshold becomes more negative, i.e. shifts away from zero, with increasing concentration c = $[K^+]$ for c above 100 nM, suggesting a limit- of- detection for potassium in the range (100 nM ... 1 μM). We find that all recorded transfer characteristics for $[K^+]$ > 1 nM can be brought to overlap with the $[K^+]$ = 1 nM characteristic by shifting them along the gate voltage axis by a concentration-dependent voltage shift, $\Delta V_T(c)$. As WGTFTs often display some hysteresis in the transfer characteristics, we here matched at the 'rising' flank of the hysteresis loop, i.e. when sweeping gate voltage from 'off' (near- zero gate voltage) to 'on', namely to increasingly negative gate voltage for a hole transporting semiconductor. However, hysteresis is small for rrP3HT WGTFTs. The resulting 'master curve' is shown in Figure 7.2b. In this way, we determine a threshold shift without assuming a specific model of the $I_D(V_G)$ characteristic. In Figure 7.2b and all future master curves, the gate voltage axis, therefore, does not show the actually applied gate voltage, but an 'effective' gate voltage that is corrected for the threshold shift,(effective V_G = applied V_G - $\Delta V_T(c)$). The required shift $\Delta V_T(c)$ is shown and analysed in context with other data in Figure. 7.10 and Table 7-1 below. Note that Giridharagopal *et al.* [200] have reported increased drain currents for non-sensitised rrP3HT WGTFTs under high concentrations (10 to 100 mM) of KCl, which they assigned to some penetration of chloride anions into the rrP3HT film. We can clearly exclude this here, as currents in Figure 7.2a are lower, not higher, under high KCl concentrations.

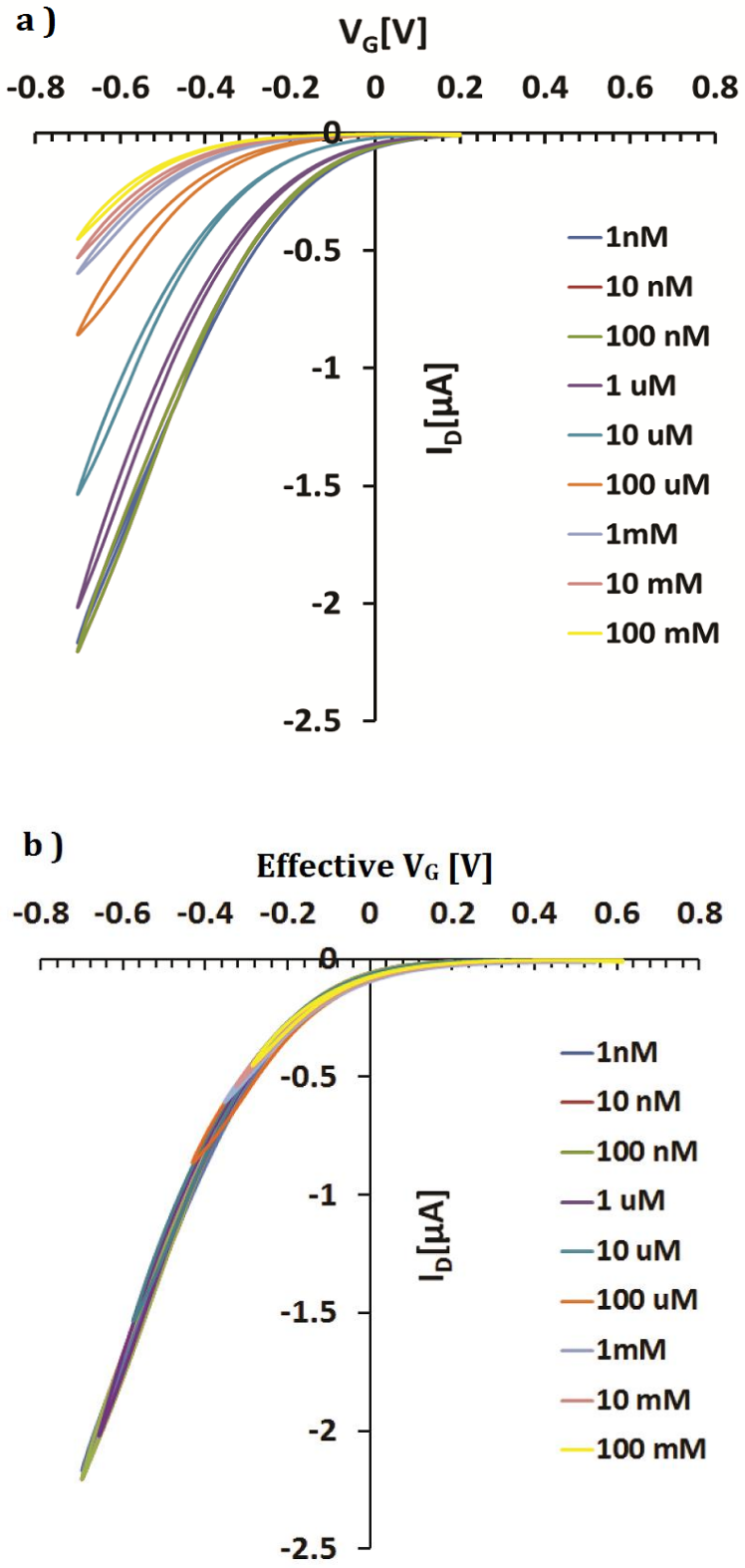

Figure 7.2 (a): *Transfer Characteristics of water- gated rrP3HT TFTs contacted by an Au gate needle sensitised with DB30C10 ionophore embedded in a plasticised PVC membrane. Gating is with water with different concentrations of potassium (K^+, from KCl), increasing from 1nM ... 100mM in factors of 10.* ***(b):*** *Transfer characteristic 'master curve' constructed by shifting characteristics along the gate voltage axis to give the best possible overlap with the characteristic under lowest (1nM) K^+ concentration.*

The ability to construct master curves by shifting transfer characteristics along gate voltage axis (here and also later in Figures 7.2b , 7.3b, 7.4b, 7.5b, 7.6b, 7.7b, 7.8b and 7.9b) does establish that $\Delta V_T(c)$ reflects only a shift of gate membrane potential in response to K^+ concentration, without concentration-dependent changes of carrier mobility or electrolyte capacitance. Otherwise, the transfer characteristics above threshold would differ in their slopes and would not project onto a single master curve, *cf.* Eq. 7-1 below. On the level of transistor operation that means K^+ ions in the gate medium do not interfere with carrier transport in the semiconductor, and the dependency of electrolyte capacitance on ion concentration is weak. The latter is reasonable as there will always be sufficient ions to populate a very thin double layer, which can migrate there from the droplet bulk.

Figures 7.3, 7.4 and 7.5 show three control experiments on rrP3HT WGTFTs. The response of DB30C10- sensitised rrP3HT WGTFTs to sodium instead of potassium in the gating water is shown in Figure 7.3, probing the selectivity of the sensor against an 'interferant'. Figure 7.4 and 7.5 show the response of rrP3HT WGTFT to K^+ and Na^+ respectively, when the gate contact was not sensitised. Corresponding $\Delta V_T(c)$ are also shown and analysed in context in Figure 7.10 and Table 7-1 below

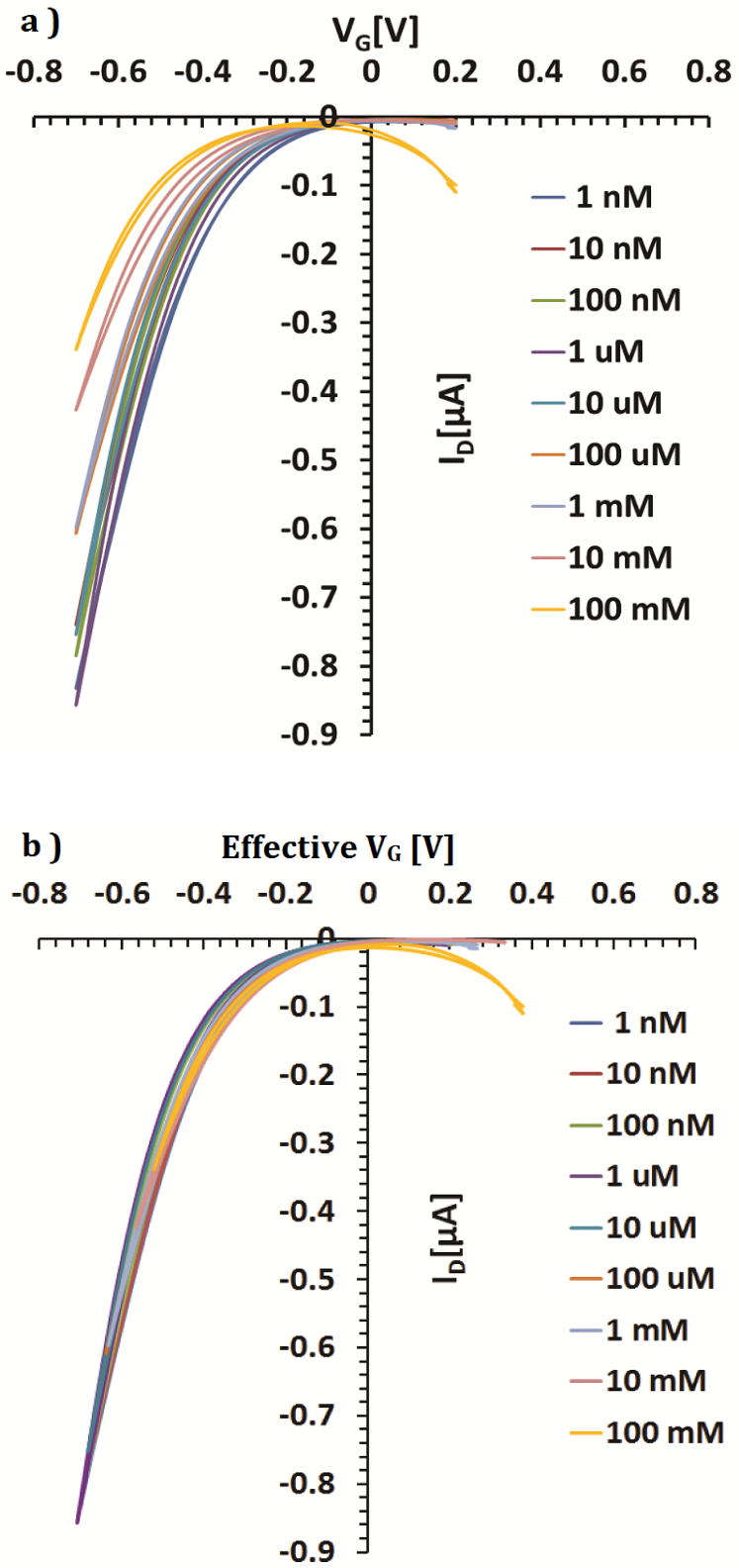

Figure 7.3 (a): *Transfer Characteristics of water- gated rrP3HT TFTs contacted by an Au gate needle sensitised with DB30C10 ionophore embedded in a plasticised PVC membrane. Gating is with water with different concentrations of sodium (Na^+, from NaCl), i.e. an interferant, increasing from 1nM ... 100mM in factors of 10.* ***(b):*** *Transfer characteristic 'master curve' constructed by shifting characteristics along the gate voltage axis to give the best possible overlap with the characteristic under lowest (1nM) Na^+ concentration.*

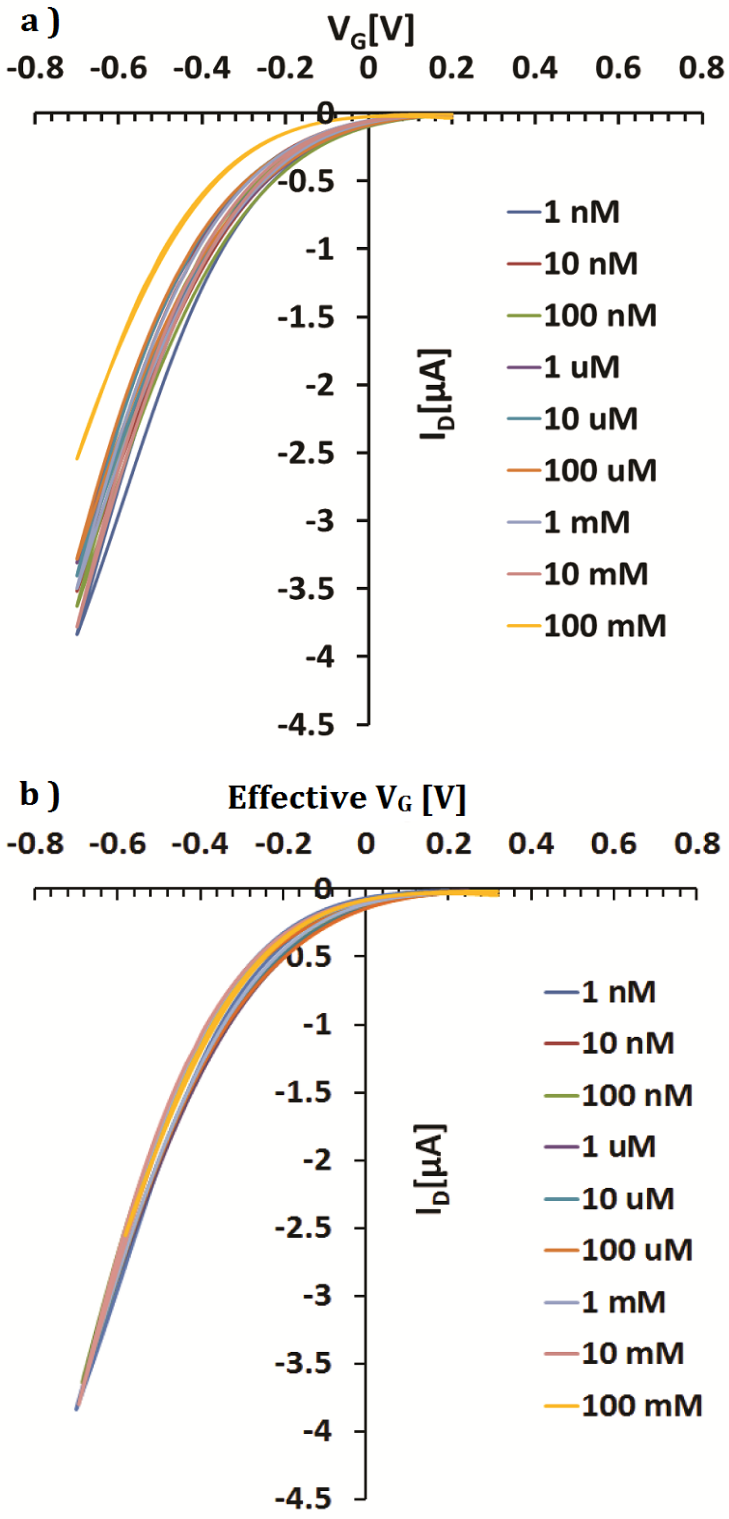

Figure 7.4 (a): *Transfer Characteristics of water- gated rrP3HT TFTs contacted by an unsensitised Au gate needle as a control experiment. Gating is with water with different concentrations of potassium (K^+, from KCl), increasing from 1nM ... 100 mM in factors of 10.* ***(b):*** *Transfer characteristic 'master curve' constructed by shifting characteristics along the gate voltage axis to give best possible overlap with the characteristic under lowest (1nM) K^+ concentration.*

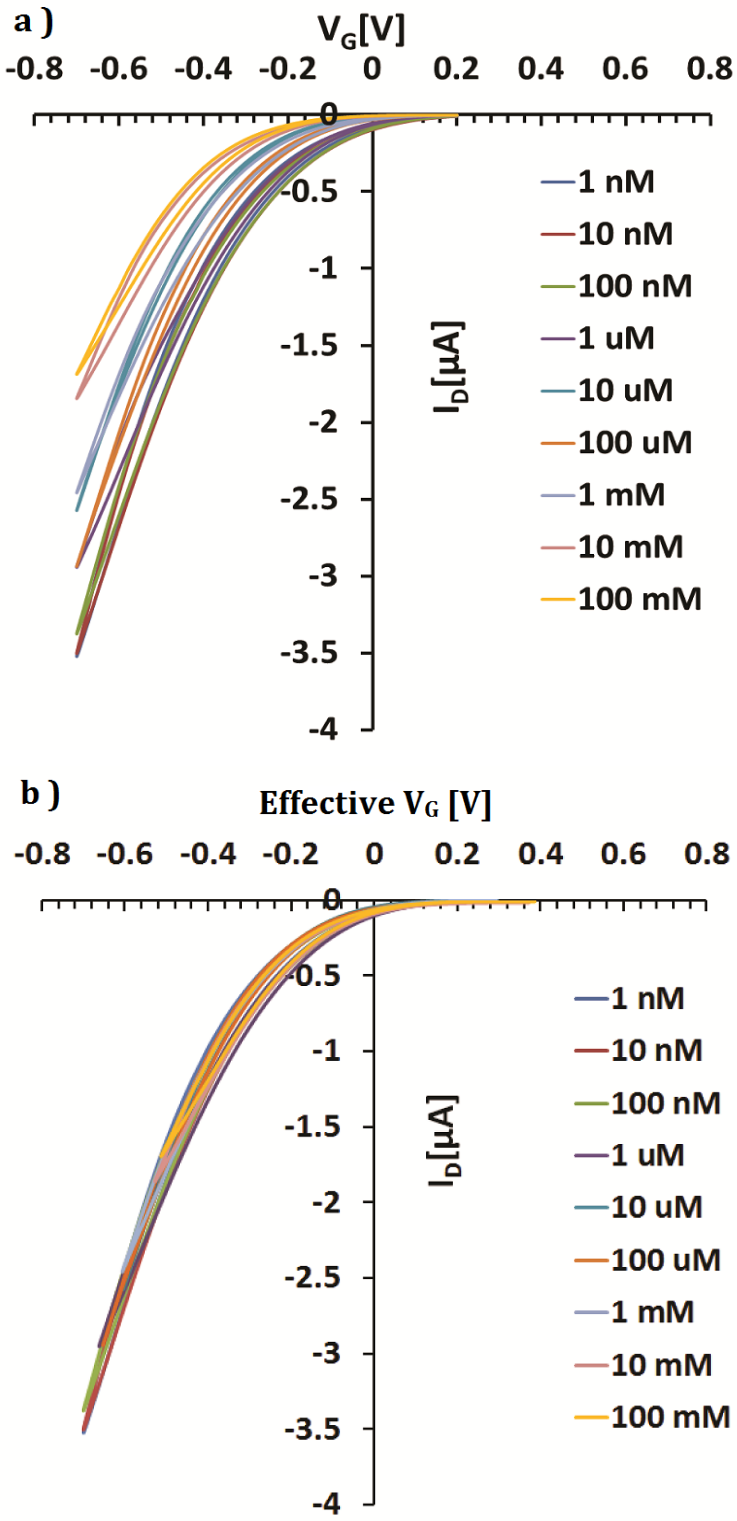

Figure 7.5 (a): *Transfer Characteristics of water- gated rrP3HT TFTs contacted by an unsensitised Au gate needle as a control experiment. Gating is with water with different concentrations of sodium (Na^+, from NaCl), increasing from 1nM .. 100 mM in factors of 10.* ***(b):*** *Transfer characteristic 'master curve' constructed by shifting characteristics along the gate voltage axis to give best possible overlap with the characteristic under lowest (1nM) Na^+ concentration.*

Figures 7.6 to 7.9 show the corresponding set of experiments using spray pyrolysed and HMDS- treated ZnO rather than rrP3HT as semiconductor: Figure 7.6, sensitised ZnO

transistor under K^+, Figure 7.7: sensitised ZnO WGTFT under Na^+ 'interferant', Figure 7.8 and 7.9 non- sensitised ZnO WGTFT.

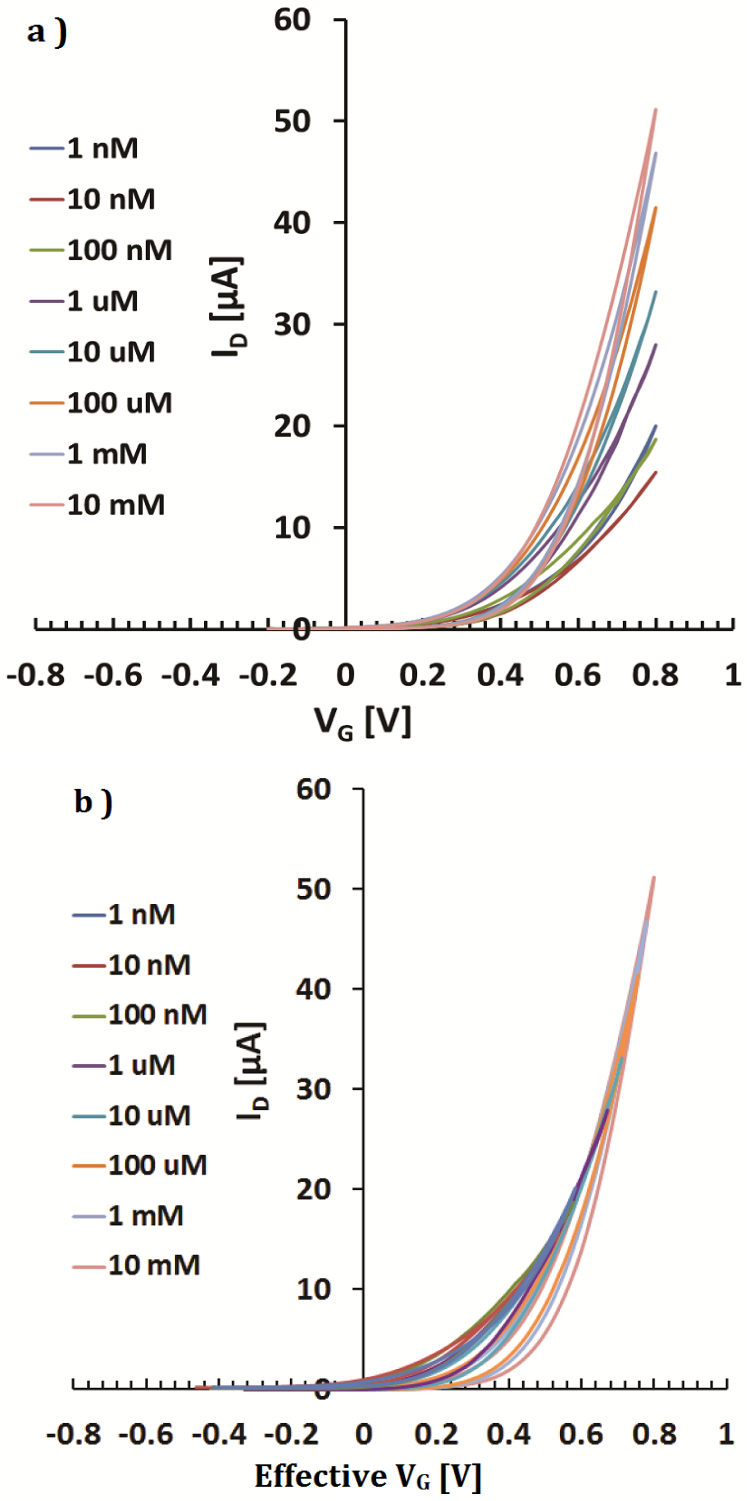

Figure 7.6 (a): *Transfer Characteristics of water- gated HMDS- treated ZnO TFTs contacted by an Au gate needle sensitised with DB30C10 ionophore embedded in a plasticised PVC membrane. Gating is with water with different concentrations of potassium (K^+, from KCl), increasing from 1nM ... 10 mM in factors of 10.* ***(b):*** *Same transfer characteristics as in 2a but shifted along the gate voltage axis for best overlap with the [K^+] = 1 nM characteristic. Characteristics were matched at the 'rising' flank, i.e. when sweeping gate voltage from near zero to large positive values.*

Now transfer characteristics are typical of electron- transporting TFTs: Once the gate voltage is more positive than a threshold, the TFT delivers a positive drain current of increasing magnitude as the gate voltage is made increasingly positive. Figure 7.6a shows threshold shifts in the same direction as for rrP3HT TFTs. However, this now means threshold becomes less positive with increasing K^+ concentration, shifting towards zero from an initially larger positive threshold rather than away from zero from an initially smaller negative value for rrP3HT WGTFTs. Also, the shift is now smaller in magnitude, and hysteresis is significant in particular for high ion concentration. We again constructed a 'master curve' (Figure7.6b) by shifting along the gate voltage axis. Characteristics were again matched at the 'rising' flank, which now is observed when sweeping gate voltage from near zero to large positive voltage as ZnO is an electron transporter. On the rising flanks, the different transfer characteristics again overlap well into a single master curve, the apparent mismatch of some characteristics is due to hysteresis on the 'falling' flank, sweeping gate voltage back towards zero. The required shift $\Delta V_T(c)$ is shown and analysed in context in Figure 7.11 and Table 7-1 below. Figures 7.7, 7.8 and 7.9 show three control experiments on ZnO WGTFTs. The response of DB30C10- sensitised ZnO WGTFTs to sodium instead of potassium in the gating water is shown in Figure 7.7. Figure 7.8 and 7.9 show the response of ZnO WGTFT to K^+ and Na^+ respectively when the gate contact was not sensitised. Corresponding $\Delta V_T(c)$ are also shown and analysed in context in Figure 7.11 and Table 7-1 below.

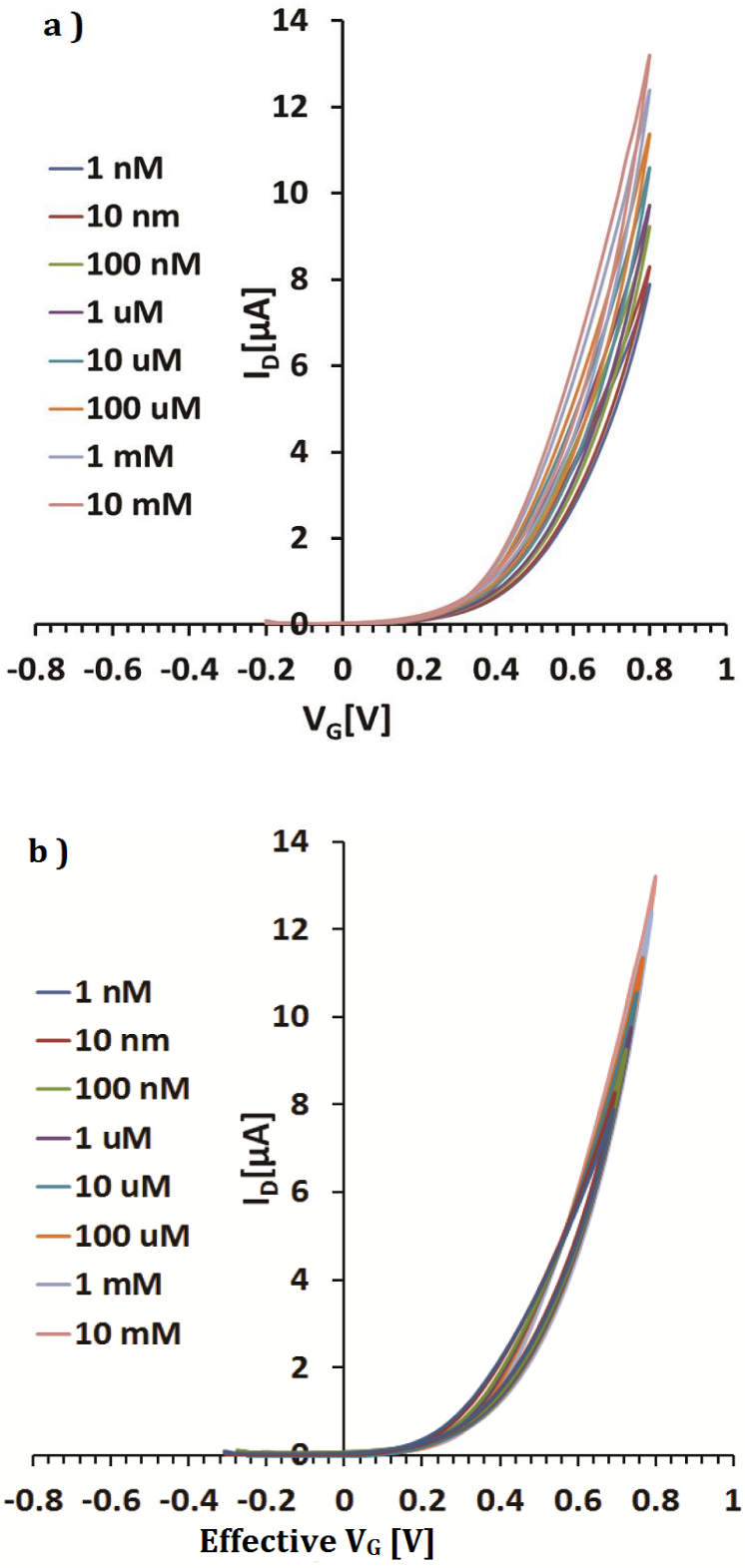

Figure 7.7 (a): *Transfer Characteristics of water- gated HMDS- treated ZnO TFTs contacted by an Au gate needle sensitised with DB30C10 ionophore embedded in a plasticised PVC membrane. Gating is with water with different concentrations of sodium (Na^+, from NaCl), i.e. an interferant, increasing from 1nM ... 10 mM in factors of 10.* ***(b):*** *Same transfer characteristics as in 6a but shifted along the gate voltage axis for best overlap with the [Na^+] = 1nM characteristic. Characteristics were matched at the 'rising' flank, i.e. when sweeping gate voltage from zero to positive values.*

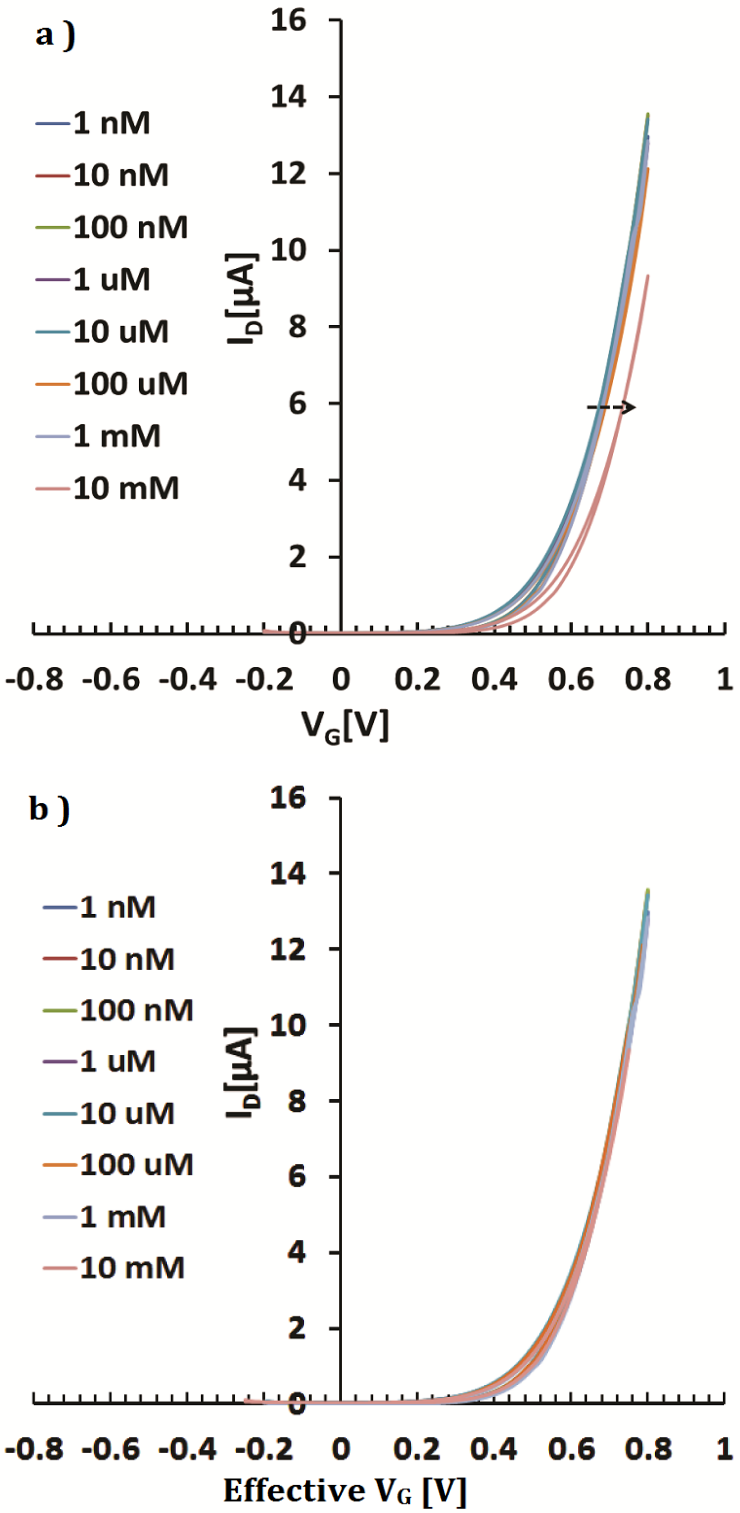

Figure 7.8 (a): *Transfer Characteristics of water- gated HMDS-treated ZnO TFTs contacted by an unsensitised Au gate needle as a control experiment. Gating is with water with different concentrations of potassium (K^+, from KCl), increasing from 1nM ... 10 mM in factors of 10.* ***(b):*** *Transfer characteristic 'master curve' constructed by shifting characteristics along the gate voltage axis to give best possible overlap with the characteristic under lowest (1nM) K^+ concentration.*

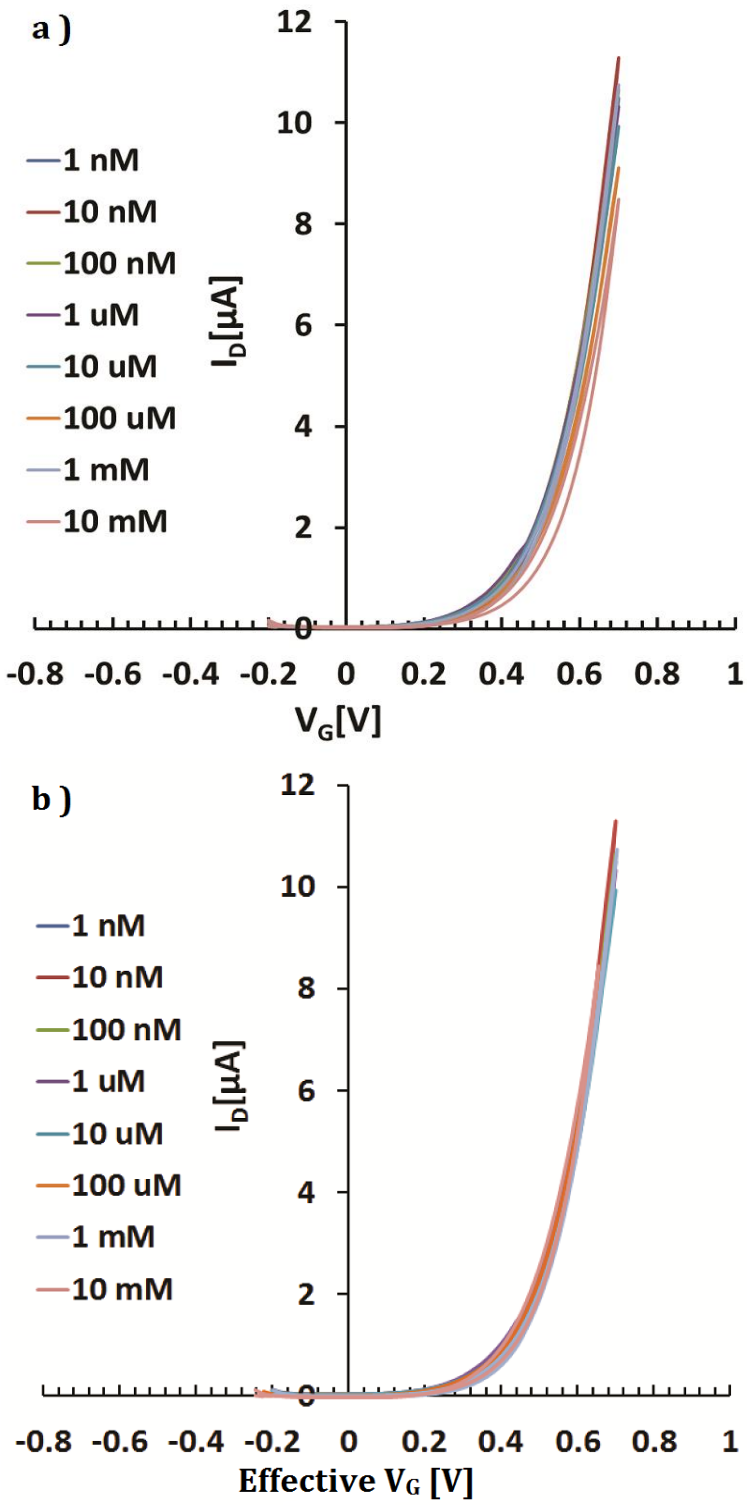

Figure 7.9 (a): *Transfer Characteristics of water- gated HMDS-treated ZnO TFTs contacted by an unsensitised Au gate needle as a control experiment. Gating is with water with different concentrations of sodium (Na^+, from NaCl), increasing from 1nM ... 10 mM in factors of 10.* ***(b):*** *Transfer characteristic 'master curve' constructed by shifting characteristics along the gate voltage axis to give best possible overlap with the characteristic under lowest (1nM) Na^+ concentration.*

Charge carrier mobility in the studied WGTFTs can be extracted from the linear transfer characteristic 'master curves', Figures 7.2b, 7.3b, 7.6b and 7.7b. Simple TFT theory relates charge carrier mobility, μ, to the (linear) transconductance (g_m)via Eq. 7-1:

$$g_m = W/L\ \mu C_i V_D \qquad 7\text{-}1$$

Wherein linear transconductance is defined as the slope of the linear transfer characteristic ($|V_D| << |V_G - V_T|$), $g_m = \partial I_D/\partial V_G$. C_i is the capacitance of the gate medium and W/L = 33.3 for our TFT substrates. We fitted straight lines in the high gate voltage regimes (V_G > 500 mV) of our master curves to find g_m and estimate the specific capacitance of the aqueous gate medium as 3 μF/cm^2 [33]. Eq. 7-1 then allows calculation of carrier mobilities; results are summarised in table 7-1. We find higher mobilities in ZnO than in rrP3HT; our results overlap with previous reports of mobilities in water- gated rrP3HT [84, 201] and precursor-route ZnO TFTs [51, 57, 120].

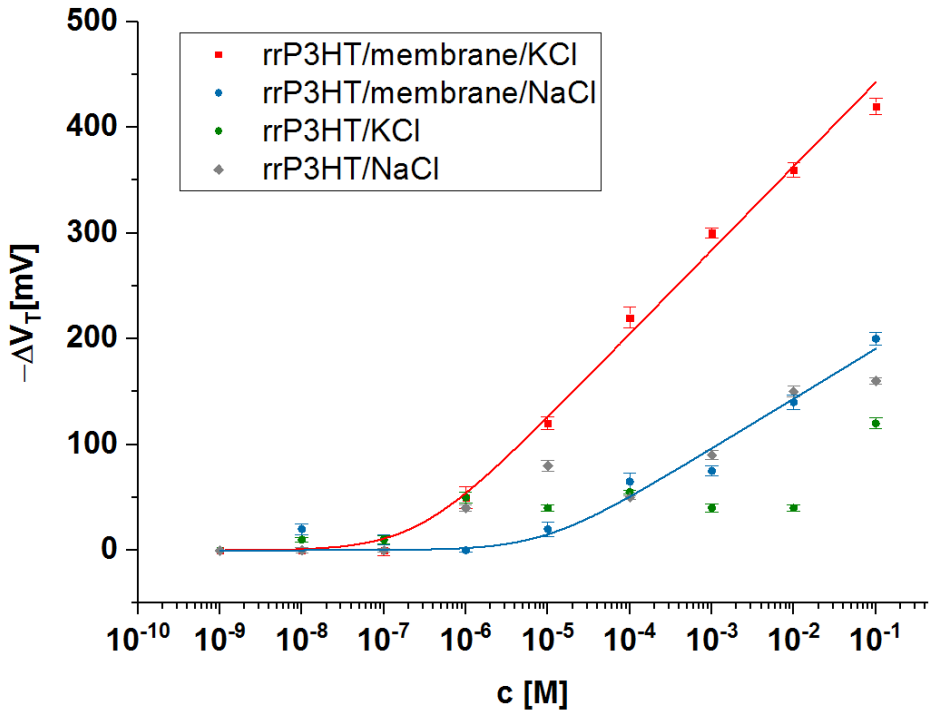

Figure 7.10 *Threshold shifts $\Delta V_T(c)$ under increasing concentration c of potassium or sodium in the gating water for rrP3HT WGTFTs sensitised with DB30C10/PVC membranes: red squares, potassium (from KCl); blue circles: Sodium (from NaCl). Solid lines are fits to Eq. 7-2; fit parameters are summarised in table 7-1. Also shown, response without ion- sensitive membrane: green circle, potassium (from KCl); grey squares: Sodium (from NaCl).*

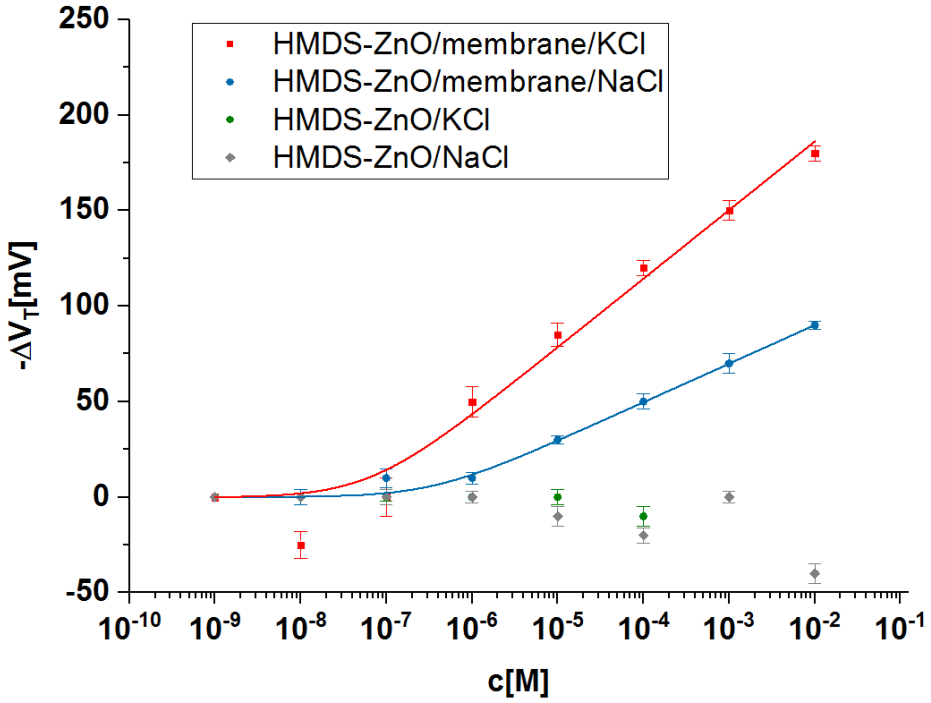

Figure 7.11 *Threshold shifts $\Delta V_T(c)$ under increasing concentration c of potassium or sodium in the gating water for ZnO WGTFTs sensitised with DB30C10/PVC membranes: red squares, potassium (from KCl); blue circles: Sodium (from NaCl). Solid lines are fits to Eq. 7-2; fit parameters are summarised in table 1. Also shown, response without ion- sensitive membrane: green circles, potassium (from KCl); grey squares: Sodium (from NaCl).*

Threshold shift $\Delta V_T(c)$ in ion- sensitive WGTFTs is rationalised as the result of an ion concentration-dependent membrane potential, $V_M(c)$[15, 17], which is effectively added to the gate contact's work function, and hence to TFT threshold voltage. For quantitative analysis, the $\Delta V_T(c)$ required to construct the master curves in Figures 7.2b, 7.3b, 7.4b, 7.5b, 7.6b, 7.7b, 7.8b and 7.9b are plotted vs. a logarithmic concentration scale in Figures 7.10 and 7.11 respectively. Also included are $\Delta V_T(c)$ for non- sensitised WGTFTs. For quantitative analysis, we fitted $\Delta V_T(c)$ according to the Nikolsky- Eisenman equation that describes ion concentration dependency of membrane potentials[152],

$$-\Delta V_T(c) = V_0 + s \log (c + c_{st}) \qquad 7\text{-}2$$

We here neglect the distinction between concentration and activity. $V_0 = -s \log (1\ nM + c_{st})$ ensures $\Delta V_T(1\ nM) = 0$ as implied by the shift procedure. Eq. 7.2 has two free fit parameters, s and c_{st}. For $c >> c_{st}$, Eq. 7-2 agrees with the generic Nernst equation (e.g.[15]). s is a slope (in mV / decade) that quantifies sensitivity; according to Nernst s = 58/z mV/dec (at ambient

temperature, wherein z is the ion's valency, z = 1 for K^+ and Na^+ [e.g.[15]). c_{st} sets a limit of detection (LoD), $c_{st} \approx$ LoD. The s and c_{st} we find from fitting data in Figures 7.10 and 7.11 are summarised in table 7-1, together with contact angles and carrier mobilities.

Table 7-1

Semiconductor	Contact angle [°]	Ion	μ [cm²/Vs]	c_{st} [nM]	s [mV/dec]
rrP3HT	102	K^+	0.45 (h^+)	160 ± 72	77 ± 3
rrP3HT	102	Na^+	0.45 (h^+)	9060 ± 9090	47 ±7
HMDS-ZnO	86.5	K^+	15(e^-)	65 ± 57	36 ± 4
HMDS-ZnO	86.5	Na^+	6.25(e^-)	313 ±131	19 ±1

Table 7.1 *contact angles, carrier mobilities, and the fit parameters to $\Delta V_T(c)$ according to eq.7-2, for the different WGTFTs studied here. Fit parameters evaluated by the Origin nonlinear fit routine.*

According to Nikolsky-Eisenman theory, the selectivity of an ionophore for an analyte- over an interferant ion is quantified by the ratio of their c_{st}, while slope s above c_{st} should match the Nernstian value s = 58/z mV/dec. However, it is known from many experimental studies, including WGTFTs and potentiometric transducers, that slope s under interferant often is lower than for analyte ion even above c_{st} [e.g.[15, 17, 18].

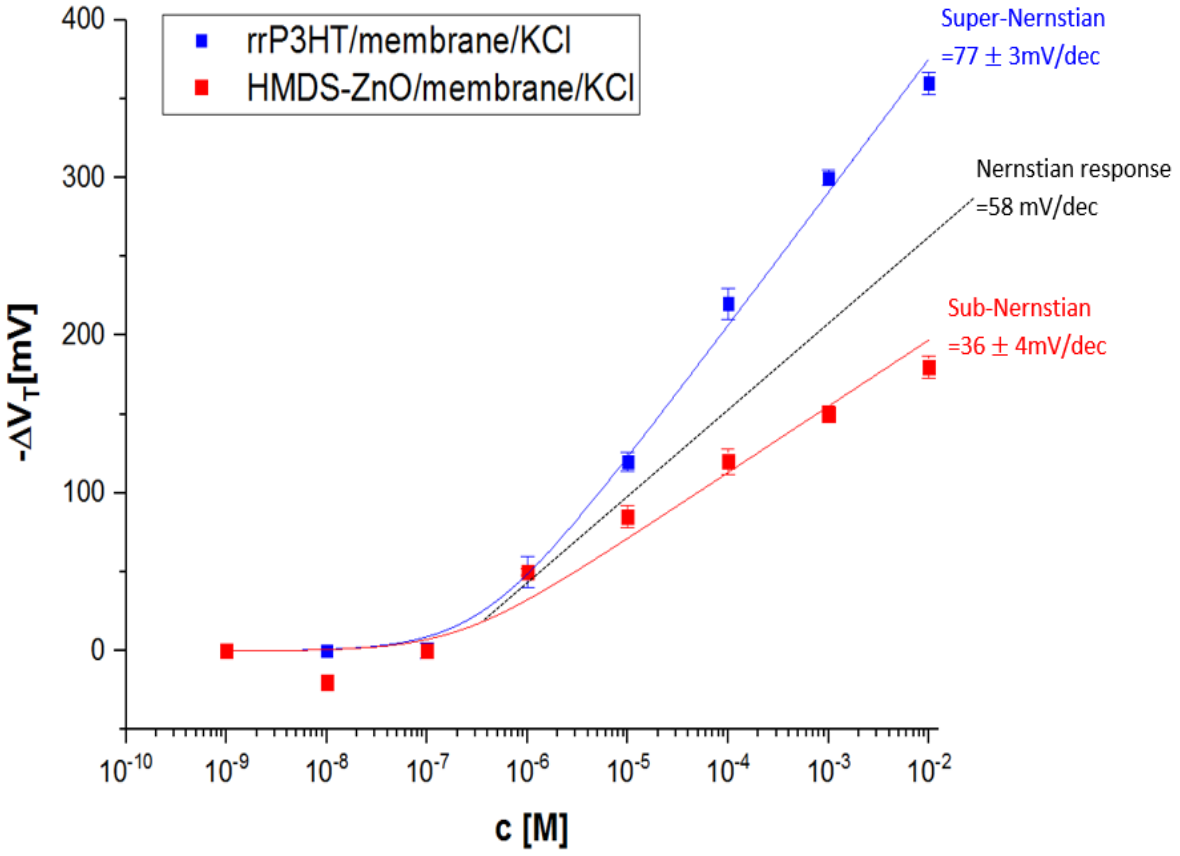

Figure 7.12 *Comparison between threshold shifts $\Delta V_T(c)$ under increasing concentration c of potassium in the gating water for rrP3HT and HMDS-ZnO WGTFTs sensitised with DB30C10/PVC membranes: rrP3HT shows super-Nernstian= 77± 3mV/dec, whereas HMDS-ZnO shows sub-Nernstian= 36 ±4mV/dec .The black dashed line shows the Nernstian response for a single ion= 58 mV/dec.*

As we always used the same DB30C10- sensitised PVC membrane on the WGTFT's gate contact, membrane potential $V_M(c)$ is expected to be the same for all WGTFTs tested here. Yet remarkably, we find the observed $\Delta V_T(c)$ are not equal: Hole- transporting rrP3HT WGTFTs display a 'super- Nernstian' potassium sensitivity of s = 77 ± 3 mV/dec, while we find only s = 36 ± 4 mV/dec for electron- transporting ZnO TFTs as shown in Figure 7.12. We note that a WGTFT is gated across a series of two electric double layer (EDL) capacitors: For a hole transporting WGTFT, a cationic EDL forms at the gate electrode/water interface in series with an anionic EDL at the water/semiconductor interface. For an electron transporting WGTFT, the EDL sequence is reversed. Apparently, the EDL sequence for gating ZnO leads to larger hysteresis (compare Figure 7.2b to 7.6b), which in itself warrants further investigation, but as threshold shift was evaluated from matching at the 'rising' flanks only, hysteresis cannot account for super- *vs* sub- Nernstian sensitivity. However, we expect the

cationic EDL to display higher capacitance than the anionic EDL due to the smaller size of cations. As both EDLs carry the same charge, the lower capacitance (anionic) EDL must therefore display a higher potential difference across it. As it is the anionic EDL that gates the hole- transporting semiconductor, we believe this leads to a sensitivity amplification for hole transporting WGTFTs according to the EDL capacitance ratio as described in Eq. 7-3. A similar capacitive amplification was achieved by Spijkman et *al.* [202] in a dual- gate architecture, albeit not in a water- gated TFT. For an electron transporting WGTFT, the EDL sequence is reversed as described in Eq. 7-4, leading to sub- Nernstian response in our ZnO WGTFTs. Previous reports are consistent with the above, albeit they have not been explained in those terms by their authors: Melzer et *al.* [17]report sub- Nernstian s = 39.3 ± 1.6 mV/dec for sensing potassium using electron transporting carbon nanotubes, while Althagafi *et al.*[190] found super- Nernstian response (55 mV/dec for Ca^{2+}, here z = 2 hence Nernstian slope would be only 29 mV/dec) using hole transporting polymer poly(2,5-bis(3-hexadecylthiophen-2-yl)thieno[3,2-b]thiophene) (PBTTT). Note that in the original report on an ion- sensitive WGTFT by List- Kratochvil et *al.*[15], the authors used a two-chamber system separated by the ion-sensitive membrane, rather than preparing it on the gate electrode. This leads to a serial combination of 4 (not 2) EDLs in alternating order, cancelling amplification.

$$\Delta V_{channel} = \Delta V_{membrane} x \frac{C_{cationic}}{C_{anionic}} \quad \text{For hole transporter} \qquad 7\text{-}3$$

$$\Delta V_{channel} = \Delta V_{membrane} x \frac{C_{anionic}}{C_{cationic}} \quad \text{For electron transporter} \qquad 7\text{-}4$$

Both DB30C10- sensitised rrP3HT and ZnO WGTFTs also respond to the 'interferant' Na^+ albeit with higher LoD, and almost halved slope even above LoD, compared to the primary analyte, K^+. This reflects the (limited) selectivity of the DB30C10 ionophore [197] but is not a feature of the chosen device architecture or semiconductor.

While the above discussion suggests rrP3HT as the preferred semiconductor for ion sensing with WGTFTs (lower hysteresis, super- Nernstian response), Figure. 7.10 reveals that unfortunately, even unsensitised rrP3HT WGTFTs display some response to increasing K^+ and Na^+ concentration, simply due to increasing ionic strength of the gating solution. It is known that organic semiconductor films have some permeability to ions [58, 148]which we

believe leads to the observed threshold shift under increasing ion concentration, even in the absence of a selective membrane, particularly for the smaller Na^+ ions. Unspecific threshold shift due to increasing ionic strength can be avoided by using two- chamber architecture as by List-Kratochvil et *al.*[15], but at the expense of more complicated device architecture, and the loss of capacitive sensitivity enhancement.

Alternatively, we can use ZnO as a semiconductor, which apparently is impermeable to ions. Figure 7.11 shows that for unsensitised ZnO WGTFTs, increasing ionic strength only leads to small threshold shift at very high ion concentrations, and with an opposite sign as for sensitised WGTFTs, which allows for clear distinction from membrane- induced threshold shift. While ZnO has the added (minor) advantage of higher carrier mobility, hence higher TFT currents, this comes at the expense of higher hysteresis, and a reversal of the favourable capacitive sensitivity enhancement found for p-type semiconductors.

7.4 Conclusion

We compare ion- sensitive water- gated (WG) electric double layer (EDL) thin film transistors (TFTs) using p-type (organic) vs n-type (inorganic) solution-processed semiconductors. Both types of WGTFTs were sensitised at the gate contact with PVC membranes containing the potassium- selective ionophore DB30C10. DB30C10 has been investigated previously in conventional potentiometric ion sensors [197], but not yet in WGTFTs. When using the organic polymer hole transporter rrP3HT as semiconductor, we observe TFT transfer characteristics with little hysteresis, and super- Nernstian potassium sensitivity of 77 ± 3 mV/decade. We explain super- Nernstian response as capacitive amplification by the ratio of cationic/anionic EDL capacitance. However, control experiments reveal a weaker, non- selective ion response of rrP3HT itself, in the absence of an ion-sensitive membrane. This compromises ion selectivity. To retain selectivity, a two- chamber design would be required that avoids direct contact between semiconductor and analyte solution[15]. However, this adds significant complexity to device manufacture and loses the super- Nernstian response.

By contrast, WGTFTs using the electron- transporting inorganic II-VI semiconductor Zinc oxide (ZnO) sprayed from soluble precursor display higher mobility, stronger hysteresis, and

sub- Nernstian response when sensitised with DB30C10 membranes. Sub- Nernstian response has been observed previously for n-type ion selective WGTFTs [17], we explain this by the now reversed sequence of cationic/anionic EDLs. However, other than rrP3HT, unsensitised ZnO WGTFTs are less responsive to ionic strength in the gating water. This retains the membrane's ion selectivity without the need for two-chamber device design.

Hence, both organic p-type, and inorganic n-type solution-processed semiconductors have their relative merits, and drawbacks, for use in ion-selective WGTFTs.

Chapter 8: Electrochemical gating of a hydrophobic organic semiconductor with aqueous media

8.1 Introduction

Electrolyte-gated (particularly, water-gated) organic thin film transistors (EG/WG OTFTs) have been the subject of intense research recently [e.g.[15, 17, 45, 58, 84, 148, 190]. This interest is driven by their potential applications, *e.g.* as sensors for waterborne analytes, and in bioelectronics. WG OTFTs can, in principle, operate in two modes, namely an organic field effect transistor (OFET) mode, or an organic electrochemical transistor (OECT) mode[146, 147]. In the OFET mode, a gate voltage applied across the electrolyte leads to interfacial electric double layers (EDLs) at the gate/water interface, and the water/semiconductor interface. The latter consists of an excess of one type of ions in the water, and an opposing charge carrier accumulation layer at the semiconductor surface. In principle, this can be anions *vs* holes or cations *vs* electrons. However, practical WG OFETs usually are hole transporting. A negative gate voltage, when exceeding a transistor-specific threshold, will generate hole accumulation and conductivity in the transistor channel: WG OFETs work in accumulation mode. Transconductance is proportional to the EDL capacitance, C_i, (≈ 3 $\mu F/cm^2$ for water gating[33]) but independent of semiconductor film thickness, d. In contrast, in OECT mode, the gate voltage does not lead to an interfacial EDL but drives ions across the electrolyte/semiconductor interface into the bulk of the semiconductor. OECT mode operation is further divided into 'depletion mode' and 'accumulation mode'. In accumulation mode, ions dope a previously undoped semiconductor channel; in the depletion mode, ions de- dope a previously doped channel [148, 149]. As we now have bulk- rather than interfacial transport, transconductance is proportional to dC*, where C* is a capacitance per unit volume, and d the thickness of the semiconductor film. A 130 nm film of the synthetic metal PEDOT: PSS displays $dC^* \approx 500$ $\mu F/cm^2$ [150], two orders of magnitude larger than C_i in field- effect mode, leading to correspondingly larger 'on' currents. This also gives a simple experimental criterion to distinguish OFET from OECT operation, namely that OFET current is smaller and independent of semiconductor film thickness, d, while OECT current is larger, and increases with d.

If a WG TFT operates in OFET- or OECT mode, it is usually controlled by the hydrophobicity or hydrophilicity of the respective organic semiconductor. Among the

commonly used thiophene-based organic hole transporters, polymers with thiophene or thiophene-thieno-thiophene conjugated backbones[203] and aliphatic sidechains (e.g. regioregular poly(3-hexithiophene) (rrP3HT) or poly[2,5-bis(3-tetradecylthiophen-2-yl) thieno[3,2-*b*]thiophene] (PBTTT)) typically lead to field-effect operation [15, 33, 190, 204]due to their hydrophobic nature: the water contact angle with PBTTT and rrP3HT is 107° [205]. However, when the polymer backbone consists of thiophenes carrying more hydrophilic ether crowns (e.g. in PEDOT:PSS [150]), or of a thiophene-thieno-thiophene backbone with hydrophilic side chains, (e.g. in poly(2-(3,3′-bis(2-(2-(2-methoxyethoxy)ethoxy)ethoxy)-[2,2'-bithiophen]-5-yl) thieno [3,2-b]thiophene), p(g2T-TT)) [206], OECT mode is observed (depletion mode for PEDOT:PSS, accumulation mode for p(g2T-TT). However, the distinction between OFET and OECT mode is somewhat fluid and may be crossed. For example,poly(2-(3,3′-bis(tetradecyloxy)-[2,2'-bithiophen]-5-yl) thieno[3,2-b]thiophene), p(a2T-TT) acts in field-effect mode at low gate voltages and shows OECT mode at high gate voltages [206], and Giridharagopal *et al* report some penetration of chloride ions into bulk even for the hydrophobic rrP3HT [200] under high ion concentrations (~100 mM). However, the highly crystalline and hydrophobic semiconducting polymer PBTTT has so far not been found to operate in OECT mode when gated with aqueous media, not even under (100...200) mM chloride electrolytes [190, 205]. PBTTT OECT operation has been seen previously only when gated with solid electrolyte, PEO: LiClO3, but with a threshold outside the 1.23 V electrochemical window of water [207].

Here, we report that even PBTTT can work in OECT mode when gated with aqueous media, without the 'sidechain engineering' (hydrophilic *vs* alkane side chains) shown by Giovannitti *et al.* [206]. This is achieved by choice of anion in the gating water, namely the water-soluble explosive, picric acid (PA), at high concentrations (≈ 50 mM or more, see below). PA partially dissociates and dissolves when in contact with water. Otherwise, it is somewhat similar to the few known solvents for PBTTT: PA consists of an electron deficient π electron system due to the substitution of a phenol ring with 3 electron withdrawing nitro groups (inset Figure. 8.1). PBTTT solvents are di- and tri-chlorinated benzene (DCB / TCB). We show that PA's combination of properties - solubility in water, and similarity to PBTTT solvents - leads to OECT behaviour in PBTTT which has previously shown OFET behaviour only when gated with aqueous media.

8.2 Experimental details

8.2.1 Materials: Poly (2,5-bis(3-tetradecylthiophen-2-yl) thieno[3,2-b]thiophene) (PBTTT-C16) was sourced from Ossila Ltd (Cat. No. M141 PBTTT-C16), regioregular poly(3-hexylthiophene) was purchased from Aldrich (Cat. No. 698989, average M_n 15,000-45,000), and 0.9 -1.1% (alkalimetric) Picric Acid (2,4,6-Trinitrophenol) solution was sourced from Sigma Aldrich (Cat. No. 36011).

8.2.2 Sample preparation:

In chapter 4, I have described the preparation and fabrication of TFT used in my experiments. However, briefly, transistor substrates consist of silica-coated glass substrates with shadow-mask evaporated 100 nm Au on 10 nm Cr adhesion layer contact pairs of width W = 1 mm separated by a gap ('channel') of L = 30 μm, W/L = 33.3. PBTTT was dissolved in 1, 2-dichlorobenzene (DCB) at 7 mg/ml or 10 mg/mL respectively, and spin coated onto contact substrates from hot (100 ^{o}C) DCB for 40 seconds at 5000 rpm or 2500 rpm for thicker films. After casting, films were dried under dynamic vacuum at 110 ^{o}C for 40 minutes. Film thickness was determined with a Veeco Dektak XT surface contact profilometer as 17.6 nm for 5000 rpm and 27 nm for 2500 rpm. For rrP3HT films, we dissolved 10 mg/mL rrP3HT in DCB, heated at 80 °C for ≈10 min, and spin cast onto contact substrates at 2000 rpm for 60s. After casting, films were dried under dynamic vacuum at 110 °C for 40 min. Film thickness was 22 nm. The semicrystalline morphology of PBTTT and rrP3HT films have been studied in detail before, *e.g.* [140, 198]. Aqueous Picric Acid solution was sourced at concentration 4.4 M; a 100 mM stock solution was prepared by dilution with DI water. A Eutech Instruments CyberScan pH meter shows pH = 5.5 for 100 mM PA. The 100 mM PA solution was then further diluted in several steps down to 1μM.

8.2.3 Electrical characterisation

In section 5.2, I have described the technique used to measure TFT characteristic by Keithley 2400 source measure units. We applied 2 μL droplets of aqueous test solutions as gate media over the channel region of PBTTT and rrP3HT TFT substrates and electrically addressed by Au gate needles (American Probe and Technologies) bent into an L-shape and held at fixed distance (~ 100μm) from the semiconductor surface using a probehead. Then, we recorded output characteristic and transfer characteristics using two Keithley 2400 source- measure units and bespoke LabView software. We limited voltage sweeps to 1V rather than the full 'electrochemical window' of water of 1.23 V. The setup is shown schematically in Figure 8.1.

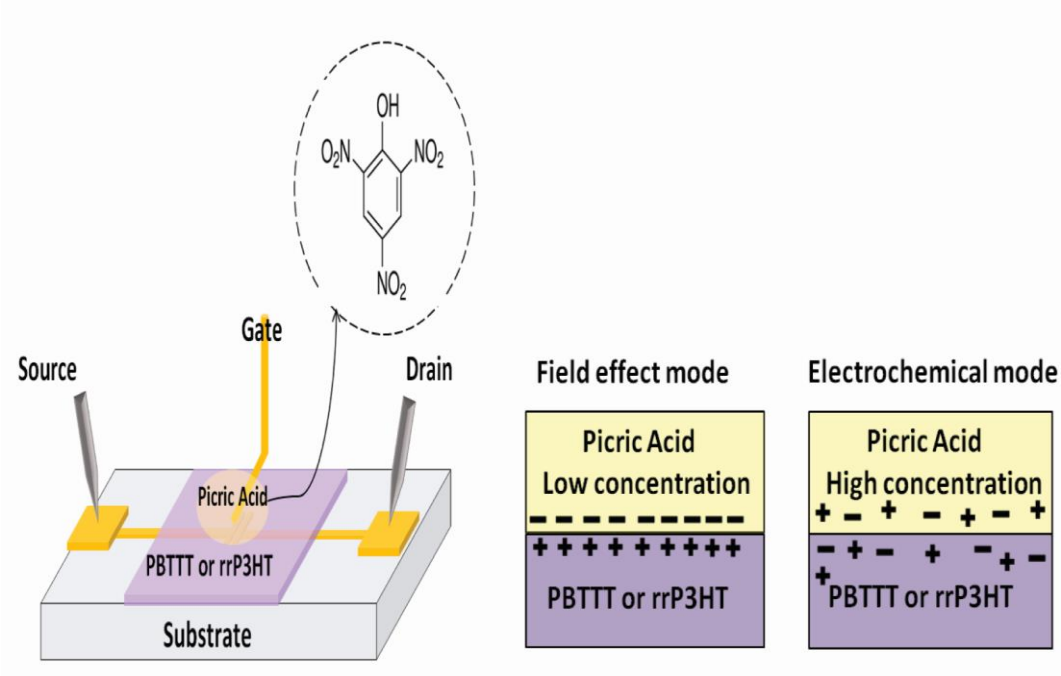

Figure 8.1 *TFTs gated by aqueous picric acid (PA) solutions.* ***Inset:*** *the structure of PA. Field effect (interfacial) and electrochemical (volumetric) transistor mode are illustrated schematically on the right.*

8.3 Results and Discussion

Figure 8.2 shows transistor output characteristics for PBTTT and rrP3HT transistors when gated either with DI water or 100 mM aqueous picric acid solutions. DI water-gated transistors display output characteristics with low threshold and some hysteresis, with maximum currents in the order of a few μA, similar to typical WG OFETs using thiophene-based polymers as semiconductors when we account for different geometry factors W/L (here, W/L = 33.3)[33, 208]. As expected, these devices behave as an electrolyte- gated field effect transistors. However, when we gate identically prepared films with an aqueous solution of 100 mM picric acid (PA), we now find significantly larger 'on' currents in the order mA, and also stronger hysteresis and dependency on film thickness. The highest observed current is approximately I_{MAX} = - 7 mA at $V_G = V_D$ = - 1V in Figure. 8.2 (b). This corresponds to a sheet resistance of $R_{\square}$ = 4.7 kΩ/□. As sheet resistance is related to conductivity σ by σ = $1/(R_{\square}d)$ with film thickness d, here d = 27 nm, this corresponds to a conductivity of σ ≈ 80 S/cm. This almost reaches the conductivity of commercial PEDOT: PSS synthetic metal products from Heraeus Holding GmbH (Hanau, Germany) for which the technical documentation currently shows conductivity 100 to 1000 S/cm. Such high currents and conductivities can only be understood by volumetric (OECT) gating rather than interfacial (OFET) operation. We note, however, that devices still clearly behave as transistors, not as

low resistance resistors, as would be the case for a highly doped semiconductor or synthetic metal: drain current strongly depends on gate voltage. The assignment of OFET vs OECT behaviour is supported by comparing results between transistors with two different PBTTT film thicknesses, 27 *vs* 17.6 nm. The DI water gated transistors show a virtually identical maximum current of ≈ 3.5 µA for both thicknesses, as expected for OFET mode operation, as field effect is limited to a thin interfacial accumulation layer. However, OECTs display bulk transport, and correspondingly, the maximum current is far bigger and increases with film thickness.

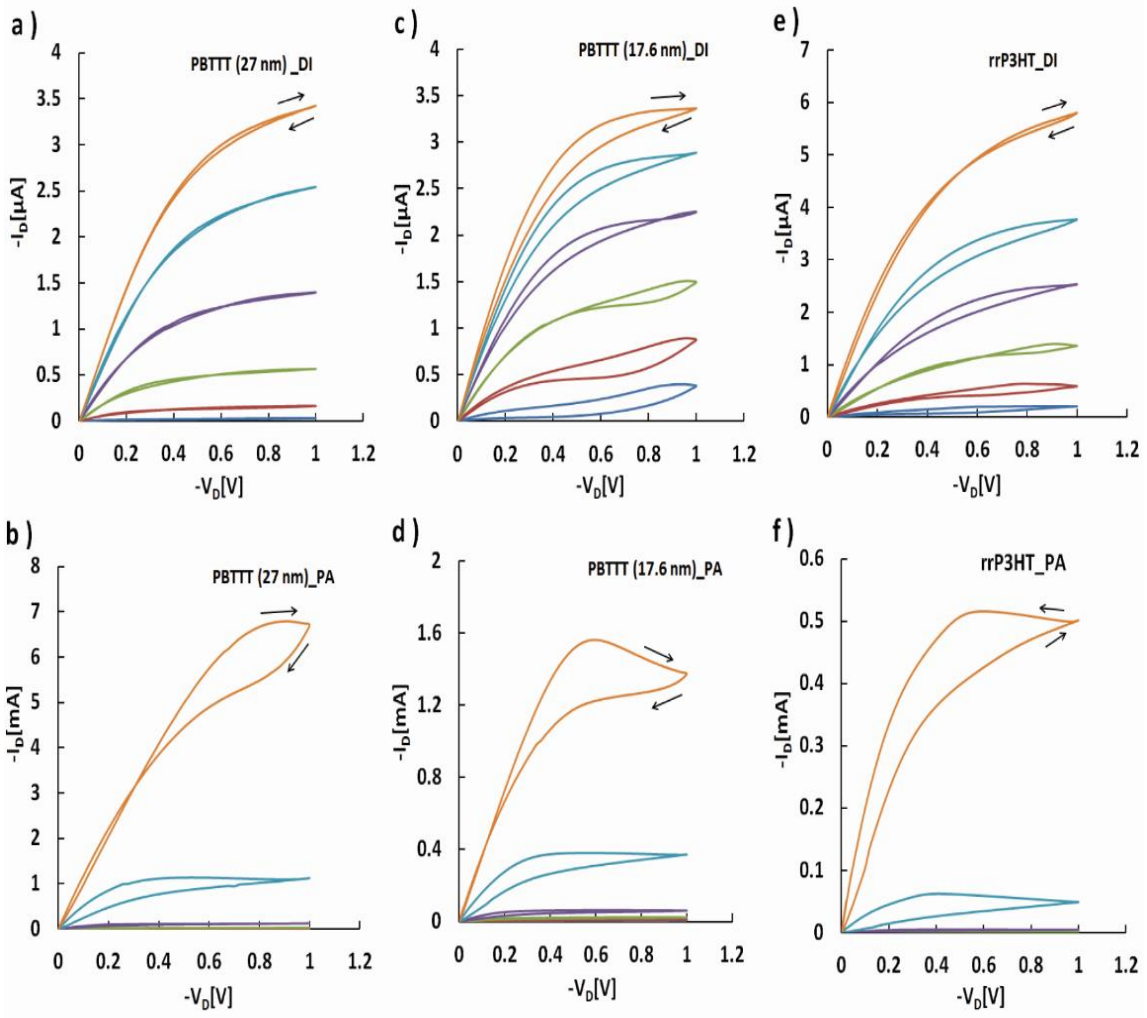

Figure 8.2 *Output characteristic for 27 nm PBTTT film gated by DI water* ***(a)*** *and 100 mM PA* ***(b);*** *17.6 nm PBTTT film gated by DI water* ***(c)*** *and 100 mM PA* ***(d);*** *and 22nm rrP3HT film gated with DI water* ***(e)*** *and 100 mM PA* ***(f).*** *Note the µA current scale in a,c,e vs mA current scale in b, d, e. Gate voltages from 0 to -1V in steps of 0.2V.*

We note that the transition from OFET- to OECT behaviour is specific to gating with PA^- anion, and is not found when PBTTT is gated with a simple anion (e.g. Cl^-), even at high

concentration and voltages: Porazzo *et al.*[205]. find no evidence of electrochemical gating mode for PBTTT under 200 mM NaCl up to V_G = - 1.2 V, V_D = -1 V, Figure 3 in [205].To confirm, we have repeated the above experiments three times on nominally identical devices. The resulting I_{MAX} are shown on a logarithmic scale in Figure 8.3.

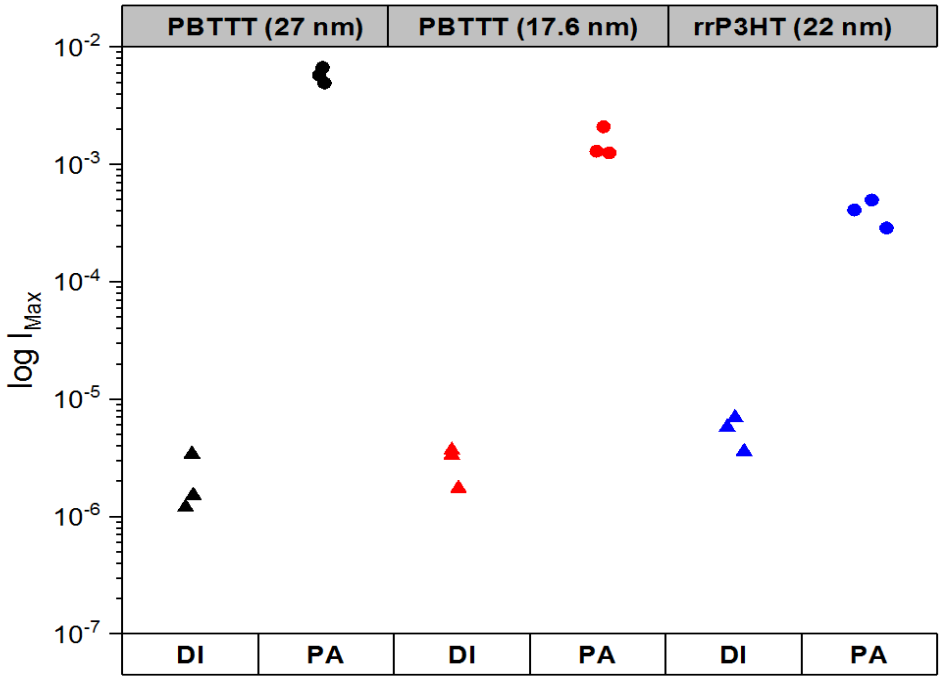

Figure 8.3 *Saturated drain current at V_G = -1V (I_{MAX}) from output characteristics of 3 nominally identical transistors each, comparing films of PBTTT (27 nm, black)), PBTTT (17.6 nm, red)) and rrP3HT (22 nm, blue) gated with either DI water (triangles) or 100 mM picric acid (PA, circles) solution in water. Note the logarithmic current scale.*

We find that in all cases, 100 mM PA gating leads to significantly higher drain current than DI water gating, more so for PBTTT than for rrP3HT. Also, thicker PBTTT films give higher currents than thinner PBTTT films. All these observations suggest that when gated with 100 mM PA, PBTTT and rrP3HT based thin film transistors operate in electrochemical (OECT) rather than field effect mode. Unlike, e.g. chloride ions [190, 205], PA anions apparently are able to penetrate the bulk of PBTTT films despite PBTTT's strongly hydrophobic character. We find, however, that this is only the case at sufficiently high concentrations of PA. Figure 8.4 shows saturated transistor drain currents (at V_G = -0.8 V) against PA concentration in water.

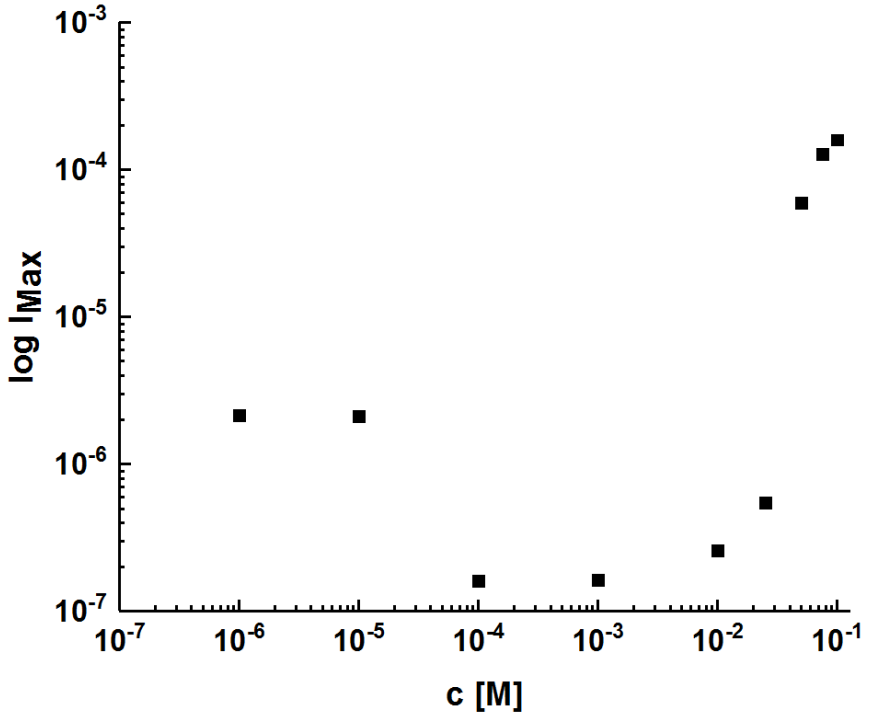

Figure 8.4 *Saturated drain current (I_{MAX}) at V_G = - 0.8 V on logarithmic scale vs PA concentration in gating water, also on a logarithmic scale.*

For PA concentrations c from zero up to 1mM, saturated drain current remains low, and in fact, somewhat decreases with increasing c. At low PA concentrations, the transistor still operates in field effect mode, *i.e.* gating is via an interfacial EDL. Therefore, the transition to electrochemical mode seen in Figure 8.2 requires higher PA concentrations. The linear transfer characteristics are shown in Figure 8.5 show lower mobility (slope) and larger threshold (V_G axis intercept) under 1 mM vs 1 μM PA. This is probably due to interactions between the electron-deficient π electron system of PA with PBTTT at the semiconductor/water EDL; such an effect is absent when the EDL forms with a 'simple' anion like chloride [190]. However, there is a rather sharp transition to far higher drain currents beginning at 10 mM PA concentrations, which is completed at c ≈ 50 mM. We assign this to the transition from field effect to electrochemical transistor mode under high PA concentrations. EDL gating requires only a single sheet of ions at the gate medium /semiconductor interface. Hence EDLs can build up even from gate media with minute ion concentrations [209]. In contrast, electrochemical gating requires bulk doping of the solid semiconducting film, hence far larger numbers of ions have to be supplied from the gate medium. A change in the level of water hydration may make this possible at higher

concentrations. Electrochemical gate media reported in the literature often have ion concentrations in the order 100 mM [149, 206]. In the case of PBTTT doped with PA, it seems c ≈ 50 mM of PA in the gate medium is needed to supply sufficient anions for electrochemical doping. We note, however, that the PA concentrations we report here are concentrations of PA molecules dissolved in water, not of dissociated anions, PA^-. Unlike simple salts, organic acids dissociate only partly in water, $PA + H_2O \leftrightharpoons PA^- + H_3O^+$. This is evident from pH measurements, we find pH ≈ 5.5 for 100 mM PA, full dissociation would lead to pH = - log (0.1) = 1; note pH = p (anion). The dissociation equilibrium is weighted towards the molecule (PA) rather than the anion (PA^-) by about 30,000: 1. The minimum concentration of PA^- anions required to affect electrochemical gating is therefore significantly lower than the quoted c ≈ 50 mM concentration of PA molecules.

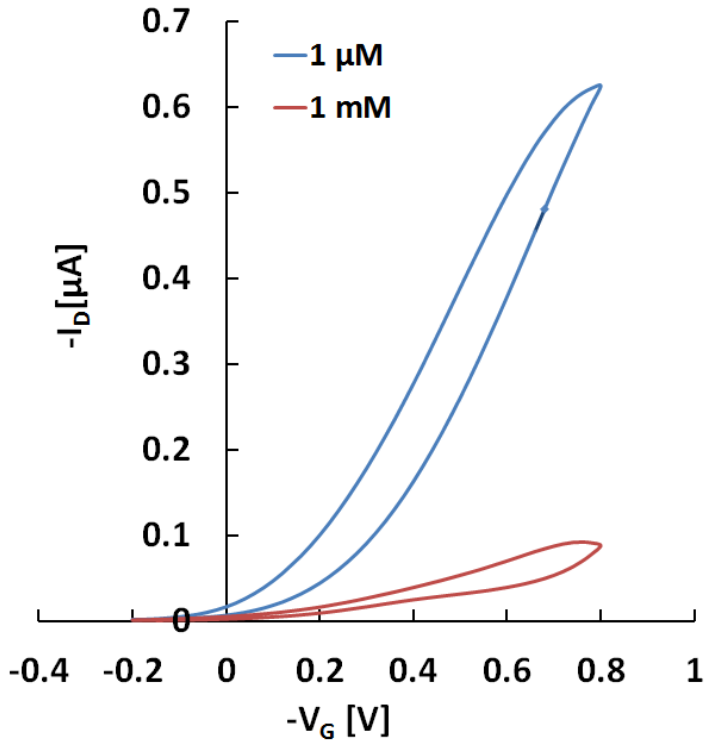

Figure 8.5 *Linear transfer characteristics (V_D = -0.1 V) for 1 µM (blue) and 1 mM (red) PA concentration.*

As a control experiment, we have gated a PBTTT film with another organic acid, acetic acid, at significantly higher concentration of 5% acetic acid ≈ 870 mM. Again, acetic acid dissociates only partially; - log (0.87) ≈ 0.1 but we measure pH = 2.6. Nevertheless, the concentration of acetic acid anions in the control experiment (pH 2.6) is far higher than concentration of PA^- anions in 100 mM PA solution (pH 5.5). Figure 8.6 shows output characteristics under 5% acetic acid gating:

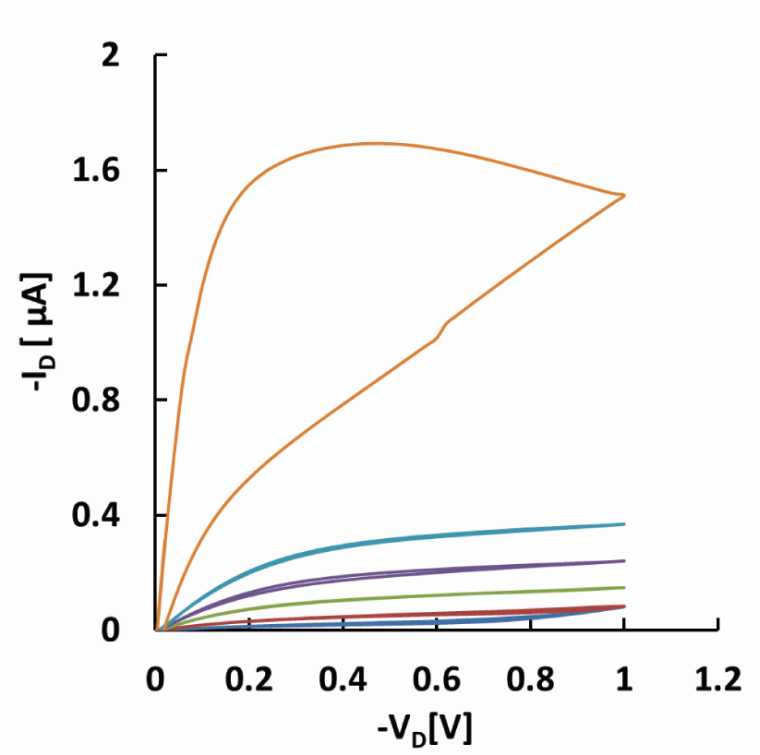

Figure 8.6 *Output characteristic of PBTTT under 5% acetic acid (commercial vinegar condiment, pH = 2.6).*

We find large hysteresis at high gate voltage, but currents remain in the µA range. The acetic acid anion does not lead to OECT operation, just like the chloride anion did not in previous reports [190, 205]. The bulk penetration into PBTTT that leads to OECT mode is specific to the PA^- anion and is not observed even for other organic acid anions. We believe that this is due to the similarity of the PA^- anion to PBTTT solvents (chlorinated benzenes), apart from the ionic *vs* neutral character: They both display an electron-deficient π electron system. This similarity is not shared by chloride or acetic acid anions. The acetic acid control experiment shows that the 'organic acid anion' property alone is not sufficient to enable bulk penetration of PBTTT.

8.4 Conclusion

We show that even the highly hydrophobic semiconducting polymer poly[2,5-bis(3-tetradecylthiophen-2-yl) thieno[3,2-*b*]thiophene] (PBTTT) can operate in an organic electrochemical transistor (OECT) rather than field effect (OFET) mode when gated with aqueous media. The required bulk penetration of anions into the semiconducting film within the electrochemical window of water is enabled here by choice of anion, namely, picric acid (PA). OECT mode operation in PBTTT films or its analogues had previously been seen only when gated with solid electrolytes with a larger electrochemical window [207], or for PBTTT analogues with hydrophilic sidechains [206]. In this instance, hydrophilicity allows some penetration of water into the semiconductor bulk, which then carries with it ions that lead to bulk gating. Here, we find bulk gating despite the inability of water to penetrate the highly hydrophobic PBTTT. We believe that PA^- anions can penetrate PBTTT bulk without using water as a 'vector'. We assign this ability to the similarity of PA to solvents for PBTTT, namely chlorinated benzenes: both PA and chlorinated benzenes, display an electron-deficient π electron system. In control experiments, we confirm that OECT mode is not observed when gating PBTTT with a different organic acid (acetic acid) that does not display such π electron system and that the gating mechanism indeed is electrochemical doping rather than a charge transfer mechanism. OECT mode is observed only at rather high PA concentrations in the gate medium (50 mM or more), albeit the weak dissociation of PA into anions means this corresponds to a rather lower concentration of PA^- anions. When OECT mode is observed, it leads to conductivities of ≈ 80 S/cm, slightly larger than for p(g2T-TT), a PBTTT analogue with hydrophilic side chains gated with chloride anions[206].

Chapter 9: Overall Conclusion and Future Work

9.1 Overall conclusion

In this thesis, I have studied the ion sensing properties, and modes of operation, of water gated thin film transistors (WGTFTs). This was in some parts in collaboration with other members of my supervisor's group. This thesis reports my results and conclusions in three aspects of WGTFT research:

1. In my contribution with T. Althagafi in chapter 6, we have demonstrated a simplified ion-selective WGTFT architecture that requires no separate ion- selective membrane[84]. Instead, we added (1% wt./wt.) of a calcium- selective calix[4]arene ionophore known as "calcium ionophore VI" [96] directly to spin casting solutions of the organic semiconductor rrP3HT. We find that resulting WGTFTs cast from ionophore- doped rrP3HT solutions selectively respond to calcium cations dissolved in the gating water with similar characteristics as previous ion- selective WGTFTs [15, 17]. The ionophore- doped rrP3HT simultaneously acts as a semiconductor, and ion- sensitive layer, without the need for a separate ion- selective membrane.

2. In chapter 7, I have performed a systematic study comparing different solution-processed semiconductors in cation- sensitive water- gated thin film transistors (WGTFTs): a hole transporting semiconducting polymer (rrP3HT), and an electron- transporting precursor-route metal oxide (ZnO) [163]. We used the same the ion- selective crown ether DB30C10 dispersed in a plasticised PVC membrane to sensitise the gate contact. We find both organic p-type, and inorganic n-type solution-processed semiconductors have their relative merits, and drawbacks, in ion- sensitive WGTFTs. Hole transporting rrP3HT WGTFTs show low hysteresis under water- gating and give super- Nernstian ion response. However, rrP3HT responds to ionic strength in water even when WGTFTs are not sensitised, compromising selectivity of the ionophore. Electron transporting ZnO WGTFTs show higher mobility, but also stronger hysteresis, and sub- Nernstian response. However, ZnO WGTFTs show little response to ionic strength when not sensitised. I rationalise the super- *vs* sub- Nernstian response characteristics in p-type *vs* n-type WGTFTs as a result of capacitative amplification or attenuation by the ratio of cationic to anionic electric double layers.

3. In chapter 8, I have shown that even the highly hydrophobic semiconducting polymer poly [2,5-bis(3-tetradecylthiophen-2-yl) thieno[3,2-b]thiophene] (PBTTT) can operate in an organic electrochemical transistor (OECT) rather than field effect (OFET) mode when gated with aqueous media [210]. The required bulk penetration of anions into the semiconducting film within the electrochemical window of water is here enabled by choice of anion, namely, picric acid (PA). OECT mode operation in PBTTT films or its analogues had previously been seen only when gated with solid electrolytes with a larger electrochemical window, or for PBTTT analogues with hydrophilic sidechains. We assign the ability of PA anions to penetrate bulk PBTTT to their similarity to PBTTT solvents (chlorinated benzenes), in the sense that they both display an electron-deficient π electron system. In control experiments, we confirm that OECT mode is not observed when gating PBTTT with another organic acid (acetic acid) that does not display such π electron system and that the gating mechanism indeed is electrochemical doping rather than a charge transfer mechanism. At PA < 50 mM concentrations, the transistor still operates and works in field effect mode, *i.e.* gating is via an interfacial EDL. OECT mode is observed only at rather high PA concentrations in an aqueous gate medium (50 mM or more), but when it is, it leads to drain currents far in excess to corresponding field- effect gated PBTTT devices, and conductivities of ≈ 80 S/cm, slightly larger than for a PBTTT analogue with hydrophilic side chains gated with chloride anions.

9.2 Future work

From experimental work of my thesis, I can propose the following future work:

1. From chapter 6, This method can create another simple way of using strong back catalogues of cation selective, water-insoluble macrocycles (e.g. valinomycin [17], phthalocyanines [183, 184]and calixarenes [87, 88]) for experimental cation detectors.

2. From chapter 7, unfortunately, we observe unsensitised polythiophene [rrP3HT] WGTFTs displaying response to increasing K^+ and Na^+ concentration, simply due to increasing ionic strength of the gating solution. However, ZnO WGTFTs show a negligible response to ionic strength when not sensitised. Our study suggests that the optimum semiconductor material for ion-selective WGTFTs would be a precursor-route inorganic p-type semiconductor.

3. From chapter 7, minor changes can be made to our design (PVC membrane on gate electrode) but two semiconductors on the same substrate (two transistors). This architecture

not only leads to simpler designs, but also more responsive sensors. This synergy is demonstrated in a novel sensor readout scheme, where the hole-transporting (rrP3HT) WGTFT is combined with the electron transporting (ZnO) WGTFT into a CMOS inverter. Inverter output is fed back to its input to set the inverter to its 'trip point', $V_{out} = V_{in}$. Trip point shifts in response to increasing potassium concentration in the gate medium due to both threshold shift, and reduced transconductance, giving a superliner response in the V_{trip} *vs* log c plot. This surpasses the usually reported linear (Nernstian) shift of threshold *vs.* log c while using a simplified WGTFT design and a low-cost readout scheme.

4. From chapter 8, we observe the concentrations c of picric acid from zero up to 1mM, saturated drain current remains low and in fact, somewhat decreases with increasing c. At low PA concentrations, the transistor still operates in field effect mode (*i.e*. gating is via an interfacial EDL). Based on this, we observed a significant shift under threshold voltage between two concentrations: 1microM and 1 mM. This means that there may be organic semiconductors sensitive to explosive material. For this reason, we can use our device via WGOTFT to detect explosives, a novel application which has not been previously reported in the literature related to WGOTFTs.

5. In the viva examination I discussed with Dr Nielsen previous published studies [206,207], and how it is possible to apply these same optical techniques to assess the mechanism in my experiments and definitively confirm between OFET mode and OECT mode. This has been determined previously using optical absorption measurements for semiconducting thin film with increasing applied gate voltage V_G. In OECT mode, we would expect to observe an increase in intensity of the polaronic absorption band with increasing V_G, a result of bulk doping. This effect is largely absent for the OFET mode, and this experiment would allow us to clearly distinguish between these two modes. This experiment would be important future work to determine the doping mechanism.

References

[1] A. J. Bandodkar, W. J. Jeang, R. Ghaffari, and J. A. Rogers, "Wearable Sensors for Biochemical Sweat Analysis," *Annual Review of Analytical Chemistry,* vol. 12, 2019.

[2] B. W. Abegaz, T. Datta, and S. M. Mahajan, "Sensor technologies for the energy-water nexus–A review," *Applied energy,* vol. 210, pp. 451-466, 2018.

[3] F. Ingelrest, G. Barrenetxea, G. Schaefer, M. Vetterli, O. Couach, and M. Parlange, "Sensorscope: Application-specific sensor network for environmental monitoring," *ACM Transactions on Sensor Networks,* vol. 6, no. 2, p. 17, 2010.

[4] H.-E. Joe, H. Yun, S.-H. Jo, M. B. Jun, and B.-K. Min, "A review on optical fiber sensors for environmental monitoring," *International journal of precision engineering manufacturing-green technology,* vol. 5, no. 1, pp. 173-191, 2018.

[5] Y. Chu *et al.*, "Health Monitoring: Human Pulse Diagnosis for Medical Assessments Using a Wearable Piezoelectret Sensing System " *Advanced Functional Materials,* vol. 28, no. 40, p. 1870292, 2018.

[6] L. Baroni, L. Cenci, M. Tettamanti, and M. Berati, "Evaluating the environmental impact of various dietary patterns combined with different food production systems," *European journal of clinical nutrition,* vol. 61, no. 2, p. 279, 2007.

[7] C. D. Koolen and G. Rothenberg, "Air Pollution in Europe," *ChemSusChem,* vol. 12, no. 1, pp. 164-172, 2019.

[8] G. Wang *et al.*, "Persistent sulfate formation from London Fog to Chinese haze," *Proceedings of the National Academy of Sciences,* vol. 113, no. 48, pp. 13630-13635, 2016.

[9] K. Mollenhauer, K. G. E. Johnson, and H. Tschöke, *Handbook of Diesel Engines*. Springer Berlin Heidelberg, 2010.

[10] H. Omidvarborna, A. Kumar, and D.-S. Kim, "NO_x emissions from low-temperature combustion of biodiesel made of various feedstocks and blends," *Fuel processing technology,* vol. 140, pp. 113-118, 2015.

[11] W. Todts, "Cars with engines:can they ever be clean?," in "Transport & Environment ", 2018 European Federation for Transport and Environment AISBL, September 2018

[12] N. Emissions. National Emissions Reported to the Convention on Long-Range Transboundary Air Pollution (LRTAP Convention)" can be found under https://www.eea.europa.eu/data-and-maps/data/national-emissions-reported-to-the-convention-on-long-range-transboundary-air-pollutionlrtap-convention-11

[13] J. D. Newman and A. P. Turner, "Home blood glucose biosensors: a commercial perspective," *Biosensors and Bioelectronics* vol. 20, no. 12, pp. 2435-2453, 2005.

[14] J. Wang, "Electrochemical glucose biosensors," *Chemical reviews,* vol. 108, no. 2, pp. 814-825, 2008.

[15] K. Schmoltner, J. Kofler, A. Klug, and E. J. List-Kratochvil, "Electrolyte-Gated Organic Field-Effect Transistor for Selective Reversible Ion Detection," *Adv Mater,* vol. 25, no. 47, pp. 6895-6899, 2013.

[16] J. Kofler, K. Schmoltner, A. Klug, and E. J. List-Kratochvil, "Hydrogen ion-selective electrolyte-gated organic field-effect transistor for pH sensing," *Applied Physics Letters,* vol. 104, no. 19, p. 72_1, 2014.

[17] K. Melzer, A. Münzer, E. Jaworska, K. Maksymiuk, A. Michalska, and G. Scarpa, "Selective ion-sensing with membrane-functionalized electrolyte-gated carbon nanotube field-effect transistors," *Analyst,* vol. 139, no. 19, pp. 4947-4954, 2014.

[18] S. K. Menon, N. R. Modi, B. Patel, and M. B. Patel, "Azo calix [4] arene based neodymium (III)-selective PVC membrane sensor," *Talanta,* vol. 83, no. 5, pp. 1329-1334, 2011.

[19] X. Chen, G. Zhou, S. Mao, and J. Chen, "Rapid detection of nutrients with electronic sensors: a review," *Environmental Science: Nano,* vol. 5, no. 4, pp. 837-862, 2018.

[20] F. J. W. c. Edition, "Guidelines for drinking-water quality," vol. 38, no. 4, pp. 104-8, 2011.

[21] M. A. Zoroddu, J. Aaseth, G. Crisponi, S. Medici, M. Peana, and V. M. Nurchi, "The essential metals for humans: a brief overview," *Journal of inorganic biochemistry,* 2019.
[22] J. Yee, "Hypercalcemia," 2007.
[23] M. Jaishankar, T. Tseten, N. Anbalagan, B. B. Mathew, and K. N. Beeregowda, "Toxicity, mechanism and health effects of some heavy metals," *Interdisciplinary toxicology,* vol. 7, no. 2, pp. 60-72, 2014.
[24] M. B. Gumpu, S. Sethuraman, U. M. Krishnan, and J. B. B. Rayappan, "A review on detection of heavy metal ions in water–An electrochemical approach," *Sensors and Actuators B: Chemical,* vol. 213, pp. 515-533, 2015.
[25] S. Chowdhury, M. J. Mazumder, O. Al-Attas, and T. Husain, "Heavy metals in drinking water: occurrences, implications, and future needs in developing countries," *Science of the total Environment,* vol. 569, pp. 476-488, 2016.
[26] Z. Li, M. Nagashima, and K. Ikeda, "Treatment Technology of Hazardous Water Contaminated with Radioisotopes with Paper Sludge Ash-Based Geopolymer—Stabilization of Immobilization of Strontium and Cesium by Mixing Seawater," *Materials,* vol. 11, no. 9, p. 1521, 2018.
[27] A. Burger and I. Lichtscheidl, "Stable and radioactive cesium: a review about distribution in the environment, uptake and translocation in plants, plant reactions and plants' potential for bioremediation," *Science of the Total Environment,* vol. 618, pp. 1459-1485, 2018.
[28] D. Dechojarassri *et al.*, "Preparation of alginate fibers coagulated by calcium chloride or sulfuric acid: Application to the adsorption of Sr^{2+}," *Journal of hazardous materials,* vol. 355, pp. 154-161, 2018.
[29] C.-H. Chiu, Y.-H. Sung, and S.-D. Huang, "Simultaneous determination of manganese, iron and cobalt in copper with a multi-element graphite furnace atomic absorption spectrometer," *Spectrochimica Acta Part B: Atomic Spectroscopy,* vol. 58, no. 3, pp. 575-580, 2003.
[30] E. Takara, S. Pasini-Cabello, S. Cerutti, J. Gasquez, and L. Martinez, "On-line preconcentration/determination of copper in parenteral solutions using activated carbon by inductively coupled plasma optical emission spectrometry," *Journal of pharmaceutical and biomedical analysis,* vol. 39, no. 3-4, pp. 735-739, 2005.
[31] J. Wang, E. H. Hansen, and B. Gammelgaard, "Flow injection on-line dilution for multi-element determination in human urine with detection by inductively coupled plasma mass spectrometry," *Talanta,* vol. 55, no. 1, pp. 117-126, 2001.
[32] T. Liu, G. Li, N. Zhang, and Y. Chen, "An inorganic–organic hybrid optical sensor for heavy metal ion detection based on immobilizing 4-(2-pyridylazo)-resorcinol on functionalized HMS," *Journal of hazardous materials,* vol. 201, pp. 155-161, 2012.
[33] L. Kergoat *et al.*, "A water-gate organic field-effect transistor," *Adv Mater,* vol. 22, no. 23, pp. 2565-2569, 2010.
[34] P. K. Weimer, "The TFT a new thin-film transistor," *Proceedings of the IRE,* vol. 50, no. 6, pp. 1462-1469, 1962.
[35] H. Du, X. Lin, Z. Xu, and D. Chu, "Electric double-layer transistors: a review of recent progress," *Journal of Materials Science,* vol. 50, no. 17, pp. 5641-5673, 2015.
[36] M. Kaisti, "Detection principles of biological and chemical FET sensors," *Biosensors and Bioelectronics,* vol. 98, pp. 437-448, 2017.
[37] S. Joshi *et al.*, "Ambient Processed, Water-Stable, Aqueous-Gated sub 1 V n-type Carbon Nanotube Field Effect Transistor," *Scientific reports,* vol. 8, no. 1, p. 11386, 2018.
[38] L. Petti *et al.*, "Metal oxide semiconductor thin-film transistors for flexible electronics," *Applied Physics Reviews,* vol. 3, no. 2, p. 021303, 2016.
[39] J. S. Park, W.-J. Maeng, H.-S. Kim, and J.-S. Park, "Review of recent developments in amorphous oxide semiconductor thin-film transistor devices," *Thin solid films,* vol. 520, no. 6, pp. 1679-1693, 2012.

[40] E. Fortunato, P. Barquinha, and R. Martins, "Oxide semiconductor thin-film transistors: a review of recent advances," *Adv Mater,* vol. 24, no. 22, pp. 2945-2986, 2012.
[41] S. Panda, *Microelectronics and optoelectronics technology*. Laxmi Publications, 2009.
[42] C. Tanase, E. Meijer, P. Blom, and D. De Leeuw, "Local charge carrier mobility in disordered organic field-effect transistors," *Organic electronics,* vol. 4, no. 1, pp. 33-37, 2003.
[43] C. Tanase, E. Meijer, P. Blom, and D. De Leeuw, "Unification of the hole transport in polymeric field-effect transistors and light-emitting diodes," *Physical review letters,* vol. 91, no. 21, p. 216601, 2003.
[44] A. Tixier-Mita *et al.*, "Review on thin-film transistor technology, its applications, and possible new applications to biological cells," *Japanese Journal of Applied Physics,* vol. 55, no. 4S, p. 04EA08, 2016.
[45] S. A. Algarni, T. M. Althagafi, A. Al Naim, and M. Grell, "A water-gated organic thin film transistor as a sensor for water-borne amines," *Talanta,* vol. 153, pp. 107-110, 2016.
[46] S. Panda, "Enhanced pH sensitivity over the Nernst limit of electrolyte gated a-IGZO thin film transistor using branched polyethylenimine," *RSC advances,* vol. 6, no. 10810–10815, 2016.
[47] L. Torsi, M. Magliulo, K. Manoli, and G. Palazzo, "Organic field-effect transistor sensors: a tutorial review," *Chem Soc Rev,* vol. 42, no. 22, pp. 8612-28, 2013.
[48] C. Wang, H. Dong, W. Hu, Y. Liu, and D. Zhu, "Semiconducting π-conjugated systems in field-effect transistors: a material odyssey of organic electronics," *Chemical reviews,* vol. 112, no. 4, pp. 2208-2267, 2011.
[49] C. W. Shih, A. Chin, C. F. Lu, and W. F. Su, "Remarkably High Hole Mobility Metal-Oxide Thin-Film Transistors," *Sci Rep,* vol. 8, no. 1, p. 889, 2018.
[50] D. Sun, C. Chen, J. Zhang, X. Wu, H. Chen, and T. Guo, "High performance inkjet-printed metal oxide thin film transistors via addition of insulating polymer with proper molecular weight," *Applied Physics Letters,* vol. 112, no. 1, p. 012102, 2018.
[51] T. M. Althagafi, A. F. Al Baroot, and M. Grell, "A new precursor route to semiconducting Zinc Oxide," *IEEE Electron Device Letters,* vol. 37, no. 10, pp. 1299-1302, 2016.
[52] W. Xu, H. Li, J.-B. Xu, and L. Wang, "Recent Advances of Solution-Processed Metal Oxide Thin-Film Transistors," *ACS Appl Mater Interfaces,* 2018.
[53] W. Xu *et al.*, "Fully solution-processed metal oxide thin-film transistors via a low-temperature aqueous route," *Ceramics International,* vol. 43, no. 8, pp. 6130-6137, 2017.
[54] K. C. Fairley *et al.*, "Non-uniform composition profiles in inorganic thin films from aqueous solutions," *ACS Appl Mater Interfaces,* vol. 8, no. 1, pp. 667-672, 2015.
[55] J. Socratous *et al.*, "Electronic Structure of Low-Temperature Solution-Processed Amorphous Metal Oxide Semiconductors for Thin-Film Transistor Applications," *Advanced Functional Materials,* vol. 25, no. 12, pp. 1873-1885, 2015.
[56] I. Isakov *et al.*, "Exploring the Leidenfrost Effect for the Deposition of High-Quality In2 O3 Layers via Spray Pyrolysis at Low Temperatures and Their Application in High Electron Mobility Transistors," *Advanced Functional Materials,* p. 1606407, 2017.
[57] T. M. Althagafi, S. A. Algarni, A. Al Naim, J. Mazher, and M. Grell, "Precursor-route ZnO films from a mixed casting solvent for high performance aqueous electrolyte-gated transistors," *Physical Chemistry Chemical Physics,* vol. 17, no. 46, pp. 31247-31252, 2015.
[58] S. H. Kim *et al.*, "Electrolyte-gated transistors for organic and printed electronics," *Advanced Materials,* vol. 25, no. 13, pp. 1822-1846, 2013.
[59] R. P. Ortiz, A. Facchetti, and T. J. Marks, "High-k organic, inorganic, and hybrid dielectrics for low-voltage organic field-effect transistors," *Chemical reviews,* vol. 110, no. 1, pp. 205-239, 2009.

[60] L.-L. Chua *et al.*, "General observation of n-type field-effect behaviour in organic semiconductors," *Nature,* vol. 434, no. 7030, p. 194, 2005.
[61] Z. Adamczyk, B. Jachimska, T. Jasiński, P. Warszyński, and M. Wasilewska, "Structure of poly (sodium 4-styrenesulfonate) (PSS) in electrolyte solutions: Theoretical modeling and measurements," *Colloids and Surfaces A: Physicochemical and Engineering Aspects,* vol. 343, no. 1-3, pp. 96-103, 2009.
[62] Y. N. Sudhakar and M. Selvakumar, "Lithium perchlorate doped plasticized chitosan and starch blend as biodegradable polymer electrolyte for supercapacitors," *Electrochimica Acta,* vol. 78, pp. 398-405, 2012.
[63] S. A. Algarni, T. M. Althagafi, P. J. Smith, and M. Grell, "An ionic liquid-gated polymer thin film transistor with exceptionally low “on” resistance," *Applied Physics Letters,* vol. 104, no. 18, p. 182107, 2014.
[64] S. Thiemann, S. Sachnov, S. Porscha, P. Wasserscheid, and J. Zaumseil, "Ionic Liquids for Electrolyte-Gating of ZnO Field-Effect Transistors," *The Journal of Physical Chemistry C,* vol. 116, no. 25, pp. 13536-13544, 2012.
[65] L.-Y. Chang, C.-P. Lee, R. Vittal, J.-J. Lin, and K.-C. Ho, "Enhanced performance of a dye-sensitized solar cell with an amphiphilic polymer-gelled ionic liquid electrolyte," *Journal of Materials Chemistry A,* vol. 1, no. 9, p. 3055, 2013.
[66] T. M. Althagafi, S. A. Algarni, A. Al Naim, J. Mazher, and M. Grell, "Precursor-route ZnO films from a mixed casting solvent for high performance aqueous electrolyte-gated transistors," *Physical Chemistry Chemical Physics,* vol. 17, no. 46, pp. 31247-31252, 2015.
[67] K. Ueno, H. Shimotani, H. Yuan, J. Ye, M. Kawasaki, and Y. Iwasa, "Field-induced superconductivity in electric double layer transistors," *Journal of the Physical Society of Japan,* vol. 83, no. 3, p. 032001, 2014.
[68] S. Mitra, A. Shukla, and S. Sampath, "Electrochemical capacitors with plasticized gel-polymer electrolytes," *Journal of Power Sources,* vol. 101, no. 2, pp. 213-218, 2001.
[69] R. Pashley, M. Rzechowicz, L. Pashley, and M. Francis, "De-gassed water is a better cleaning agent," *The Journal of Physical Chemistry B,* vol. 109, no. 3, pp. 1231-1238, 2005.
[70] K. Izutsu, *Electrochemistry in nonaqueous solutions*. John Wiley & Sons, 2009.
[71] M. Freemantle, *An introduction to ionic liquids*. Royal Society of chemistry, 2010.
[72] F. Endres and S. Z. El Abedin, "Air and water stable ionic liquids in physical chemistry," *Physical Chemistry Chemical Physics,* vol. 8, no. 18, pp. 2101-2116, 2006.
[73] R. Hagiwara *et al.*, "Physicochemical properties of 1, 3-dialkylimidazolium fluorohydrogenate room-temperature molten salts," *Journal of the electrochemical society,* vol. 150, no. 12, pp. D195-D199, 2003.
[74] S. Ono, S. Seki, R. Hirahara, Y. Tominari, and J. Takeya, "High-mobility, low-power, and fast-switching organic field-effect transistors with ionic liquids," *Applied Physics Letters,* vol. 92, no. 10, p. 93, 2008.
[75] S. W. Lee *et al.*, "Periodic array of polyelectrolyte-gated organic transistors from electrospun poly (3-hexylthiophene) nanofibers," *Nano letters,* vol. 10, no. 1, pp. 347-351, 2009.
[76] E. W. Price and C. Orvig, "Matching chelators to radiometals for radiopharmaceuticals," *Chem Soc Rev,* vol. 43, no. 1, pp. 260-290, 2014.
[77] E. Marsault and M. L. Peterson, "Macrocycles are great cycles: applications, opportunities, and challenges of synthetic macrocycles in drug discovery," *Journal of medicinal chemistry,* vol. 54, no. 7, pp. 1961-2004, 2011.
[78] S. Mudaliar and R. R. Henry, "New oral therapies for type 2 diabetes mellitus: the glitazones or insulin sensitizers," *Annual review of medicine,* vol. 52, no. 1, pp. 239-257, 2001.

[79] D. Maity, R. Gupta, R. Gunupuru, D. N. Srivastava, and P. Paul, "Calix [4] arene functionalized gold nanoparticles: application in colorimetric and electrochemical sensing of cobalt ion in organic and aqueous medium," *Sensors Actuators B: Chemical,* vol. 191, pp. 757-764, 2014.
[80] Z. Li, J. R. Askim, and K. S. Suslick, "The optoelectronic nose: colorimetric and fluorometric sensor arrays," *Chemical reviews,* vol. 119, no. 1, pp. 231-292, 2018.
[81] D. Y. Kucherenko, I. Kucherenko, O. Soldatkin, Y. V. Topolnikova, S. Dzyadevych, and A. Soldatkin, "A highly selective amperometric biosensor array for the simultaneous determination of glutamate, glucose, choline, acetylcholine, lactate and pyruvate," *Bioelectrochemistry,* 2019.
[82] L. V. Shkotova, N. Y. Piechniakova, O. L. Kukla, and S. V. Dzyadevych, "Thin-film amperometric multibiosensor for simultaneous determination of lactate and glucose in wine," *Food chemistry,* vol. 197, pp. 972-978, 2016.
[83] E. Zdrachek and E. Bakker, "Potentiometric sensing," *Analytical chemistry,* vol. 91, no. 1, pp. 2-26, 2018.
[84] T. M. Althagafi, A. F. Al Baroot, S. A. Algarni, and M. Grell, "A membrane-free cation selective water-gated transistor," *Analyst,* vol. 141, no. 19, pp. 5571-5576, 2016.
[85] E. Bakker, P. Bühlmann, and E. Pretsch, "Carrier-based ion-selective electrodes and bulk optodes. 1. General characteristics," *Chemical reviews,* vol. 97, no. 8, pp. 3083-3132, 1997.
[86] P. Bühlmann, E. Pretsch, and E. Bakker, "Carrier-based ion-selective electrodes and bulk optodes. 2. Ionophores for potentiometric and optical sensors," *Chemical reviews,* vol. 98, no. 4, pp. 1593-1688, 1998.
[87] V. Arora, H. M. Chawla, and S. P. Singh, "Calixarenes as sensor materials for recognition and separation of metal ions," *Arkivoc,* vol. 2, pp. 172-200, 2007.
[88] M. A. Qazi, Ü. Ocak, M. Ocak, and S. Memon, "An excellent copper selective chemosensor based on calix[4]arene framework," *Analytica Chimica Acta,* vol. 761, pp. 157-168, 2013.
[89] C. J. Pedersen, "Cyclic polyethers and their complexes with metal salts," *Journal of the American Chemical Society,* vol. 89, no. 26, pp. 7017-7036, 1967.
[90] J. Vicens and V. Böhmer, *Calixarenes: a versatile class of macrocyclic compounds*. Springer Science & Business Media, 2012.
[91] D. J. Cram, "Cavitands: organic hosts with enforced cavities," *Science,* pp. 1177-1183, 1983.
[92] C. D. Gutsche, *Calixarenes: an introduction* (no. 10). Royal Society of Chemistry, 2008.
[93] G. McMahon, S. O'Malley, K. Nolan, and D. Diamond, "Important calixarene derivatives—their synthesis and applications," *Arkivoc,* vol. 7, pp. 23-31, 2003.
[94] R. J. Forster and D. Diamond, "Nonlinear calibration of ion-selective electrode arrays for flow injection analysis," *Analytical chemistry,* vol. 64, no. 15, pp. 1721-1728, 1992.
[95] P. E. Georghiou *et al.*, "Synthesis of an upper-and lower-rim functionalized calix [4] arene for detecting calcium ions using a microcantilever sensor," *New Journal of Chemistry,* vol. 37, no. 5, pp. 1298-1301, 2013.
[96] T. McKittrick, D. Diamond, D. J. Marrs, P. O'Hagan, and M. A. McKervey, "Calcium-selective electrode based on a calix [4] arene tetraphosphine oxide," *Talanta,* vol. 43, no. 7, pp. 1145-1148, 1996.
[97] G. W. Gokel, W. M. Leevy, and M. E. Weber, "Crown ethers: sensors for ions and molecular scaffolds for materials and biological models," *Chemical reviews,* vol. 104, no. 5, pp. 2723-2750, 2004.
[98] M. Hiraoka, *Crown ethers and analogous compounds*. Elsevier, 2016.
[99] M. S. Frant, "Historical perspective. History of the early commercialization of ion-selective electrodes," *Analyst,* vol. 119, no. 11, pp. 2293-2301, 1994.
[100] P. T. Kissinger and W. R. Heineman, "Cyclic voltammetry," *Journal of Chemical Education,* vol. 60, no. 9, p. 702, 1983.

[101] R. Yan, S. Qiu, L. Tong, and Y. Qian, "Review of progresses on clinical applications of ion selective electrodes for electrolytic ion tests: from conventional ISEs to graphene-based ISEs," *Chemical Speciation & Bioavailability,* vol. 28, no. 1-4, pp. 72-77, 2016.
[102] P. Bergveld, "Thirty years of ISFETOLOGY: What happened in the past 30 years and what may happen in the next 30 years," *Sensors and Actuators B: Chemical,* vol. 88, no. 1, pp. 1-20, 2003.
[103] P. Bergveld, "Development of an ion-sensitive solid-state device for neurophysiological measurements," *IEEE Transactions on Biomedical Engineering,* no. 1, pp. 70-71, 1970.
[104] S. D. Moss, J. Janata, and C. C. Johnson, "Potassium ion-sensitive field effect transistor," *Analytical Chemistry,* vol. 47, no. 13, pp. 2238-2243, 1975.
[105] S. D. Moss, C. C. Johnson, and J. Janata, "Hydrogen, calcium, and potassium ion-sensitive FET transducers: a preliminary report," *IEEE Transactions on Biomedical Engineering,* no. 1, pp. 49-54, 1978.
[106] S. Casalini, F. Leonardi, T. Cramer, and F. Biscarini, "Organic field-effect transistor for label-free dopamine sensing," *Organic Electronics,* vol. 14, no. 1, pp. 156-163, 2013, doi: 10.1016/j.orgel.2012.10.027.
[107] Z. Bao and J. Locklin, *Organic field-effect transistors*. CRC press, 2007.
[108] L. A. Majewski, R. Schroeder, and M. Grell, "One volt organic transistor," *Advanced Materials,* vol. 17, no. 2, pp. 192-196, 2005.
[109] C. M. Hussain, *Handbook of Nanomaterials for Industrial Applications*. Elsevier, 2018.
[110] Y. Jiang and B. Tian, "Inorganic semiconductor biointerfaces," *Nature Reviews Materials,* p. 1, 2018.
[111] M. Eslamian, "Inorganic and organic solution-processed thin film devices," *Nano-micro letters,* vol. 9, no. 1, p. 3, 2017.
[112] H. Mirzaei and M. Darroudi, "Zinc oxide nanoparticles: Biological synthesis and biomedical applications," *Ceramics International,* vol. 43, no. 1, pp. 907-914, 2017.
[113] M. H. Huang *et al.*, "Room-temperature ultraviolet nanowire nanolasers," *science,* vol. 292, no. 5523, pp. 1897-1899, 2001.
[114] L. Vayssieres, K. Keis, A. Hagfeldt, and S.-E. Lindquist, "Three-dimensional array of highly oriented crystalline ZnO microtubes," *Chemistry of materials,* vol. 13, no. 12, pp. 4395-4398, 2001.
[115] Ü. Özgür *et al.*, "A comprehensive review of ZnO materials and devices," *Journal of Applied Physics,* vol. 98, no. 4, p. 11, 2005.
[116] A. Onodera and M. Takesada, "Electronic ferroelectricity in II-VI semiconductor ZnO," in *Advances in Ferroelectrics*: IntechOpen, 2012.
[117] Z. Zhang, J. Huang, S. Chen, X. Pan, L. Chen, and Z. Ye, "P-type single-crystalline ZnO films obtained by (N, O) dual implantation through dynamic annealing process," *Superlattices and Microstructures,* vol. 100, pp. 468-473, 2016.
[118] B. Bayraktaroglu, K. Leedy, and R. Neidhard, "Microwave ZnO thin-film transistors," *IEEE Electron Device Letters,* vol. 29, no. 9, pp. 1024-1026, 2008.
[119] C.-T. Lee and Y.-H. Lin, "P-type ZnO thin-film transistors and passivation using photoelectrochemical oxidation method," *Applied Physics Express,* vol. 7, no. 7, p. 076502, 2014.
[120] B. S. Ong, C. Li, Y. Li, Y. Wu, and R. Loutfy, "Stable, solution-processed, high-mobility ZnO thin-film transistors," *Journal of the American Chemical Society,* vol. 129, no. 10, pp. 2750-2751, 2007.
[121] A. Al Naim and M. Grell, "Electron transporting water-gated thin film transistors," *Applied Physics Letters,* vol. 101, no. 14, p. 141603, 2012.
[122] M. Singh *et al.*, "Bio-sorbable, liquid electrolyte gated thin-film transistor based on a solution-processed zinc oxide layer," *Faraday discussions,* vol. 174, pp. 383-398, 2014.
[123] W. Brütting, *Physics of organic semiconductors*. John Wiley & Sons, 2006.

[124] P. Bernier, G. Bidan, and S. Lefrant, *Advances in synthetic metals: twenty years of progress in science and technology*. Elsevier, 1999.
[125] R. O. Norman, *Principles of organic synthesis*. Routledge, 2017.
[126] K. Jessie and D. Ball, "Introductory Chemistry," ed, 2014.
[127] R. Farchioni and G. Grosso, *Organic electronic materials: conjugated polymers and low molecular weight organic solids*. Springer Science & Business Media, 2013.
[128] S. Z. Bisri, T. Takenobu, and Y. Iwasa, "The pursuit of electrically-driven organic semiconductor lasers," *Journal of Materials Chemistry C,* vol. 2, no. 16, pp. 2827-2836, 2014.
[129] G. Horowitz, "Organic field-effect transistors," *Advanced Materials,* vol. 10, no. 5, pp. 365-377, 1998.
[130] M. Ahles, R. Schmechel, and H. von Seggern, "N-type organic field-effect transistor based on interface-doped pentacene," *Applied Physics Letters,* vol. 85, no. 19, pp. 4499-4501, 2004.
[131] A. Campbell, D. Bradley, and D. Lidzey, "Space-charge limited conduction with traps in poly (phenylene vinylene) light emitting diodes," *Journal of Applied Physics,* vol. 82, no. 12, pp. 6326-6342, 1997.
[132] W. Pasveer *et al.*, "Unified description of charge-carrier mobilities in disordered semiconducting polymers," *Physical review letters,* vol. 94, no. 20, p. 206601, 2005.
[133] A. F. Paterson *et al.*, "Recent progress in high-mobility organic transistors: a reality check," *Advanced Materials,* vol. 30, no. 36, p. 1801079, 2018.
[134] V. Arkhipov, I. Fishchuk, A. Kadashchuk, and H. Bässler, "Semiconducting Polymers: Chemistry, Physics and Engineering," ed: Wiley-VCH Verlag Weinheim, 2007.
[135] M. Redecker, D. D. Bradley, M. Inbasekaran, W. W. Wu, and E. P. Woo, "High Mobility Hole Transport Fluorene-Triarylamine Copolymers," *Advanced Materials,* vol. 11, no. 3, pp. 241-246, 1999.
[136] W. S. Liu, C. C. Liu, and M. Y. Kuo, "High-Performance p-Channel Organic Semiconducting Candidates Based on Benzo [1, 2-k; 4, 5-k′] difluoranthene Derivatives," *Chemistry–A European Journal,* vol. 15, no. 24, pp. 5896-5900, 2009.
[137] F. Liscio *et al.*, "Structure and Morphology of PDI8-CN2 for n-Type Thin-Film Transistors," *Advanced Functional Materials,* vol. 22, no. 5, pp. 943-953, 2012.
[138] Y. Xu, C. Liu, D. Khim, and Y.-Y. Noh, "Development of high-performance printed organic field-effect transistors and integrated circuits," *Physical Chemistry Chemical Physics,* vol. 17, no. 40, pp. 26553-26574, 2015.
[139] M. K. Silvan Pretl, Aleš Hamáček, Tomáš Džugan, Jan Řeboun, Jiří Čengery, "Characterization of the Organic Field–Effect Transistor
Based on Solution Processed P3HT," *IEEE,* 2010.
[140] K. Manoli *et al.*, "A comparative study of the gas sensing behavior in P3HT-and PBTTT-based OTFTs: The influence of film morphology and contact electrode position," *Sensors (Basel),* vol. 14, no. 9, pp. 16869-16880, 2014.
[141] R. D. McCullough, R. D. Lowe, M. Jayaraman, and D. L. Anderson, "Design, synthesis, and control of conducting polymer architectures: structurally homogeneous poly (3-alkylthiophenes)," *The Journal of organic chemistry,* vol. 58, no. 4, pp. 904-912, 1993.
[142] H. Sirringhaus *et al.*, "Two-dimensional charge transport in self-organized, high-mobility conjugated polymers," *Nature,* vol. 401, no. 6754, p. 685, 1999.
[143] I. McCulloch *et al.*, "Liquid-crystalline semiconducting polymers with high charge-carrier mobility," *Nat Mater,* vol. 5, no. 4, pp. 328-33, Apr 2006.
[144] P. Boufflet *et al.*, "Using Molecular Design to Increase Hole Transport: Backbone Fluorination in the Benchmark Material Poly (2, 5-bis (3-alkylthiophen-2-yl) thieno [3, 2-b]-thiophene (pBTTT)," *Advanced Functional Materials,* vol. 25, no. 45, pp. 7038-7048, 2015.
[145] B. Hamadani, D. Gundlach, I. McCulloch, and M. Heeney, "Undoped polythiophene field-effect transistors with mobility of 1 cm 2 V− 1 s− 1," *Applied Physics Letters,* vol. 91, no. 24, p. 243512, 2007.

[146] C. Liao and F. Yan, "Organic semiconductors in organic thin-film transistor-based chemical and biological sensors," *Polymer reviews,* vol. 53, no. 3, pp. 352-406, 2013.
[147] C. Liao, M. Zhang, M. Y. Yao, T. Hua, L. Li, and F. Yan, "Flexible organic electronics in biology: materials and devices," *Adv Mater,* vol. 27, no. 46, pp. 7493-7527, 2015.
[148] J. Rivnay, S. Inal, A. Salleo, R. M. Owens, M. Berggren, and G. G. Malliaras, "Organic electrochemical transistors," *Nature Reviews Materials,* vol. 3, p. 17086, 2018.
[149] D. Khodagholy *et al.*, "High transconductance organic electrochemical transistors," *Nat Commun,* vol. 4, p. 2133, 2013.
[150] J. Rivnay *et al.*, "High-performance transistors for bioelectronics through tuning of channel thickness," *Science Advances,* vol. 1, no. 4, p. e1400251, 2015.
[151] G. D. Christian, P. Dasgupta, and K. Schug, *Analytical Chemistry, 7th Edition: Seventh Edition*. Wiley Global Education, 2013.
[152] B. Nikolski and T. Tolmacheva, "Permeability of membranes. II. Effect of boric anhydride and aluminium oxide on the electrode properties of glass," *Zh. Fiz. Khim,* vol. 10, pp. 504-512, 1937.
[153] B. Klein *et al.*, "Ozone oxidation of cassava starch in aqueous solution at different pH," *Food chemistry,* vol. 155, pp. 167-173, 2014.
[154] B. Kasprzyk-Hordern, M. Ziółek, and J. Nawrocki, "Catalytic ozonation and methods of enhancing molecular ozone reactions in water treatment," *Applied Catalysis B: Environmental,* vol. 46, no. 4, pp. 639-669, 2003.
[155] D. M. Mattox, "The foundations of vacuum coating technology. 2003," *Norwich, NY: Noyes Publications/William Andrew Pub*.
[156] D. Johannsmann, *The Quartz Crystal Microbalance in Soft Matter Research*. Springer, 2014.
[157] F. C. Krebs, "Fabrication and processing of polymer solar cells: a review of printing and coating techniques," *Solar Energy Materials and Solar Cells,* vol. 93, no. 4, pp. 394-412, 2009.
[158] H. Yang, S. W. LeFevre, C. Y. Ryu, and Z. Bao, "Solubility-driven thin film structures of regioregular poly (3-hexyl thiophene) using volatile solvents," *Applied Physics Letters,* vol. 90, no. 17, p. 172116, 2007.
[159] K. Choy, "Chemical vapour deposition of coatings," *Progress in materials science,* vol. 48, no. 2, pp. 57-170, 2003.
[160] G. Adamopoulos, S. Thomas, P. H. Wöbkenberg, D. D. Bradley, M. A. McLachlan, and T. D. Anthopoulos, "High-Mobility Low-Voltage ZnO and Li-Doped ZnO Transistors Based on ZrO2 High-k Dielectric Grown by Spray Pyrolysis in Ambient Air," *Adv Mater,* vol. 23, no. 16, pp. 1894-1898, 2011.
[161] Y.-H. Yang, S. S. Yang, C.-Y. Kao, and K.-S. Chou, "Chemical and Electrical Properties of Low-Temperature Solution-Processed In–Ga–Zn-O Thin-Film Transistors," *IEEE Electron Device Letters,* vol. 31, no. 4, pp. 329-331, 2010.
[162] J.-Y. Bae, J. Park, H. Y. Kim, H.-S. Kim, and J.-S. Park, "Facile Route to the Controlled Synthesis of Tetragonal and Orthorhombic SnO2 Films by Mist Chemical Vapor Deposition," *ACS Appl Mater Interfaces,* vol. 7, no. 22, pp. 12074-12079, 2015.
[163] A. F. Al Baroot and M. Grell, "Comparing electron-and hole transporting semiconductors in ion sensitive water-gated transistors," *Materials Science in Semiconductor Processing,* vol. 89, pp. 216-222, 2019.
[164] D. Perednis and L. J. Gauckler, "Thin film deposition using spray pyrolysis," *Journal of electroceramics,* vol. 14, no. 2, pp. 103-111, 2005.
[165] L. Filipovic *et al.*, "Modeling the growth of tin dioxide using spray pyrolysis deposition for gas sensor applications," *IEEE transactions on semiconductor manufacturing,* vol. 27, no. 2, pp. 269-277, 2014.
[166] J. B. Mooney and S. B. Radding, "Spray pyrolysis processing," *Annual review of materials science,* vol. 12, no. 1, pp. 81-101, 1982.

[167] C. Falcony, M. Aguilar-Frutis, and M. García-Hipólito, "Spray Pyrolysis Technique; High-K Dielectric Films and Luminescent Materials: A Review," *Micromachines,* vol. 9, no. 8, p. 414, 2018.
[168] N. Lehraki, M. Aida, S. Abed, N. Attaf, A. Attaf, and M. Poulain, "ZnO thin films deposition by spray pyrolysis: Influence of precursor solution properties," *Current Applied Physics,* vol. 12, no. 5, pp. 1283-1287, 2012.
[169] E. Bacaksiz, M. Parlak, M. Tomakin, A. Özçelik, M. Karakız, and M. Altunbaş, "The effects of zinc nitrate, zinc acetate and zinc chloride precursors on investigation of structural and optical properties of ZnO thin films," *Journal of Alloys and Compounds,* vol. 466, no. 1-2, pp. 447-450, 2008.
[170] S. D. Gunjal, Y. B. Khollam, S. A. Arote, S. R. Jadkar, P. N. Shelke, and K. C. Mohite, "Structural, optical and electrical properties of spray pyrolysis deposited CdS films," in *Macromolecular Symposia*, 2015, vol. 347: Wiley Online Library, pp. 9-15.
[171] J. Raj Mohamed and L. Amalraj, "Effect of precursor concentration on physical properties of nebulized spray deposited In2S3 thin films," *Journal of Asian Ceramic Societies,* vol. 4, no. 3, pp. 357-366, 2016.
[172] M.-I. Baraton and L. Merhari, "Surface chemistry of TiO2 nanoparticles: influence on electrical and gas sensing properties," *Journal of the European Ceramic Society,* vol. 24, no. 6, pp. 1399-1404, 2004.
[173] D. XT, *STYLUS PROFILER -USER MANUAL*, United States of America: Bruker Corporation, 2011.
[174] Y. Yuan and T. R. Lee, "Contact angle and wetting properties," in *Surface science techniques*: Springer, 2013, pp. 3-34.
[175] T. Huhtamäki, X. Tian, J. T. Korhonen, and R. H. Ras, "Surface-wetting characterization using contact-angle measurements," *Nature protocols,* vol. 13, no. 7, p. 1521, 2018.
[176] K.-Y. Law and H. Zhao, *Surface wetting: characterization, contact angle, and fundamentals*. Springer Switzerland, 2016.
[177] S. Park *et al.*, "Sub-0.5 V highly stable aqueous salt gated metal oxide electronics," *Scientific reports,* vol. 5, p. 13088, 2015.
[178] S. Y. Park, M. Park, and H. H. Lee, "Cooperative polymer gate dielectrics in organic thin-film transistors," *Applied Physics Letters,* vol. 85, no. 12, pp. 2283-2285, 2004.
[179] Z. Ye, Y. Yuan, H. Xu, Y. Liu, J. Luo, and M. Wong, "Mechanism and origin of hysteresis in oxide thin-film transistor and its application on 3-D nonvolatile memory," *IEEE Transactions on Electron Devices,* vol. 64, no. 2, pp. 438-446, 2017.
[180] T. N. Ng, B. Russo, and A. C. Arias, "Degradation mechanisms of organic ferroelectric field-effect transistors used as nonvolatile memory," *Journal of Applied Physics,* vol. 106, no. 9, p. 094504, 2009.
[181] M. Egginger, S. Bauer, R. Schwödiauer, H. Neugebauer, and N. S. Sariciftci, "Current versus gate voltage hysteresis in organic field effect transistors," *Monatshefte für Chemie-Chemical Monthly,* vol. 140, no. 7, pp. 735-750, 2009.
[182] Y. Kuo, "Thin Film Transistors 10 (TFT 10)," 2010: The Electrochemical Society.
[183] M. Kandaz, M. N. Yarasir, and A. Koca, "Selective metal sensor phthalocyanines bearing non-peripheral functionalities: Synthesis, spectroscopy, electrochemistry and spectroelectrochemistry," *Polyhedron,* vol. 28, no. 2, pp. 257-262, 2009.
[184] L. K. Kumawat, N. Mergu, A. K. Singh, and V. K. Gupta, "A novel optical sensor for copper ions based on phthalocyanine tetrasulfonic acid," *Sensors and Actuators B: Chemical,* vol. 212, pp. 389-394, 2015.
[185] L. Lvova, C. Di Natale, and R. Paolesse, "Porphyrin-based chemical sensors and multisensor arrays operating in the liquid phase," *Sensors and Actuators B: Chemical,* vol. 179, pp. 21-31, 2013.
[186] A. Giovannitti *et al.*, "Sodium and Potassium Ion Selective Conjugated Polymers for Optical Ion Detection in Solution and Solid State," *Advanced Functional Materials,* vol. 26, no. 4, pp. 514-523, 2016.

[187] F. Buth, A. Donner, M. Sachsenhauser, M. Stutzmann, and J. A. Garrido, "Biofunctional electrolyte-gated organic field-effect transistors," *Adv Mater,* Research Support, Non-U.S. Gov't vol. 24, no. 33, pp. 4511-7, 2012.
[188] R. F. de Oliveira, L. Merces, T. P. Vello, and C. C. B. Bufon, "Water-gated phthalocyanine transistors: Operation and transduction of the peptide–enzyme interaction," *Organic Electronics,* vol. 31, pp. 217-226, 2016.
[189] A. Michalska, K. Pyrzyńska, and K. Maksymiuk, "Method of achieving desired potentiometric responses of polyacrylate-based ion-selective membranes," *Analytical chemistry,* vol. 80, no. 10, pp. 3921-3924, 2008.
[190] T. M. Althagafi, S. A. Algarni, and M. Grell, "Innate cation sensitivity in a semiconducting polymer," *Talanta,* vol. 158, pp. 70-76, 2016.
[191] R. Ahmad, M.-S. Ahn, and Y.-B. Hahn, "Fabrication of a non-enzymatic glucose sensor field-effect transistor based on vertically-oriented ZnO nanorods modified with Fe2O3," *Electrochemistry Communications,* vol. 77, pp. 107-111, 2017.
[192] R. Ahmad, M.-S. Ahn, and Y.-B. Hahn, "ZnO nanorods array based field-effect transistor biosensor for phosphate detection," *Journal of colloid and interface science,* vol. 498, pp. 292-297, 2017.
[193] R. Ahmad and Y.-B. Hahn, "Nonenzymatic flexible field-effect transistor based glucose sensor fabricated using NiO quantum dots modified ZnO nanorods," *Journal of colloid and interface science,* vol. 512, pp. 21-28, 2018.
[194] R. Ahmad, T. Mahmoudi, M.-S. Ahn, and Y.-B. Hahn, "Recent advances in nanowires-based field-effect transistors for biological sensor applications," *Biosensors and Bioelectronics,* 2017.
[195] C. J. Pedersen, "Macrocyclic Polyethers: Dibenzo-18-Crown-6 Polyether and Dicyclohexyl-18-Crown-6 Polyether," *Organic Syntheses,* vol. 52, p. 66, 1972, doi: 10.15227/orgsyn.052.0066.
[196] D. Lee and J. Thomas, "4′-picrylamino-5′-nitrobenzo-18-crown-6 as a sensing reagent in potassium ion-selective electrode membranes," *Talanta,* vol. 41, no. 6, pp. 901-907, 1994.
[197] J. Petranek and O. Ryba, "Potassium-selective electrodes based on macrocyclic polyethers: The effect of structure of the neutral carrier on selectivity," *Analytica Chimica Acta,* vol. 72, no. 2, pp. 375-380, 1974.
[198] J. Y. Na, B. Kang, D. H. Sin, K. Cho, and Y. D. Park, "Understanding solidification of polythiophene thin films during spin-coating: effects of spin-coating time and processing additives," *Sci Rep,* vol. 5, p. 13288, 2015.
[199] J. W. Jeong *et al.*, "The response characteristics of a gas sensor based on poly-3-hexylithiophene thin-film transistors," *Sensors and Actuators B: Chemical,* vol. 146, no. 1, pp. 40-45, 2010.
[200] R. Giridharagopal *et al.*, "Electrochemical strain microscopy probes morphology-induced variations in ion uptake and performance in organic electrochemical transistors," *Nat Mater,* vol. 16, no. 7, p. 737, 2017.
[201] A. Nawaz *et al.*, "High mobility organic field-effect transistors based on defect-free regioregular poly (3-hexylthiophene-2, 5-diyl)," *Organic Electronics,* vol. 38, pp. 89-96, 2016.
[202] M. Spijkman, E. Smits, J. Cillessen, F. Biscarini, P. Blom, and D. De Leeuw, "Beyond the Nernst-limit with dual-gate ZnO ion-sensitive field-effect transistors," *Applied Physics Letters,* vol. 98, no. 4, p. 043502, 2011.
[203] S. Liu *et al.*, "Conjugated Polymer for Voltage-Controlled Release of Molecules," *Adv Mater,* vol. 29, no. 35, p. 1701733, 2017.
[204] R. Porrazzo, S. Bellani, A. Luzio, E. Lanzarini, M. Caironi, and M. R. Antognazza, "Improving mobility and electrochemical stability of a water-gated polymer field-effect transistor," *Organic Electronics,* vol. 15, no. 9, pp. 2126-2134, 2014.
[205] R. Porrazzo *et al.*, "Field-effect and capacitive properties of water-gated transistors based on polythiophene derivatives," *APL Materials,* vol. 3, no. 1, p. 014905, 2015.

[206] A. Giovannitti *et al.*, "Controlling the mode of operation of organic transistors through side-chain engineering," *Proceedings of the National Academy of Sciences,* vol. 113, no. 43, pp. 12017-12022, 2016.
[207] J. D. Yuen *et al.*, "Electrochemical doping in electrolyte-gated polymer transistors," *Journal of the American Chemical Society,* vol. 129, no. 46, pp. 14367-14371, 2007.
[208] R. Porrazzo *et al.*, "Water-gated n-type organic field-effect transistors for complementary integrated circuits operating in an aqueous environment," *ACS omega,* vol. 2, no. 1, pp. 1-10, 2017.
[209] A. F. Al Naim and M. Grell, "Organic solvents as gate media for thin-film transistors," *Journal of Applied Physics,* vol. 112, no. 11, p. 114502, 2012.
[210] A. Al Baroot, A. Alshammari, and M. Grell, "Electrochemical gating of a hydrophobic organic semiconductor with aqueous media," *Thin Solid Films,* vol. 669, pp. 665-669, 2019.

Copyright permission

Title: Comparing electron- and hole transporting semiconductors in ion sensitive water- gated transistors

Author: Abbad F. Al Baroot,Martin Grell

Publication: Materials Science in Semiconductor Processing

Publisher: Elsevier

Date: January 2019

Logged in as:
Abbad Al Baroot
University of Sheffield
Account #:
3001369741

LOGOUT

Please note that, as the author of this Elsevier article, you retain the right to include it in a thesis or dissertation, provided it is not published commercially. Permission is not required, but please ensure that you reference the journal as the original source. For more information on this and on your other retained rights, please visit: https://www.elsevier.com/about/our-business/policies/copyright#Author-rights

BACK CLOSE WINDOW

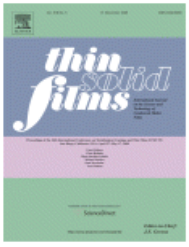

Title: Electrochemical gating of a hydrophobic organic semiconductor with aqueous media

Author: Abbad Al Baroot,Alhulw Alshammari,Martin Grell

Publication: Thin Solid Films

Publisher: Elsevier

Date: 1 January 2019

Logged in as:
Abbad Al Baroot
University of Sheffield
Account #:
3001369741

LOGOUT

Please note that, as the author of this Elsevier article, you retain the right to include it in a thesis or dissertation, provided it is not published commercially. Permission is not required, but please ensure that you reference the journal as the original source. For more information on this and on your other retained rights, please visit: https://www.elsevier.com/about/our-business/policies/copyright#Author-rights

BACK CLOSE WINDOW